Doctoral Dissertation
Doctoral Program in Energy Engineering (34th Cycle)

General assessment and radiation damage minimization of advanced structural materials for compact tokamaks

By

Stefano Segantin

******

Supervisor(s):
Prof. Massimo Zucchetti, Supervisor
Dr. Raffaella Testoni, Co-Supervisor

Doctoral Examination Committee:
Prof. Ju Li, Referee, Massachusetts Institute of Technology (MIT)
Prof. Penghui Cao, Referee, University of California Irvine

Politecnico di Torino
2022

Declaration

I hereby declare that, the contents and organization of this dissertation constitute my own original work and does not compromise in any way the rights of third parties, including those relating to the security of personal data.

Stefano Segantin

2022

* This dissertation is presented in partial fulfillment of the requirements for **Ph.D. degree** in the Graduate School of Politecnico di Torino (ScuDo).

I would like to dedicate this thesis to my loving parents and sister, who always pushed me to follow my dreams. I also dedicate this thesis to Elsa, who had the hardest job in supporting me during the whole process and I would have not succeeded without her love. A special dedication goes to my cousin Massimo, who did his best to follow his dreams.

Acknowledgments

And I would like to acknowledge my two advisors prof. Massimo Zucchetti and Dr. Raffaella Testoni for the effort and patience they put on teaching and supporting me and my work. I would like to acknowledge also Prof. Michael Short and Prof. Dennis Whyte for the priceless technical suggestions. The third acknowledgment goes to the friend of a lifetime, Mattia, who also supported me in my path. Last but not least, I would like to acknowledge my officemates Dr. Andrea Bersano, Ing. Samuele Meschini and Andrea Allio for the convivial atmosphere we created in our office, which made me go to work everyday with a smile.

Abstract

The necessity of suitable structural materials is one of the main issues that concern advanced reactor (i.e. Gen IV and fusion) designers and scientists. Advanced reactor concepts foresee high temperature environments, strongly corrosive coolants and an exacerbated radiation environment due to fast neutrons and high fluences. This thesis explores such aspects in the framework of a transition from a pre-conceptual to conceptual design of Affordable Robust Compact (ARC) fusion reactor. ARC concept is the flagship of the high magnetic field path to nuclear fusion energy. In this work, the suitable structural materials for ARC core structures, namely the vacuum vessel, are assessed. Four most concerning issues have been identified in ARC core environment: high thermal loads and temperature, structural integrity, a deeply corrosive environment and elevated neutron loads with unpredictable effects. A reference alloy for each of the families considered is here taken. The work focuses on steels, Ni-based superalloys, V-based alloys and Multiple Principal Element Alloys (MPEAs). An accelerated analytical thermomechanical analysis is proposed to identify the materials with the best thermomechanical tradeoff properties. Ni-based superalloys and V-based alloys show the highest chances to survive ARC core environment, with Ni-based superalloys having an extreme structural resistance and V-based alloys a more optimized mechanical-thermal properties tradeoff. The corrosion issue is out of the aims of this thesis. However, some main aspects and possible solutions (i.e. coatings and corrosion control through beryllium doping) are taken from literature and briefly discussed. The work divides the irradiation

aspects in three main studies. A neutron transport analysis, performed to assess the suitability of structural materials in the core environment. Ni-based alloys raised some concerns regarding their negative effect on the fuel cycle self-sustainability. Other alloys allow for more conservative results. Afterwards, the radiation induced activation of each alloy is estimated. In this instance, the study proposes some optimization techniques to minimize the expected radioactivity of irradiated materials. V-based alloys have the lowest achievable induced radioactivity, requiring disposal for less than a century. Ni-based superalloys would most likely require medium-level waste-like management strategies for a few centuries. Lastly, an advanced study on the primary radiation damage effects is proposed. The work aims to both assess the radiation resistance of the considered alloys and to provide some useful guidelines for the design of radiation-resistant advanced materials, like MPEAs. Results strengthen the hypothesis of a link between the potential energy landscape of a material and its radiation response, shedding light on the main driving mechanisms. It should be possible to identify the most radiation resistant alloys by characterizing their main element potential energy and defect migration energy barriers. While, for advanced and highly mixed materials, the heterogeneity in the energy barriers seem to be the driving parameter for designing a radiation resistant material.

Despite this work identifies V-based alloys and MPEAs as the most suitable for the purpose, because of the different technological readiness level, a different path is also suggested. A first version of ARC would probably rely on a Ni-based superalloy. The first ARC version will surely provide fundamental experimental data about its core environment effects on structural materials. The following, most efficient, versions of ARC should rely on better performing V-based alloys or advanced materials.

Contents

List of Figures

List of Tables

Chapter 1

Introduction

1.1 Motivation

Nuclear fusion research is looking forward to design the next generation of fusion reactors. Such reactors are supposed to be the first machines able to obtain net energy from the deuterium tritium fusion reaction. As physics is getting well-established, the main necessity is the development of solid solutions for the engineering design of fusion reactors. In this instance, the identification and selection of structural materials for the reactor core is a main challenge. Core components of a nuclear fusion reactor need to withstand one of the harshest environments seen in the energy sector. Structural materials must guarantee components integrity while tolerating extreme temperatures, thermal and mechanical loads, radiation and chemically aggressive environments.

In this respect, increasing the reactor size and reducing the operating temperature would lower the power density, ultimately relax the core materials requirement. However, necessity of market competitiveness and deploy practicality drive forward the attractiveness of compact reactors with high power densities. Such aspect meets its main engineering limit in the availability of sufficiently resilient materials for the construction of reactor core components.

In addition, it is particularly complex to experimentally reproduce the exact conditions of a fusion reactor, dramatically reducing the availability of reliable data for designers. Indeed, literature often shows how experts are particularly concerned about the lack of information about material behavior in fusion reactors [1], [2] and the risk of unavailability of effectively resistant materials amongst the commercial alloys.

In this framework, through the improvements of material modeling that bridge the gap with experiments, it is necessary to develop and optimize advanced materials able to broaden the current design limits of nuclear reactors.

1.2 Thesis objectives

The main target of this thesis is to provide a methodology of structural material choice and evaluation for the application in new generations of compact fusion reactors. The thesis also aims to give particular focus on advanced materials, namely vanadium-based alloys and multicomponent alloys. In this instance, a detailed list of the objectives is defined below:

1. Identification of the main issues that structural materials face in compact tokamaks;
2. Selection of the most promising materials from literature analysis;
3. Comparison of material behavior in terms of the identified issues;
4. Irradiation analysis of suitable materials and discussion of compatibility with blanket;
5. Assessment of radioactive waste caused by studied materials;
6. Insight of radiation damage and development of a strategy for damage minimization in advanced materials;

1.3 Historical context

Nuclear energy is one of the most challenging fields for material scientists. Components of fusion and fission reactor cores experience extremely severe conditions.

Historically, nuclear reactors structural materials were chosen amongst the strongest stainless steels and Nickel superalloys [3]. Reactor pressure vessels and their internals are usually made of type 304/316 stainless steels, A-286 and Alloy X-750 [3].

Such materials are largely sufficient for the structures of the first three generations of fission reactors, presenting low failure rates [4] and allowing decades of continuous full power operations of the plant [5]. However, innovations in the field highlighted the attractiveness of new families of materials, in particular Generation four fission reactors (Gen-IV), small modular reactors and nuclear fusion reactors require structural materials able to withstand higher temperature environments, higher thermal loads and need to show a perfectioned chemical stability [6]–[8]. More specifically, modern coolants, moderators and breeding blanket compounds as well as the necessity of higher thermodynamic efficiencies are the main cause of such material developments.

Generation four reactors propose many different configurations of core, coolant and balance of plant. Most of them abandoned water as coolant, exception made for the supercritical water reactor. Such decision relaxes the pressure load in

most configuration, they nevertheless raise temperature and corrosion problems. Proposed Gen-IV reactors feature molten salts, liquid metals or gases such as helium as coolants. The molten salts and liquid metals proposed for the new generation of reactors (e.g. chloride, fluoride, sodium, lead etc.) show melting temperatures between 100°C and 500°C unavoidably raising the operating temperature of the reactor and its components. Furthermore, the high fluid density and their chemical aggressiveness caused researchers to discard the most chemically susceptible alloys for the core structure. In this respect, Gen-IV researchers are still giving a shot to ferritic-martensitic (F-M) steels and stainless austenitic stainless steels [6], [9]. Moreover, several backup materials are under development and additional study. The most likely viable are the engineered oxide dispersed steels (ODS), the nickel-based alloys (e.g. the Inconel family) and some refractory alloys (mainly based on tungsten, molybdenum, tantalum etc.). The mentioned materials are known for their superior mechanical and thermal properties, radiation resistance and chemical stability. Also, they can operate at higher temperatures than usual steels. In this context, advanced materials, such as concentrated solid solutions, medium and high entropy alloys would further relax the thermal and mechanical limits and potentially increase the radiation resistance of the core structure [6], [9].

Currently operating fusion reactors are experimental apparatus that generate high thermal loads for few seconds and a nearly negligible neutron yield. For such machines, material properties of main importance are a sufficient resistance to thermal loads (good conductivity, high melting point) and high mechanical properties. Most of the fusion reactors feature stainless steels and nickel-based alloys [10], [11]. In particular, the high magnetic field - compact tokamak Alcator C-Mod applies a nickel-based superalloy (Inconel-718) for its core structures [12]. Nonetheless, scientists are forced to evaluate other type of materials for future fusion reactors. Next generation of fusion reactors will rely in the deuterium-tritium fusion. They therefore will have high thermal loads, high operational temperatures, chemically aggressive coolants and unprecedented fast neutron fluxes for nearly continuous operation.

In this respect, the main path to fusion energy is led by the ITER and DEMO projects [13]. Such reactors result from a wide international collaboration involving almost all of the world most advanced countries (i.e. European Union, United States, Russia, China, South Korea, Japan and India) [13] and are expected to achieve the goal of a fully working power plant in 2050-2070 [14]. Both the machine designs are very complex and exploit a large number of core components (e.g. vacuum vessel, breeding-modules, ports, divertor cassettes, shield blocks etc.). Most of the component are expected to be cooled down by water and component temperatures will be similar to light water reactor ones, by design. For this reason, classic iron-based alloys, such as SS-316, HT-9, T-91, are expected to compose most of the core structures [15]–[17]. However, there is a shared will to move forward to reduced activation steels, such as Eurofer-97 [15], [17], [18].

Alongside the ITER-DEMO pathway for fusion, a few private companies are trying to achieve fusion energy with different approaches. It is the case of Commonwealth of Fusion Systems (CFS), which aims to achieve fusion energy in shorter timescales leading the approach of high magnetic field – compact tokamaks. The compact tokamak configuration is made possible by the new High Temperature Superconductor (HTS) technology for the reactor magnets [19], [20]. CFS and MIT-PSFC propose a pathway composed by two fusion reactors. The first machine is the SPARC tokamak [21], [22]. SPARC is a purely experimental device with very specific goals. SPARC purposes are to prove the feasibility of a tokamak based on HTS magnets, achieve the energy breakeven, study the DT plasma physics, evaluate and assess the best divertor technologies [21]–[26]. ARC reactor is the second step of the CFS-MIT pathway [22]. ARC goal is to be the core component of a nuclear fusion pilot plant and provide the basis for commercially viable fusion energy. The high-field path for fusion energy currently relies on nickel-based superalloys (such as Inconel-718) for the current design of ARC [20], [27]. However, advanced materials are being developed in order to hold reliable backup solutions or even allow enhanced core performances. As a matter of fact, ARC constitutes the main case study for the advanced material analysis and design of this thesis, which will often recall its operating conditions.

1.4 Thesis structure

Chapter 2 describes the reactor case study considered for this thesis. Namely, ARC reactor. ARC operating conditions are discussed, and particular attention is given to the most pertinent ones for the core structural materials issue. The materials considered for this work are presented and their most relevant properties are compared. Chapter 3 actively explores the nuclear properties for the considered by means of Monte Carlo neutron transport models. Particular attention is given to the best structure-blanket configuration in terms of tritium produced, neutron flux on the structure and core shielding capability. Chapter 4 addresses radiation induced activation with rate equation models. It mainly focuses on the optimization of the ARC-relevant materials in terms of reducing induced activation. In addition, some preliminary information on irradiation damage are extrapolated and discussed. Chapter 5 takes advantage of Molecular Dynamics modeling for optimizing the most advanced ARC-relevant materials. In particular, primary damage and microdefect generation are minimized by means of the identification and tuning of the most damage-affecting material thermodynamic parameters. Afterwards, a characterization of energy barriers for

Chapter 2

Reactor-relevant structural materials

2.1 Introduction

The core of a fusion reactor is an extremely complex system. It is necessary to consider a wide range of physical aspects (e.g. thermodynamics, neutronics, corrosion etc.) in order to choose suitable materials. Each of these physical aspects requires sufficient values of the considered material relevant properties. In addition, it is often possible to observe synergistic effects of different physical aspects on the materials (e.g. radiation enhanced creep, radiation enhanced corrosion, rise of the ductile-brittle transition temperature etc. [28], [29]). Considering these premises, scientists should foresee the behavior of a given material in the desired working conditions as a whole, also considering the synergistic effects of the different physics involved. By doing so, it would be possible to identify univocally the best material for a given purpose. As a matter of fact, a procedure as sure as the given one would most likely identify more than one suitable material, leaving room to economic speculations for the final choice. However, this type of procedures is not viable in most of the cases. The complexity of experimentally reproduce all the physics as a whole is most likely prohibitive. Such complexity affects also the field of numerical modeling. This holds particularly true when it comes to consider material modeling. Often it is possible to model just one aspect and a physical phenomenon just to specific space and timescales. While many other modeling fields are usually considered self-consistent and sufficient for their purposes (e.g. thermo-fluid dynamics, structural mechanics, electro-magnetism etc.). The inability of experimentally or numerically reproduce a reactor core conditions as a whole forces material

scientists to consider just the most relevant physical phenomena one at a time. Synergistic effects are usually considered only if cause of particular concern (e.g. radiation enhanced corrosion [28], [29]).

In this chapter the Affordable Robust Compact (ARC) fusion reactor and its core conditions will be presented as main relevant case study. Such operating conditions affect most of the discussions that will be made about advanced materials, their properties and the design throughout the whole thesis. Subsequently, the materials that are considered for tokamak structures will be presented. In addition, the most relevant physical aspects of the reactor core will be discussed as well as some qualitative criteria for identifying the most attractive materials.

2.2 Compact high-field tokamaks

Fusion research is now focusing on magnetic confinement approach with deuterium and tritium as fuels. As previously mentioned, ITER and DEMO are the main projects of this field worldwide [13]. The strategy adopted by such projects is to apply the most consolidate technologies possible (classic low-temperature superconductors, iron-based stainless steels etc.). This approach should minimize the risk of project failure. Nevertheless, current consolidate technologies require for a high reactor complexity, especially in terms reactor size, number of components, fabrication and expected operation and maintenance requirements. The choice of the magnets technology caused the machines to require a colossal size and a low magnetic field, resulting in a relatively low power density of the core. As an alternative, it is possible to take a more pioneering approach that could be however more challenging. It is the case of the SPARC and ARC projects [20], [21]. They rely on novel technologies in order to design reactors with improved performances. Such machines are simple, compact and with a high power density. They indeed follow the footprints of the Alcator tokamak [30]. Among the high-field family ARC tokamak (Figure 1) aims to be the core of a pilot power plant virtually ready to be replicated at commercial scale level [20], [27].

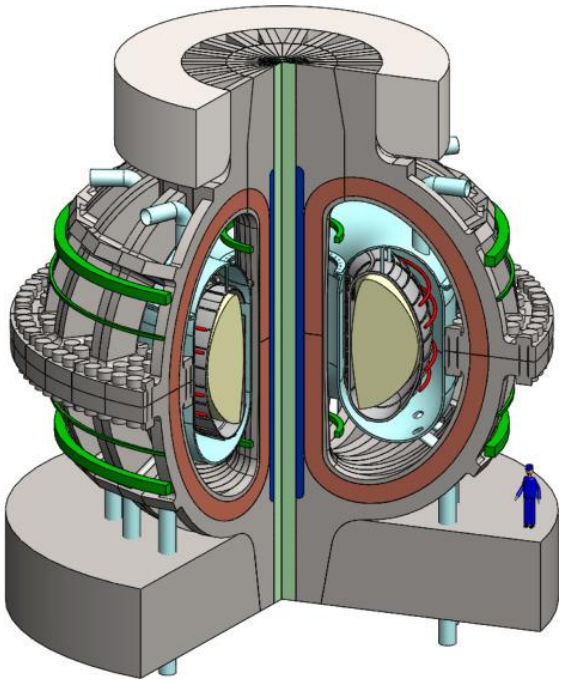

Figure 1: Rendering of the ARC reactor [20].

High temperature superconducting magnets is one of the most advanced technologies that ARC features. HTS are fundamental for enhancing plasma performances, increasing the power density and shrinking the reactor size. All the design choices will be a direct follow-up of the research activities carried out with SPARC. It therefore relies on plasma physics and magnetic configurations that will be proven solid. Because of its purposes, ARC tackles all the main challenges that constitute an obstacle to commercial fusion energy. In this instance, continuous operations (or high duty cycle, in the case of pulsed machines), a self-sustaining tritium cycle and a fully working balance of plant are the most power plant-relevant features. Table 1 lists the main design parameters of ARC [20].

Table 1: ARC main design parameters [20].

Design Parameter	Value	Units
Fusion Power	525	MW
Thermal Power	708	MW
Major radius	3.3	m
Minor radius	1.13	m
Plasma volume	141	m^3

Toroidal magnetic field	9.2	T
Fusion Power wall loading	2.5	$\frac{MW}{m^2}$

The reactor is still under design and most of the parameters may vary in the finalization phase of the project [20], [27]. Still, the aim of this thesis is to provide some solid material choice and design guidelines that remain relevant for any type of high power density tokamak, including future versions of ARC.

With a major radius of about 3 m and a fusion power of more than 500 MW, ARC is an extremely compact machine. For comparison, ITER and DEMO have major radius of about 6 m and 9 m and fusion powers of 500 MW and 2000 MW, respectively [14], [31]. ARC compactness is an attractive feature because of the expected reduced costs and deployment times required, as well as minimized radioactive inventories. Nevertheless, the high power density pushes to the limit several engineering parameters that need to be carefully addressed to ensure the success of the project. Alongside the reduced size, ARC holds additional peculiar features, such as a fully liquid blanket tank and a thin vacuum vessel immersed in the blanket [20], [27]. With the compact configuration, ARC core faces high thermal loads and neutron fluxes. The liquid blanket, necessarily made of a lithium-based compound, requires for high operating temperatures (between 800 K and 1000 K), comparable to Gen-IV reactor ones. The configuration of ARC reactor joins optimized plasma physics with economics attractiveness, but it constitutes a major challenge for core structural materials.

2.3 Compact tokamak core operating conditions

The operating conditions of the vacuum vessel are particularly relevant for this thesis as it aims to identify the best fitting materials for ARC core structures. As a matter of fact, the vessel is the only unavoidable structure in ARC core. In addition, there are some vessel design choices that are of main relevance for this thesis, more specifically:

- There is a thin tungsten first wall separating the plasma from the structure [27]. In this way it is possible to neglect some of the issues that are peculiar of the plasma facing components (e.g. interaction with high energy ions and electrons, sputtering etc.).
- Despite the thin first wall, the vessel structure is directly in neutron sight, with no chance of effective shielding.
- The vessel is double walled with a relatively thin inner structure connected with a more solid outer one. A layer of coolant flows between the two walls. A layer of a neutron multiplier material is added in order to ensure a self-sufficient fuel cycle [20], [27].

- The blanket is liquid and works as coolant for the core components. In the case of ARC the fluid is the FLiBe molten salt [20], [27]. But it is likely that a commercially viable plant would require a beryllium-free breeder compound seeing as how Be is highly toxic and a rather expensive element.

Figure 2 shows the qualitative configuration of ARC vacuum vessel layers.

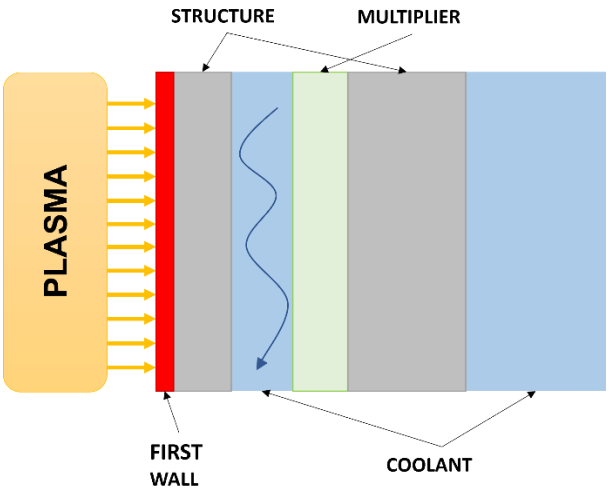

Figure 2: Configuration of ARC vacuum vessel layers. From the left: burning plasma, first wall, inner vessel structure, flowing coolant, neutron multiplier, bulk coolant in the tank.

The mentioned design choices are extremely attractive in terms of machine simplification and plant efficiency optimization. Nevertheless, they overhang on the materials that should compose the core structures. More specifically, FLiBe molten salt (or other Li-based compounds) and the plant thermodynamic efficiency require for a high temperature environment. The operating conditions are thus expected to be around 800-900 K [20], [27]. In addition, thermal loads and the neutron flux are expected to be nearly prohibitive because of the reactor power density. Thermal loads are expected to be on the order of 0.5 $\frac{MW}{m^2}$ for the main chamber and about 10 $\frac{MW}{m^2}$ in the divertor region. The neutron flux is expected to be between 1e+14 and 1e+15 $\frac{n}{cm^2 \cdot s}$ over the vessel structure [20], [27]. Temperature, thermal loads and neutron flux are of main interest for this work because they are expected to be among the problems that may determine the project success. It is worth to recall that the aim of this thesis is to provide some considerations about the best fitting materials also for generic compact tokamaks. Thus, the precision over some parameters will be relaxed in view of a more versatile results and considerations. This is also in view of likely changes that could occur in the configuration of ARC reactor itself. Table 2 lists the magnitude

of expected operating condition of a core component in ARC and other compact tokamaks with a similar power density.

Table 2: Generic core operating conditions of ARC reactor or other tokamaks of similar power density.

Load	value	Units
Temperature	800-900	K
Pressure	1-5	bar
Thermal load	0.5-10	$\frac{MW}{m^2}$
Neutron flux	1e+14-1e+15	$\frac{n}{cm^2 \cdot s}$
Desired lifetime	10’000-20’000	h

There are many other concerning aspects for the structural materials of compact tokamak cores. For instance, coolant chemical aggressiveness and electro-magnetic loads in off normal transients (e.g. plasma disruptions). Because of the extension of such issues, they will be only mentioned in this thesis, leaving extensive discussions to other specific studies. Regarding the magnetic forces, this work will only mention, when possible, whether a material is paramagnetic or ferromagnetic and its Curie temperature. Recalling that a ferromagnetic material will experience high stresses due to the intense magnetic field, especially it stands below the Curie temperature, while a paramagnetic material would weakly experience the magnetic field effect. The characterization of the chemical environment, on the other hand, is of primary importance, especially when it comes to evaluate the synergistic effect of irradiation and corrosion [28], [29]. Still, it is an extremely broad field that must be addressed in dedicated studies. Anyway, the corrosion issue is likely to be relaxed thanks to some technological strategies. It is the case of beryllium doping and protective coatings. Beryllium fluorides have the lowest activation energy amongst other metal-fluorides and Be is soluble in FLiBe [32]. Hence, it is possible to assume that, as fluorine is the most concerning element, additional Be in the solution would control the F aggressiveness on the structure. For what concerns coatings, amorphous aluminum oxide (Al_2O_3) coatings, for instance, have already shown their protection effectiveness on stainless steels against liquid lithium-lead compounds [33], showing also good ductility and hydrogen (tritium) permeability reduction [34], [35]. It is possible to assume that such type of coatings would be effective against other lithium-based compounds corrosion too. This work will however just discuss, when possible, whether a particular material is particularly

chemically susceptible or it has a high chromium content. Cr is usually added to increase the alloy performances and chemical stability at high temperatures [36]. Despite that, Cr raises significant corrosion issues when it comes to work in fluoride-rich dynamic environments [37]–[39]. Selective Cr leach has also been observed in oxygen rich liquid metals [40]. A high Chromium fraction is thus a likely issue for an ARC-like tokamak unless the coolant and blanket compound is changed.

2.4 Relevant structural materials

In this section, the most ARC-relevant structural materials will be shortly reviewed and their actual suitability for ARC environment will be discussed. This section will give particular attention to thermal properties comparison. The core operating temperature is considered the strictest parameter as well as the least attractive to relax, especially in terms of power plant thermodynamic efficiency. Operating temperature will be thus treated as first cutoff parameter for identifying the most suitable materials. Most attractive materials will be then deeply analysed throughout the rest of the thesis.

Ferritic/Martensitic (F/M) steels – Ferritic/Martensitic steels are iron-based alloys with a relatively high content of Chromium (9-12%) [36]. Other typical alloying elements present in the matrix are V, Mn, Nb, Mo and W [36]. The high Cr content is necessary for the steel to operate at high temperatures and withstand corrosion and oxidation. It nevertheless raises dynamic-driven corrosion issues in the ARC and fluoride-salt cooled reactors [37]–[39]. F/M steels present a BCC microstructure with a good swelling resistance [41]. F/M steels have good mechanical and thermal properties, with a yield strength in the range 500-800 MPa at room temperature [42], [43], while the thermal conductivity is roughly 15-35 $\frac{W}{m \cdot K}$ [43]. Nonetheless, mechanical properties significantly degrade at ARC-like operating temperatures [41]. F/M steels are limited up to 800 K or lower operating temperatures [41]. Because of the radiation induced ductile-to-brittle transition temperature increase, the operating temperature window in nuclear reactor cores is roughly in the range 500-800 K [44]. The temperature upper bound is quite prohibitive for ARC case study as 800 K is lower than or similar to the operating temperature of the coolant and structures need to operate at higher temperatures. F/M steels are particularly sensitive to magnetic fields as they are ferromagnetic materials. Suggestions say that ferromagnetic materials could be handled in DEMO design [42], still concerns increase when it comes to deal with high magnetic field machines like ARC. The Eurofer-97 alloy is of particular interest as it has been chosen as baseline structural material for the DEMO reactor [45]. It is a Reduced Activation Ferritic/Martensitic (RAFM) high temperature steel whose alloys elements were chosen specifically for low-activation purposes. Other reactor-relevant examples of F/M steels are HT-9, T-91 and NF12 [6].

Ferritic/martensitic steels can be considered a mature technology that has already been applied in nuclear industry. Data on the behavior of such materials in nuclear reactor are thus available. Additional research would be needed only for an ad hoc reactor environment in terms of a specific application or, if necessary, for the application of new material optimization techniques.

Oxide Dispersion Strengthened Steels (ODS) – Oxide Dispersion Strengthened steels are F/M steels that include yttrium-oxide dispersoids (Y_2O_3) in the matrix. ODS have been developed with the aim of increasing the allowed operating temperature of F/M steels [46]. ODS can operate at temperatures higher than 900 K with higher yield strength and better creep resistance than classic F/M steels. The downside is a reduced ductility [47]. Despite that, ODS have also shown an improved radiation tolerance as the Y-Ti-O dispersoids seem act like effective radiation defects sink [6]. ODSs seem to match well ARC operating conditions. They still have corrosion issues in fluoride-salts environment because of the relatively high chromium content and are also quite susceptible to magnetic fields. ODS match well the operating conditions of high temperature liquid metal reactors as well as low-field tokamaks. Assuming the feasibility of effective anti-corrosion barriers ODS could work fine also in molten salts reactor and ARC-like tokamak cores. Among the ODS, the ODS-Eurofer is the most studied for nuclear fusion applications as it is a reduced activation alloy based on Eurofer-97 with yttrium-oxide dispersoids. ODS-Eurofer shows indeed better high-temperature performances than Eurofer-97, especially in terms of creep resistance and high temperature yield strength [47].

ODS have not been extensively applied in the nuclear industry yet. Hence, there is a lack of data of the behavior of such materials in normal operating conditions. Nevertheless, they have been extensively studied in the past few decades and there would just be the necessity of additional high dose studies [6].

Austenitic steels – Austenitic Stainless Steels are Fe-based alloys with good mechanical properties and corrosion resistance. Like F/M steels, austenitic stainless steels often show a high chromium content (16-20%) [48]. They are more ductile than F/M steels and show good creep properties at slightly higher temperatures, up to around 850 K [6], [49]. In contrast to F/M steels, austenitic steels show an FCC microstructure, making them more sensitive to irradiation damage and swelling [6]. In addition, the thermal conductivity of austenitic stainless steels is usually in the range 15-20 $\frac{W}{m \cdot K}$ [48], [50], that is lower with respect the F/M steels one [6]. This aspect may heavily affect both the operating temperature of the structure at equal coolant temperature as well as the thermal stress. SS-316 is probably the austenitic stainless steel most applied in nuclear industry. It is used in gen-III reactors and it is the primary choice also for most of the gen-IV reactors [3], [6]. SS-316 is also the baseline structural material of ITER tokamak [51].

Like F/M steels, austenitic stainless steels are a mature technology that has been widely used in the nuclear sector. Additional research would be needed only for an ad hoc reactor environment in terms of a specific application or, if necessary, for the application of new material optimization techniques.

Nickel-based superalloys – Nickel-based superalloys are corrosion resistant materials able to operate at high temperatures, up to about 1000 K for prolonged periods of time [52]–[54]. Their chemical composition is usually constituted by about 10 alloying elements [52]. There is a nickel matrix with additional elements, such as Cr, Co, Al, Ti, W, Mn, Mo, Fe and a minor content of other elements such as Mn, C, B and Si [55], [56]. In particular, the chromium content is relatively high (10-20%) [55]–[57]. Despite the good corrosion resistance in normal applications, the high content of Cr has shown to be the cause of a fast-deteriorating effect in flowing fluoride-salts environment [58], [59]. Ni-based superalloys present some nuclear-related issues. First, they have an FCC microstructure, which means that they are more prone to radiation damage than other microstructures. Secondly, nickel is more likely to transmute gas than many other alloying elements. Lastly, nickel heavily suffers from neutron-induced radioactivity [60]. This makes this family of materials as the most radioactive after irradiation on this list. On the other hand, Ni-based superalloys hold a very high yield also at high temperatures. The yield strength ranges in 800-1100 MPa [61]. The most temperature-resistant superalloys allow an operating temperature above 1000 K and show a good creep resistance up to 1100 K. Temperatures allowed are therefore roughly 400 K higher than the Fe-based alloys previously discussed. Thermal conductivity of Ni-based alloys is usually higher than austenitic stainless steels but lower than F/M steels. In most of the superalloys it ranges in 20-25 $\frac{W}{m \cdot K}$ in the allowed temperature window [62]–[64]. Ni-based superalloys are usually paramagnetic at room temperature with some ferromagnetic traits [65].

Inconel series belong to this family of alloys and has already been applied in experimental deuterium-deuterium fusion reactors [12]. Additionally, the Inconel-718 has been chosen as the baseline structural material for the ARC reactor [20], [27]. Nevertheless, the corrosion, activation and gas transmutation issues led the ARC team to begin the development of more suitable alternatives.

Most of the nickel-based superalloys have already been found their applications in several fields. Gen-III fission reactors have seen the use of Inconel-625 for core components [66]. Other type of Ni-based superalloys are being extensively studied for use in both nuclear fusion and fission fields. As a Ni-based superalloy is set as baseline material for ARC and Ni-based superalloys have also an advanced readiness level for nuclear applications, an appendix at the end of this work has been added in order to provide an insight on this family of materials with some focus on the most ARC relevant properties and aspects.

Vanadium-based alloys – V-based alloys feature a BCC vanadium matrix and few alloying elements. Most common alloying elements are Ti, Cr and Si. V-Cr-Ti systems are the most studied in nuclear fusion industry. In such alloys titanium and chromium content stand in the ranges 0 – 5% and 0 – 15%, respectively. Interest in this type of alloys has risen because of their nuclear properties and capability of operate at very high temperatures. A superior radiation resistance and a very low neutron induced activation are the most attracting nuclear properties of this family of materials [67], [68]. Thermal conductivity is around 30-35 $\frac{W}{m \cdot K}$, which is higher than Ni-based superalloys and austenitic stainless steels and comparable to F/M steels [69]. Vanadium alloys show nonetheless a relatively low yield strength, which is in the range 200-700 MPa, depending on the alloy type and operating temperature [68]–[72]. In addition, the high temperature yield strength and the creep limits allow operating temperatures and stresses comparable to nickel superalloys ones [73]–[77]. In addition to chromium reactivity with fluoride salts, vanadium alloys are chemically susceptible to many other environments [78], [79]. They therefore need particular attention in the development of anti-corrosion coatings. V-based alloys show paramagnetic behavior [80].

V-4Cr-4Ti is considered the baseline composition for vanadium alloys for nuclear fusion applications [72], [78].

Vanadium alloys have been developed in the last few decades. Still, they are still in the research phase and they have not found extensive application in the nuclear field yet. Main aspects that research is addressing include techniques for corrosion resistance, fabrication technologies and behavior at high radiation doses.

Advanced materials/Multicomponent materials - In addition to the classic alloys presented so far, it is worth to mention some advanced materials that are particularly promising for extreme environment resistance.

Advanced materials considered in this work are the so-called Multi-Principal Element Alloys (MPEAs), also known as Concentrated Solid Solution Alloys (CSAs). Single-Phase Concentrated Solid Solutions (SP-CSAs), Medium Entropy Alloys (MEAs) and High Entropy Alloys (HEAs) are the most studied categories that belong to the MPEA family. Classic alloys have a single principal element matrix (e.g. iron in Fe-based alloys, nickel in Ni-based alloys, aluminum in Al-based alloys etc.) and several alloying elements, such as Ni, Cr, Mo, Mn, C, Si etc., that are present in minor concentrations (0.1%-5%). The hallmark of MPEAs is that several elements are present in nearly equimolar concentrations to form a solid solution. The main consequence is a rise of the degrees of freedom in the alloy design. Furthermore, several alloys belonging to the MPEA family showed outstanding properties already. HEAs are likely the most promising alloys of this family for both the degrees of freedom they allow in the alloy design and the mechanical properties in a wide range of operating temperature. In fact,

preliminary experimental studies on HEAs had remarkable results. Firstly, several HEAs have an excellent thermal stability. HEAs seem to be able to increase the operating temperature by several hundreds of K. In particular, the degradation of the main mechanical properties occurs well above 1500 K of temperature for some HEAs [81]. While creep still needs much more exploration to be characterized [82]. Secondly, some HEAs showed also superior chemical stability at high temperatures [82]. These aspects could relax the necessity of highly engineered coatings, increase the system thermal efficiency and open to functional compounds for the liquid blanket that have a high melting temperature. On the other hand, it seems that HEAs tend to have relatively low thermal conductivities [83]. Higher thermal stresses are thus expected in face of a more resilient material and a trade-off study should be conducted.

MPEAs comprise a wide range of alloys, and materials belonging to this family show extremely different properties. Secondly, MPEAs are still in design and development phase. They are not yet being produced at industrial scale nor widely applied in any sector. Most advanced materials are still being studied and characterized at laboratory scale. In this sense research is focusing both in characterizing most relevant aspects and properties of MPEAs and exploring the broad phase space provided by the multiple degrees of freedom in the alloy design. For these reasons, there is still a lack of data about the full properties of a single MPEA.

It is usually not possible to design stable and application-relevant solid solutions with the combination of random elements on the periodic table. Nevertheless, it is possible to evaluate whether some elements are likely to form stable and single-phase solid solutions [84]. Despite the broad range of degrees of freedom in MPEAs design, this work will take as example one of the most interesting HEAs that are currently under development and characterization, namely the WTaVCrTi system [85]–[87]. Such system is composed by most of the low-activation elements as well as refractory elements for high temperature operations. Hence, it holds the potentialities for a reactor relevant high entropy alloy. This work aims to identify the most relevant elements to form a solid solution, especially in terms of radiation physics and to provide some guidelines for the design of reactor relevant MPEAs.

Table 3 summarizes the main features and properties of the mentioned materials. The table does not include MPEAs or HEAs because of their relatively immaturity as technology, their broad range of possible alloys and the lack of complete data.

Table 3: Summary of main relevant properties of the considered materials.

Material	Cell	Cr content [%]	Max. operating T [K]	σ_y [MPa]	k $\left[\frac{W}{m \cdot K}\right]$
F/M steels	BCC	$9-15$	800	$200-400$	$15-35$
ODS Steels	BCC	$9-12$	$950-1000$	$200-600$	$15-35$
Austenitic SS	FCC	$16-20$	850	$150-200$	$15-20$
Ni-based superalloys	FCC	$10-20$	$1000-1100$	$800-1100$	$20-25$
V-based alloys	BCC	$0-15$	$950-1000$	$200-700$	$30-35$

2.5 Thermomechanics comparison

Regardless of the configuration, all tokamak core elements need to withstand high temperatures and high thermal loads that usually lead to high thermal stresses. This is the case for the vacuum vessel and first wall structures. Despite being classified as secondary stress, and hence with a higher allowed threshold than classic mechanical loads, thermal stresses may constitute the largest fraction of the whole stress experienced by the component. Thermomechanics is a known field of engineering and it is the first step for choosing a material in a thermal system. In this sense, most of the materials considered for the design of a reactor have known and proven mechanical and thermal properties. Seeing as how structural materials in a tokamak core must work in harsh thermal and mechanical conditions, it is best to choose the material that minimizes the thermal stress still bearing mechanical loads. It is here proposed the derivation of a simple parameter aimed to work as a tool for comparing material thermal and mechanical properties. The derivation takes advantage from the simplest thermal system possible (e.g. Figure 3). The system is not dissimilar to what experiences the first wall structure of a tokamak and the vacuum vessel of ARC.

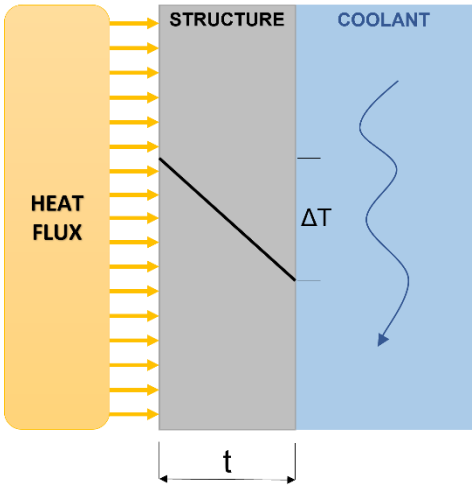

Figure 3: Heat flux – wall – coolant thermal model. ΔT is the temperature gradient experienced along the structure thickness. Coolant applied for temperature steady state.

In the model of Figure 3, the material of thickness t experiences thermal stress caused by the heat flux and a generic mechanical constraint. According to Hooke's law for continuous media, stress is given by $\sigma=E\cdot\varepsilon$, assuming a linear elastic material behavior, reasonable assumption in metals. In the case of solely thermal stress, it is possible to write $\varepsilon= \alpha\cdot\Delta T$. While E and α are properties of the material, ΔT is given also by the external conditions that the component experiences, such as the magnitude of the thermal load. In particular, the temperature gradient can be derived from $Q=U\cdot\Delta T$ where Q is the surface heat load $\left(\frac{W}{m^2}\right)$ and U is the global heat exchange coefficient $\left(\frac{W}{m^2\cdot K}\right)$. In the system considered, $U = \left(\frac{1}{h}+\frac{t}{k}\right)^{-1}$ where t is the material thickness. The convective coefficient h is here assumed orders of magnitude higher than $\frac{k}{t}$. This usually holds true in the case of and optimized cooling system. Otherwise, for the purpose of this discussion, it is possible to assume h fixed and take it out from the parametrization. Likewise, the thermal flux Q is an external load that may vary depending on the system, it is thus possible to assume it fixed and henceforth apply the proportionality sign to equations. The temperature gradient can be written as $\Delta T \propto \frac{t}{k}$. Substituting in the Hooke's law for thermal stress:

$$\sigma_{th} \propto E \cdot \alpha \cdot \frac{t}{k} \qquad \text{Eq. 1}$$

Thermal stress is thus directly proportional to the material thermal expansion coefficient and inversely proportional to the material thermal conductivity. σ_{th} is also proportional to the material thickness, which is the only parameter that is not directly related to the material properties. The higher the thickness t, the higher the thermal stress experienced by the material. However, it is not possible to reduce t by choice. A minimum material thickness is also directly related to the

structure integrity. Considering ARC vacuum vessel, it has to withstand gravitational forces, pressure forces due to the flowing FLiBe and electromechanical loads in the case of off-normal operations (e.g. plasma disruption). In the case of mechanical loads, designers chose material thickness depending on the magnitude of the load applied and the yield strength of the structural material. Considering a simple model of a load force perpendicular to the material cross section, the minimum thickness linked to the yield strength according to $\sigma_y \propto \frac{F}{A}$ where F is the generic mechanical load and A is the material active cross section area, which is proportional to t and another length that is usually fixed by design. Fixing the mechanical load, it is possible to write $t_{min} \propto \frac{1}{\sigma_y}$. It is possible to substitute in Eq. 1 the thickness with another property of the material (i.e. yield strength). Hence, it is here proposed a parameter that takes into account both thermal and structural properties of materials, here called for simplicity material termomechanical parameter (mtm):

$$\frac{1}{\sigma_{th}} \propto mtm = \frac{k \cdot \sigma_y}{E \cdot \alpha} \qquad \text{Eq. 2}$$

Because of several simplifications and the repeated use of the proportional sign, such parameter should give just qualitative information about material properties. It rather works well for comparing candidate materials and identifying the material with the best mix of thermal and mechanical properties. The mtm parameter is inversely proportional the induced thermal stresses. Hence, materials with high value of mtm parameter should be preferred for the structures of a thermal system. In this instance, a most suitable material should have a high thermal conductivity k, in order to reduce the temperature gradient along the thickness, a high yield strength and a low thermal expansion coefficient α for reducing the elongation and the thermal stress. It is here proposed a comparison of a reference alloy for each class of materials, namely Eurofer-97, ODS, SS-316, Inconel718 and V-4Cr-4Ti. Once again, MPEAs have not been implemented in the comparison because of the lack of complete data on their properties. Material properties have been taken from literature [88]–[101]. Particular attention has been given in finding properties that were temperature dependent in order to evaluate the mtm parameter in an ARC-relevant temperature window, that has been set in [700; 1000] K. Figure 4 shows the behavior of the mtm parameter with temperature for the mentioned reference materials. For Eurofer97 thermal conductivity and V-4Cr-4Ti thermal conductivity and thermal expansion coefficient have been used correlations extrapolated from data with a proven validity up to 900 K. Dashed lines show where such properties correlations have been extended to match the ARC-relevant operating temperature window. For V-4Cr-4Ti there is no reason to believe the properties will change behavior in the window 900-1000 K as it is the most stable alloy at those temperatures. Contrarily, Eurofer97 is closer to its melting point and it is not excluded its

thermal conductivity could change behavior. Anyway, for sake of simplicity, the correlations of the mentioned properties are here expanded up to 1000 K.

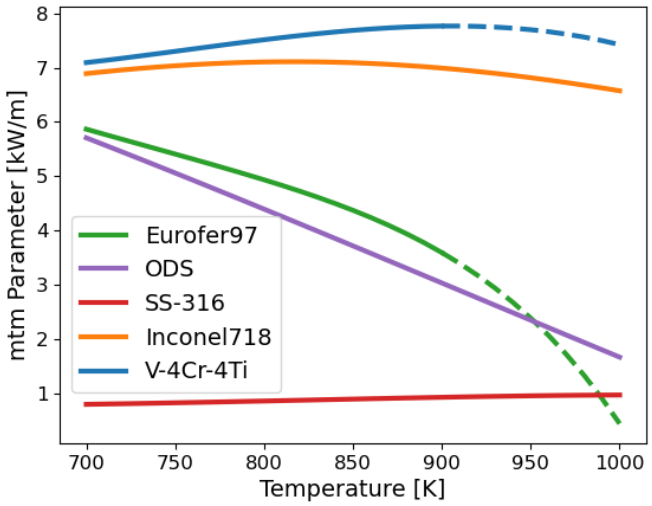

Figure 4: Material thermo-mechanic parameter vs temperature for Eurofer97, SS-316, Inconel718 and V-4Cr-4Ti.

According to Figure 4, V-4Cr-4Ti and Inconel-718 show the highest mtm parameter values in the whole temperature range considered. They should be able to minimize the thermal stress and the temperature reached under reactor-relevant thermal loads. For instance, according to the mtm parameter, SS-316 would experience about 8 times higher thermal stress than V-4Cr-4Ti, in the same operating conditions. To conclude the comparison, Figure 5 shows the maximum temperature reached by the wall in the case of a fixed wall thickness of 10 mm as in the baseline design of ARC vacuum vessel. According to the simplified: $T_{wall} = T_{cool} + \frac{Q \cdot t}{k}$, where T_{cool} is the coolant temperature and the convective coefficient is assumed equal to infinite. Eurofer97 and ODS show a quasi-identical wall temperature.

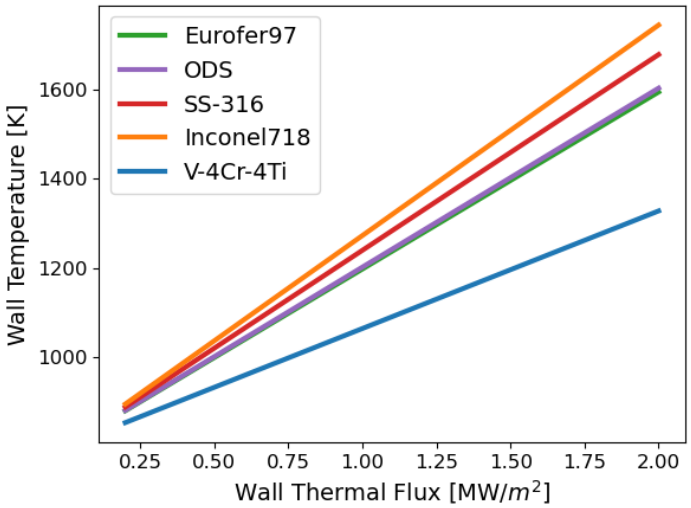

Figure 5: Wall maximum temperature vs wall thermal flux. Computed on a 10 mm thick wall for the four materials of reference.

In the expected ARC operating conditions (i.e. 0.5 $\frac{MW}{m^2}$ of thermal load and 800 K of coolant temperature) almost all the structural materials would reach a wall peak temperature of above 1000 K. The V-based alloy would be able to stand below such temperature because of its higher thermal conductivity.

In literature is possible to find several works that experimentally evaluated the given material properties. This study choses to get material properties from references that provided a temperature dependent fitted correlation [90]–[93], [95], [96], [101], [102]. Nevertheless, it is possible to find other temperature dependent properties from other studies or datasheets from factories. Most properties are slightly variable, hence a sensitivity study should be carried out, when possible. Concerning the ODS series, it has been difficult to find consistent properties for a single alloy. For ODS some properties have been averaged or curve-fit in the temperature range of relevance starting from literature data. For this reason, ODS properties must be considered slightly less accurate than other material ones. Despite the slight variability, the overall behavior of the properties and the mtm parameter is considered accurate enough for a qualitative and comparative study.

2.6 Discussion and conclusions

In this chapter the ARC case study and its core configuration have been described. Focus has been given to design choices that are more relevant for an assessment on suitable core structural materials. In this respect, it is worth to recall that ARC will be a compact machine with a high power density. Its core structure will be composed by a relatively thin vacuum vessel immersed in a molten salt tank. The

liquid compound will work as both breeding blanket and coolant. The first issue identified is that molten salts usually operate at high temperatures. On the other hand, the choice of molten salt relaxes the pressure requirements. FLiBe and the other molten salts can indeed flow at nearly atmospheric pressure. While mechanical loads are expected to be low, the high power density suggests that heat loads and neutron fluxes will be more concerning. Thermal stress and neutron damage are thus identified as second and third issues for the material structure. In this instance, the operating conditions of ARC core in terms of operating temperature, magnitude of thermal loads and magnitude of neutron fluxes have been recalled from literature and discussed.

The second part of this chapter addressed the thermal problem from the point of view of structural materials. The aim was to identify the materials that have the best mix of mechanical and thermal properties. A list of materials considered for ARC structures have been made. Namely, F/M steels, ODS steels, austenitic stainless steels, Ni-based superalloys and V-based alloys. Particular attention have been given to their mechanical and thermal properties. Lastly, a material thermomechanical parameter, here called mtm parameter for simplicity, has been derived and proposed for carrying out qualitative analysis and comparisons. The study then compared material properties in the ARC operating temperature window on the basis of such parameter. It is expected that the peak temperature of materials will be above 900 K or even 1000 K in most cases.

Despite F/M and austenitic steels have been here considered, they are not expected to be able to operate at such temperatures. At such temperatures they usually experience a drop in the yield strength and an increase in the elongation rate, suggesting they would be subject to plastic deformation and be particularly sensitive to creep [103]. Oxide Dispersion Strengthened steels seem to be able to successfully extend the operating temperature window [104] even though they do not seem to be the most optimized alloys on this list. From the analysis it came out that Inconel-718 and V-4Cr-4Ti show the optimal mix of thermal and mechanical properties. The former has better mechanical properties while the latter has better thermal properties.

It is worth to mention that the mtm parameter does not contemplate materials creep-related properties. Creep resistance should be addressed in order to conclude the considerations about thermal properties of the mentioned materials. In thermal machines creep is surely one of the biggest threats for continuous operations. Hence, an accurate creep analysis and comparison should be carried out. However, as a creep analysis is beyond the scope of this thesis, just a comparison between materials will be given on the basis of available literature. ARC vacuum vessel is expected to operate for years, that is a time on the order of 10000 hours. Hence, it is possible to compare the stress that considered materials could withstand at ARC temperature of operation for about ten thousands (1e+4) hours. F/M steels and austenitic stainless steels have a stress limit below 160-200

MPa at 875 K for the operating time required [105]. ODS steels are expected to have a stress limit of about 300 MPa at 925 K [106]. Inconel-718 could withstand up to 500 MPa at 925 K for about 1e+4 hours [107]. V-4Cr-4Ti is able to bear up to 400 MPa at about 875 K for 1e+4 hours [108]. It is possible to conclude that also in dynamic conditions, Inconel-718 and V-4Cr-4Ti system show the most promising behaviors.

Lastly, it necessary to recall that all the thermal and mechanical properties considered in this section belong to unirradiated materials. Most of them are expected to show a change with neutron irradiation. The next step is indeed the study of material behavior under irradiation in order to characterize the properties, analyze the microstructural evolution and reduce the irradiation damage as well as the induced radioactivity. In fact, material behavior under irradiation is extensively studied in nuclear field and experiments predict pretty well the material behavior in a reactor in most cases. However, it is nearly impossible to reproduce the irradiation conditions of a fusion reactor nor to predict the material properties behavior with a good confidence. Therefore, research activities should identify the most likely materials able to withstand a fusion reactor irradiating conditions and increase the portfolio of attractive materials by exploring advanced ones. In the meanwhile, modeling activities should be employed to design advanced materials able to minimize the most concerning aspects of radiation damage.

Despite the expected changes with irradiation, unirradiated properties are still necessary to start a baseline choice of suitable materials for a reactor core.

Chapter 3

Core neutronics

3.1 Introduction

A neutronics analysis is the second step for assessing the suitability of structural materials in a tokamak core environment. In a fusion reactor neutronics is necessary for four main reasons. First, it is needed to evaluate a core configuration effectiveness in breeding tritium through the $^{6}Li(n, T)^{4}He$ reaction. It is worth to mention that in fact tritium is not present in nature and needs to be bred directly in the reactor for ensuring a self-sustained plant fuel cycle. Secondly, neutronics provide the distribution of the neutron power deposition in the core. Third, it is possible to evaluate the core shielding effectiveness and design additional shield for the magnets. Lastly, neutronics gives information necessary for the evaluation of the irradiation effects on materials, such as transmutation, induced activation, damage and swelling. This chapter describes the neutronics modeling activities carried out for ARC core:

- discussion of the main material nuclear properties relevant for the study;
- description of the modeling technique and the software applied;
- description of the modeling choice for ARC core;
- results presentation and discussion.

The objectives of the neutronics modeling activities are to identify the structural material with the best nuclear properties and to assess its behavior considering the synergistic effects with the breeding blanket compound. Results of the neutronics modeling activities are necessary to carry out some specific studies for the considered structural material analysis. More explicitly, the

resulting neutron flux and spectrum on the structures would help modeling the radiation induced activation and the radiation damage effects.

3.2 Nuclear properties

Nuclear properties relevant for this work can be reduced to the element cross sections that enhance the reactor tritium economy and reduce the irradiation damage in solid components. Considering the tritium task, elements composing core materials should have a low neutron absorption (n, γ) and a good neutron multiplication capacity (n, xn). Figure 6 shows the mentioned cross sections for the main elements (Fe, Ni, Ti, V, Cr, Ta, W) of the structural materials considered in this work. For a better clearness the pictures show the cross sections of the isotopes that have a natural abundance above 10% for each element. Structural elements have been subdivided as the most abundant in Fe-based and Ni-based alloys (Fe and Ni), then in V-Cr-Ti systems. Ta and W cross sections have been added as interesting refractory elements for a high entropy alloy alongside V-Cr-Ti. Despite cross sections are usually displayed in log-log scale, here it has been chosen to set a linear scale for the energy axis in order to focus on the very fast neutron interactions. This choice is driven by the fact in the vessel region neutrons are expected to have a very hard spectrum with a predominant energy peaking at 14 MeV [109].

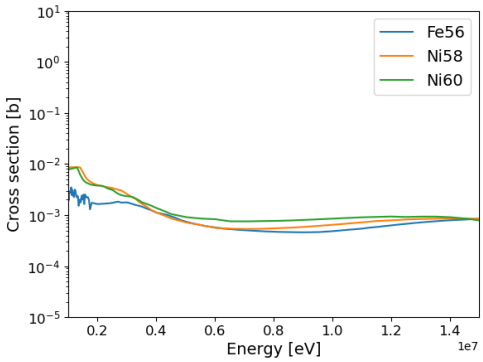

(a)

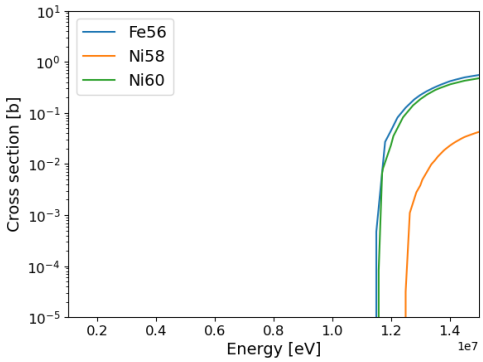

(b)

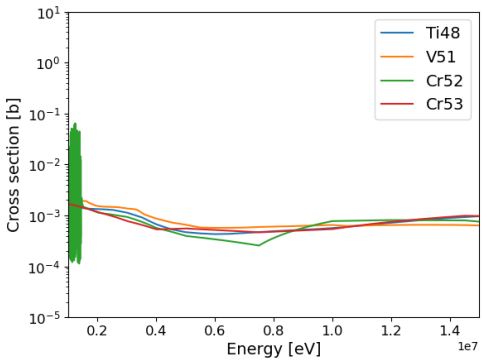

(c)

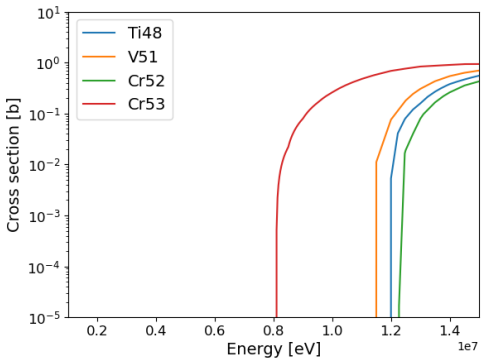

(d)

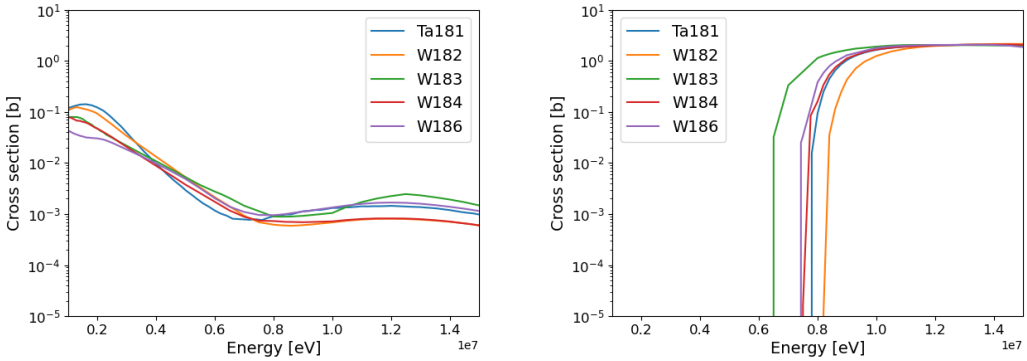

(e) *(f)*

Figure 6: Neutron cross sections of the main elements for structural materials. (a) and (b) correspond to most naturally abundant Fe and Ni isotopes. (c) and (d) correspond to most naturally abundant Ti, V and Cr. (e) and (f) correspond to most naturally abundant Ta and W isotopes. (a), (c) and (e) show the (n, γ) absorption cross sections. (b), (d) and (f) show the (n, 2n) neutron multiplication cross section. Data have been taken from ENDF/B-VIII library [110].

In addition to the mentioned cross sections, structural materials should be as much transparent to neutrons as possible. The breeding blanket compound should have a high lithium concentration as well as good neutron shielding and moderating capabilities. Namely, the blanket compound should have a relatively high total cross section but a low average atomic weight of the elements.

Regarding structural materials, radiation damage is a rather concerning issue that has to be addressed starting from neutronics. Typical mechanisms of radiation damage are microdefect generation and clustering, dislocation generation and motion, hydrogen segregation and helium-void nucleation and swelling. All of the mentioned mechanisms show up in most of the irradiation conditions. Despite that, hydrogen segregation and swelling are believed to be much pronounced in fusion reactor than any other reactor [111]. Mostly because of the neutron energy incoming from the fusion reaction itself (i.e. 14.06 MeV). Radiation damage mechanisms will be deeply discussed in Chapter 5. In this section nuclear properties that play a role in some of such phenomena will be depicted. More specifically, helium and hydrogen generation through the (n,p), (n,α) cross sections. Figure 7 shows the mentioned cross sections for the main elements of the considered structural alloys.

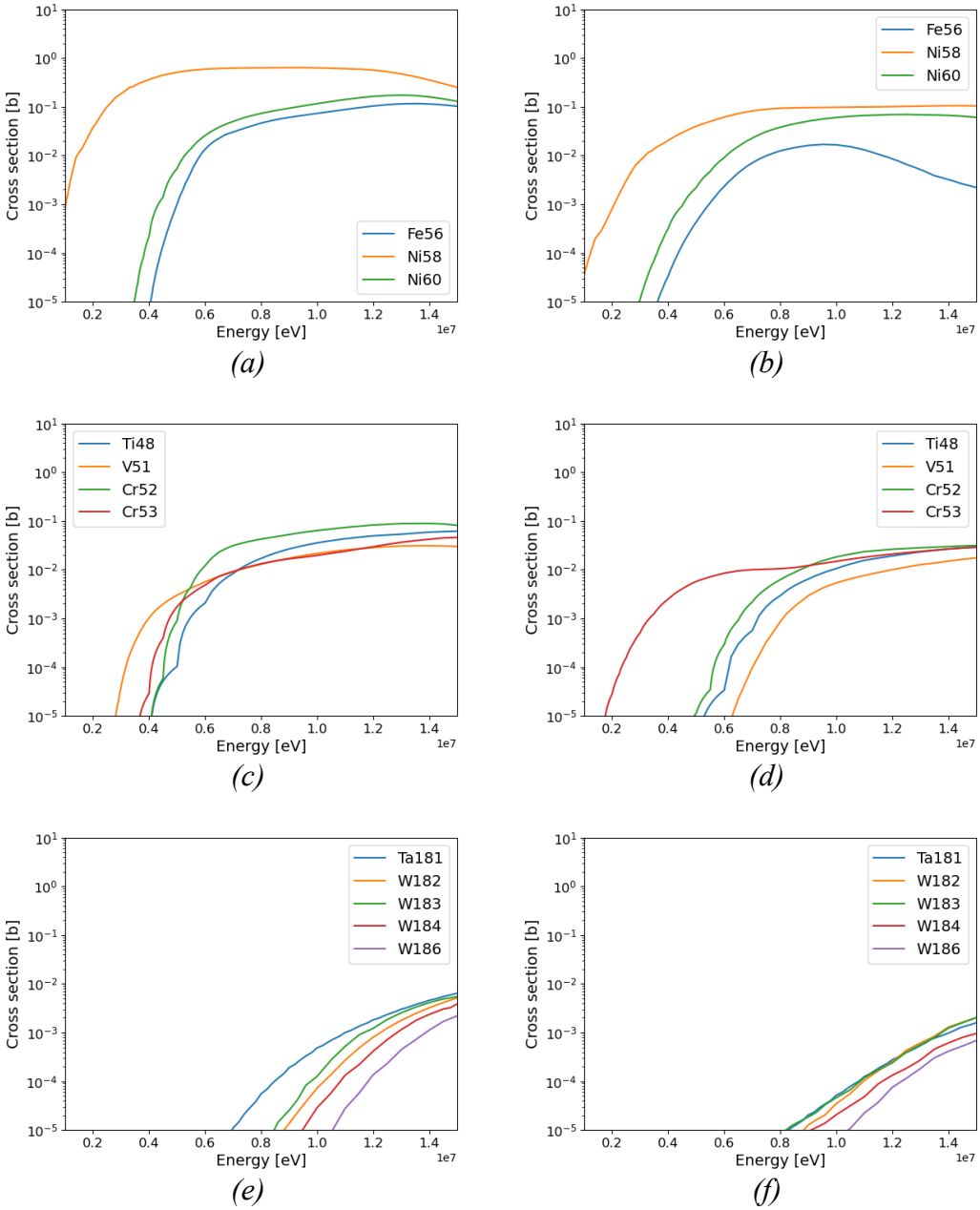

Figure 7: Neutron cross sections of the main elements for structural materials. (a) and (b) correspond to most naturally abundant Fe and Ni isotopes. (c) and (d) correspond to most naturally abundant Ti, V and Cr. (e) and (f) correspond to most naturally abundant Ta and W isotopes. (a), (c) and (e) show the (n, p) hydrogen transmutation cross sections. (b), (d) and (f) show the (n, α) helium transmutation cross section. Data have been taken from ENDF/B-VIII library [110].

The cross sections displayed in Figure 6 and Figure 7 have been plotted taking advantage of the OpenMC software and the ENDF/B-VIII library [109], [110].

From pictures it is possible to notice that in the fast side of the spectrum the considered transition metals have similar absorption effectiveness. Still, it is possible to notice that nickel isotopes raise their (n, γ) cross sections by one order of magnitude at energies lower than 3-4 MeV. In addition, refractory and quasi-refractory metals (i.e. Ta, W and Ti, V, Cr) show a wider and higher neutron multiplication cross section. For this reason it is possible to expect that V-based alloys and MPEAs that include refractory elements would enhance the reactor neutron and tritium economy with respect the Ni-based superalloys. Furthermore, V-Cr-Ti systems are typically characterized by a lower density than other transition metal-based alloys. They are thus expected to be more transparent to neutrons. This aspect should additionally enhance the neutron economy of the reactor. It is therefore expected that a V-Cr-Ti structure would maximize the reactor tritium breeding ratio. Regarding transmutation of gas, it is clear that nickel is particularly subjected to hydrogen and helium nuclei transmutation. In the meanwhile, refractory metals seem to be less sensitive to gas transmutation, with a less wide and two order of magnitude lower cross section. As Ta and W are particularly heavy metals, also (n, n+p) and (n, n+α) cross sections have been checked and it has been found that they have similar magnitude of regular (n, p) and (n, α) ones. Despite that, it is possible to expect that alloys with high nickel concentrations would suffer swelling more than V-based alloys and way more than MPEAs with high Ta and W fractions.

Comparing cross sections gives qualitative information on the behavior of elements in a given irradiation environment. Still, neutronics modeling can provide more specific data useful for the design of a reactor core. More specifically, this work is interested in assessing the best fitting structural material for ARC core. In this respect, neutronics modeling is used to evaluate how structural materials affect ARC tritium breeding ratio and to evaluate its magnitude. Neutronics can evaluate fundamental quantities for assessing radiation damage, such as neutron fluxes and energy spectra. The following subsections provide the neutronics modeling strategies adopted for this thesis as well as the most relevant model results.

3.3 Methodology

For neutronics simulations this work takes advantage of OpenMC tool [112]. It is an open-source Monte Carlo particles transport software developed at the Massachusetts Institute of Technology. Monte Carlo neutron transport algorithms and modeling techniques and strategies are not at the core of this thesis. They will be rather used to qualitative evaluate the nuclear properties of the structural materials here considered. For this reason, a short description of the working flow of a Monte Carlo particle transport algorithm is considered sufficient. MC transport codes are based on probability distributions that have to be known a priori. Figure 8 describes a simplified version of the algorithms usually applied.

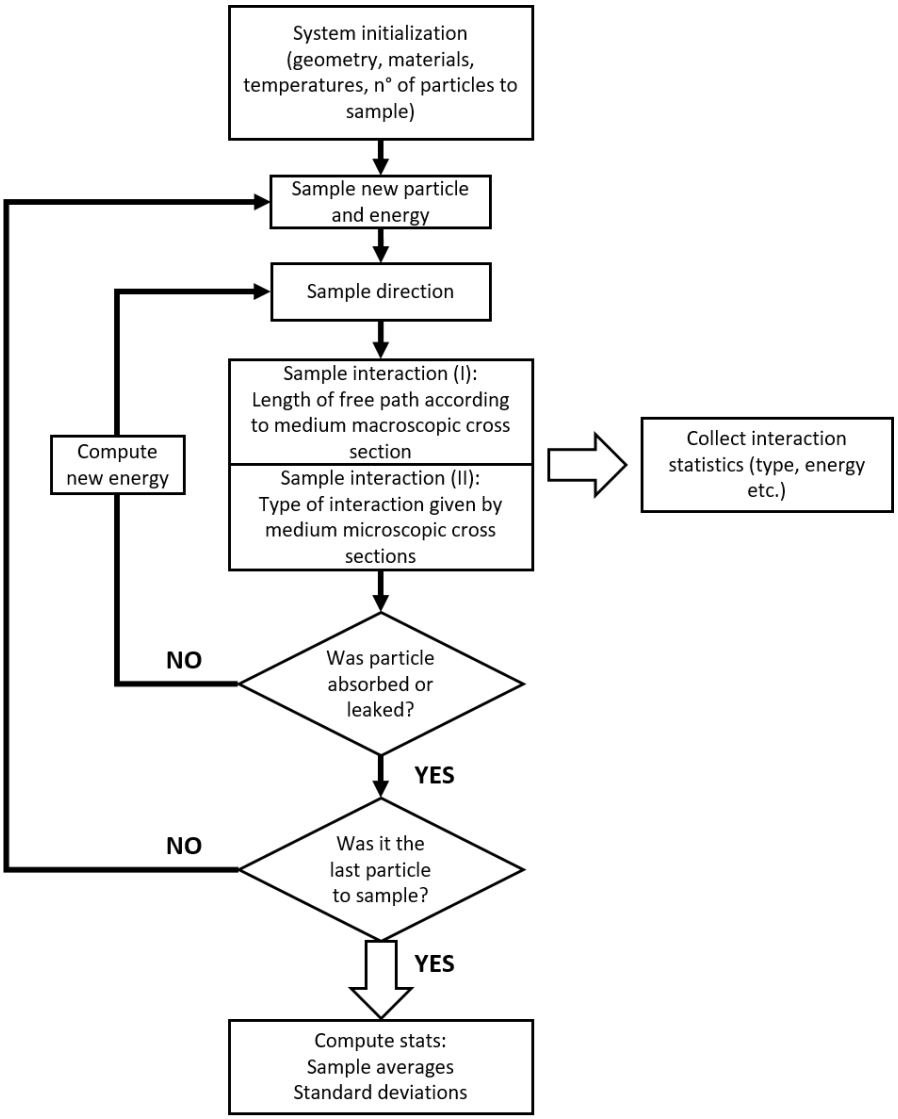

Figure 8: Flow chart of a Monte Carlo particle transport algorithm.

Particles are generated with energy, coordinates and direction that follow a given probability distribution. Random number generation is necessary to address each probability distribution. Particles are then tracked in their random walks up to their disappearance. Mean free paths and interactions with the medium are dominated by particles information and the properties of the medium itself. More specifically, interactions are sampled according to the medium cross sections, which are energy dependent. Example of interactions are elastic scattering, absorption, inelastic scattering, particle expulsion and fission. In the particular case of neutron transport the probability distributions are a function of the particles energy and are provided by cross section libraries. This work relies on the widely adopted and validated ENDF/B-VIII cross section library [110]. Each result is described by a probability distribution that has a Gaussian shape,

according to the central limit theorem. Hence, results are always reported in the form of sample average and standard deviation. Intuitively, the larger the number of sampled particles, the higher the result precision and the lower the standard deviation. The price is however a higher computational cost. In fact, most of the neutron transport codes implement algorithms for core parallelization and simulation acceleration techniques. OpenMC developers have given particular attention to optimized core scalability algorithms [112], [113]. It is worth to mention that the methodology here described is one of the two methodologies usually adopted in Monte Carlo codes for neutronics. It is also the most relevant for nuclear fusion neutronics studies. This type of algorithm is based on the total number of particles to generate and track, which has to be explicitly defined in the simulation initialization. The other methodology is usually used for simulating fission reactor cores and it is based on eigenvalue calculations. The simulation completion is not driven by a given number of random walks to sample. It is determined by the convergence of a given figure of merit instead, usually linked to the reactor criticality.

ARC team developed a detailed model for neutronics simulations using MCNP code [27], [114]. Main features of the model are an Inconel-718 structure, an additional layer of pure beryllium as neutron multiplier, a 90% lithium-6 enriched FLiBe and a 20 cm thick ZrH_2 neutron shield. The most detailed aspect of the model is the geometry. The vessel shows a D-shape cross section and two long-legged divertors. The blanket tank presents a rectangular shape with few indentations to leave room for poloidal field coils. Despite the presence of a detailed model, additional simplified models have been developed. The aim was to provide consistent fast-running and easy-to-parametrize models and it was met with a cylindrical model that mimics the reactor vessel and blanket components [115], [116]. This thesis proposes an improvement to such models still holding the same modeling philosophy and similar characteristics. The strategy is to keep the model as simple as possible mainly for two reasons. First, a simple model is easier to parametrize and faster to run and results comprehension is much more immediate. Second, a simplified model provides more flexible information. In this way, most of the results can be relevant for other tokamaks of similar configuration as well as for future versions of ARC reactor itself. In fact, it is likely that the reactor will experience further adjustments in future design sessions. The model geometry here proposed features a D-shaped section, which is the main improvement with respect previous models. On the third dimension, the toroidal evolution has been avoided in order to stick with simplicity. Instead, a linear extrusion has been preferred. Previous studies did not highlight significant differences between a toroidal and a linear extrusion, especially at this level of detail [115]. A 100 cm linear extrusion of the D-shaped section has been performed. Such length corresponds to a slice that is about 1/20 of the total toroid, considering a major radius of 330 cm. The D-shape has been built in order to match its first wall surface with ARC design one. This is at the core of the

strategy to get ARC-relevant results from simulations. Studies have already confirmed that main results, such as TBR and neutron fluxes are in good agreement with ARC detailed model [115]. The inner D-shape, which corresponds to the first wall, is a semicircle with a 242 cm radius. The resulting surface is offset for building the rest of the model. Vacuum vessel layers directly recall ARC main model ones [27]. From the inside to the outside of the vessel, thicknesses are set as follows: 0.1 cm of first wall (FW), 1 cm of inner structural layer (STR1), 2 cm of FLiBe channel, 1 cm of beryllium neutron multiplier (NMULT) and 3 cm of outer structural layer (STR2). The blanket has been split in two regions: the high field (HF) and low field (LF) regions. The HF region is expected to have little room for the blanket because of the toroidal geometry. First ARC design foresees about 10 cm of blanket on this side [20]. An improved version of ARC suggests instead about 50 cm of blanket [27]. Considering that the neutron and thermal shielding of the central solenoid will be critical issues, this work proposes 20 cm of HF blanket thickness, leaving much room for such additional components. The LF side is much more relaxed in this sense. LF blanket could reach up to 100 cm of thickness in some core regions. However, in other regions it is limited by the presence of neutron shields for the poloidal field coils [27]. For this reason, LF blanket thickness has been set equal to 50 cm, which is the blanket thickness in correspondence of such coils. As this work focuses on the vacuum vessel region, the neutron and thermal shield components have not been included. Figure 9 displays the geometry of the model developed for this work.

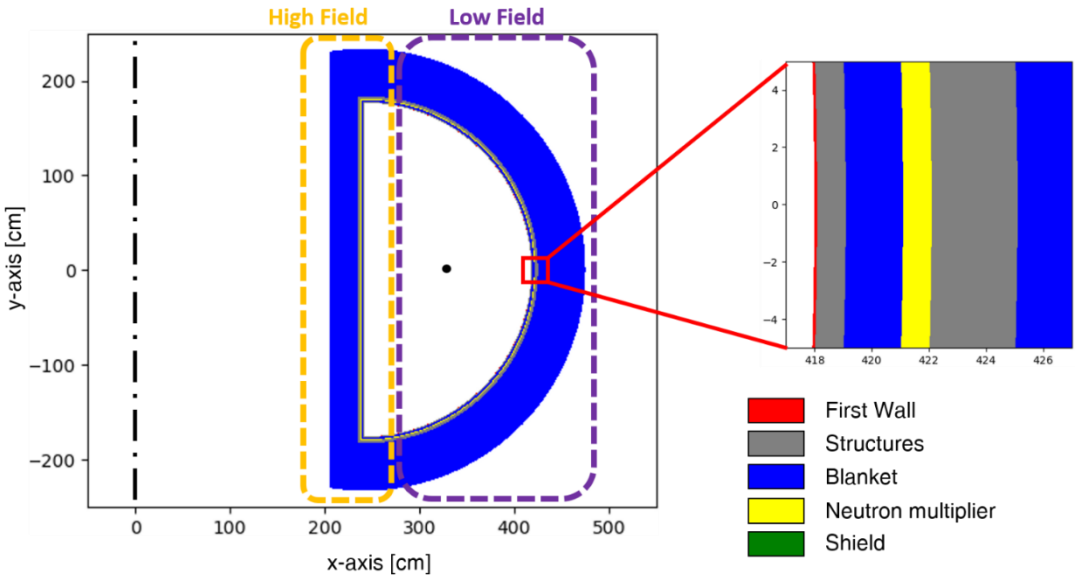

Figure 9: Geometry of the OpenMC neutronics model with a zoom in the vacuum vessel region on the LF side.

Previous studies provided evidence that some structural materials in the vessel could help avoiding the additional layer of beryllium [115], [116]. Still, this work

focuses more on the irradiation behavior of different structural materials and their comparison. Thus, the beryllium layer has been implemented in all the simulations for consistency with the baseline design. It is nonetheless worth to mention that some structural materials may actually experience reduced neutron loads if they allow to remove the neutron multiplier layer. Considering the aim of this thesis, the parametric study is limited to the structural material of the vessel. Previous works already performed crossed sensitivity analysis on liquid breeder compounds and lithium-6 enrichment fraction. Results of the mentioned analysis showed that a FLiBe blanket with 90% enrichment represents the best tradeoff between a sufficiently high TBR, a low neutron load on the vessel and an effective magnet shielding [116]. As OpenMC needs a cell and a material in order to keep tracking particles, the vacuum chamber, which hosts the neutron source, has been modeled as a cell with an extremely low density (i.e. 1e-4 $\frac{g}{cm^3}$) DT compound. Vacuum boundary condition has been set to all the blanket outer surfaces. Namely, all particles that leave the blanket are lost. On the two sides of the D shape feature a reflective boundary condition in order to simulate the continuity of a toroidal shape. All the model surfaces and cells have been carefully designed in order to obtain a watertight geometry. The neutron source has been modeled as an isotropic box source 100 cm height, with a 20 cm edge and centered at the D center, which is 121 cm from the HF FW inner surface. The source provides 14.06 MeV neutrons. The source intensity has been set equal to 1 neutron to simplify the scalability with the fusion power. However, it is possible to compute the actual intensity the model should have. ARC should provide about 525 MW of fusion power that corresponds to a neutron yield of roughly 1.86e+20 $\frac{n}{s}$. Since this model represents a slice of the whole reactor, its source intensity should be equal to 9e+18 $\frac{n}{s}$. The model has a homogeneous temperature of 900 K. Material properties relevant for neutronics have been listed in Table 4. The table provides also the names of the cells that have been filled with the corresponding material. It is necessary to specify that for WTaVCrTi an ideal equimolar composition has been taken and, because of the lack of data in literature, the material density has been computed according to the apparent density formula (Eq. 3).

Table 4: List of materials, composition and density modeled for the neutronics analysis.

Material	Composition [at. %]	Density $\frac{g}{cm^3}$	Model cell
W	W 100	19.3	FW
Be	Be 100	1.85	Nmult
FLiBe	F 57.14 – Li 28.57 – Be 14.29	1.96	channel –

			blanket
Eurofer97	Fe 88.66 – Cr 9 – W 1.5 – Mn 0.4 – V 0.2 – C 0.11 – Ta 0.07 – Ti 0.01 – impurities	7.798	STR1 – STR2
Inconel718	Ni 53 – Cr 19.06 – Fe 18.15 – Nb 5.08 – Mo 3.04 Ti 0.93 – Al 0.52 – Co 0.11 – C 0.02 – Cu 0.02 - impurities	8.19	STR1 – STR2
V-4Cr-4Ti	V 92 – Cr 4 – Ti 4	6.06	STR1 – STR2
WTaVCrTi	W 20 – Ta 20 – V 20 – Cr 20 – Ti 20	10.74*	STR1 – STR2

*According to apparent density formula

$$\rho_{mix}^{T} = \sum_{i} X_i \cdot \rho_i^T \qquad \text{Eq. 3}$$

where ρ is the density, T is the set temperature and X is the molar concentration of the ith element. 1e+5 particles and 10 batches are sampled for each simulation in order to reach results relative standard deviations always on the order of 1e-3 or lower. No acceleration methods nor variance reduction techniques were adopted as the model needs on the order of tens of minutes to run. Lastly, the ENDF/B-VIII cross section library has been adopted for nuclear data [110]. Most important results to tally are the neutron flux and relative spectrum on the chamber structural layers, which are of main interest to start evaluating the irradiation magnitude and the damage. Fluxes and spectra are also necessary for more detailed damage and activation studies. In addition, particles production such as H1, H2, H3, He3 and He4 generation rates should be tallied in order to get information about swelling likelihood and magnitude. Lastly, additional tallies include tritons transmutation rate in the channel and blanket cells and the current leaking the blanket surface. The former tally is necessary to evaluate the impact of different structural materials on the machine TBR, the latter tally evaluates possible neutron shielding effects. Table 5 summarizes the tallies applied in the model and their relative cell or surface.

Table 5: List of the main tallies applied in the model.

Tally	Units	Type	Object
Neutron flux	$\left[\frac{n}{source\ particle \cdot cm^2 \cdot s}\right]$	Cell tally	STR1, STR2

Neutron energy spectrum	$\left[\frac{eV}{source\ particle}\right]$	Cell tally	STR1, STR2
(H1, H2, H3, He3, He4) particles production rate	$\left[\frac{particle}{source\ particle}\right]$	Cell tally	STR1, STR2
Tritons production rate	$\left[\frac{t}{source\ particle}\right]$	Cell tally	Channel, blanket
Neutron current	$\left[\frac{n}{cm^2 \cdot s}\right]$	Surface tally	Outer blanket

3.4 Results

Neutronics results are here presented. This section displays first the figures that are affected by structural materials even though that was not part of the material required functions. It is the case of the TBR (Figure 10 and Table 6). Tritium breeding ratio is of crucial importance for the reactor fuel cycle self-sustainability, and it is heavily affected by the chamber structural material. Figure 10 displays the tritium production tally for 1 source particle. It is clear that most of the tritium is bred in the channel and in the innermost regions of the tank, which is in good agreement with previous studies [27], [116].

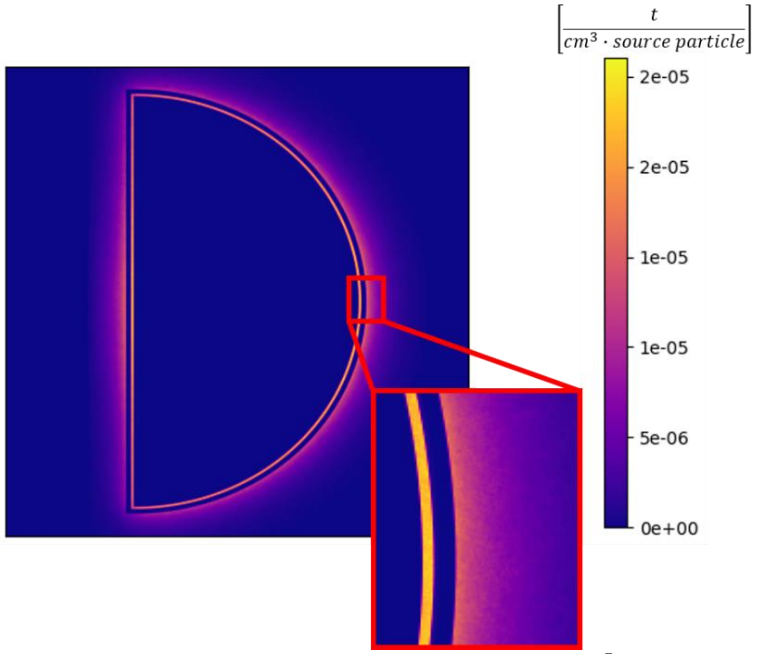

Figure 10: Mesh results for the tritium transmutation rate $\left[\frac{t}{cm^3 \cdot source\ particle}\right]$.

The overall tritium breeding ratio is made explicit in Table 6. Inconel has worst performance in terms of tritium production, while V-4Cr-4Ti maximizes the fuel breeding.

Table 6: Tritium Breeding Ratio results (sample average and standard deviation).

Material	TBR	Std. dev.
Eurofer97	1.15	1.33e-3
Inconel718	1.04	1.42e-3
V-4Cr-4Ti	1.21	1.43e-3
WTaVCrTi	1.12	9.87e-4

Neutron shielding is another secondary effect that can be affected by the type of structural material applied. The reactor coils are the first components that require an effective neutron shielding. As magnets are placed outside the blanket tank, Figure 11 displays the neutron current exiting the blanket outer surface from the high-field and low-field regions. V-4Cr-4Ti seems to perform worse in this sense. Still, currents are comparable for all the materials and the values stand in the same order of magnitude.

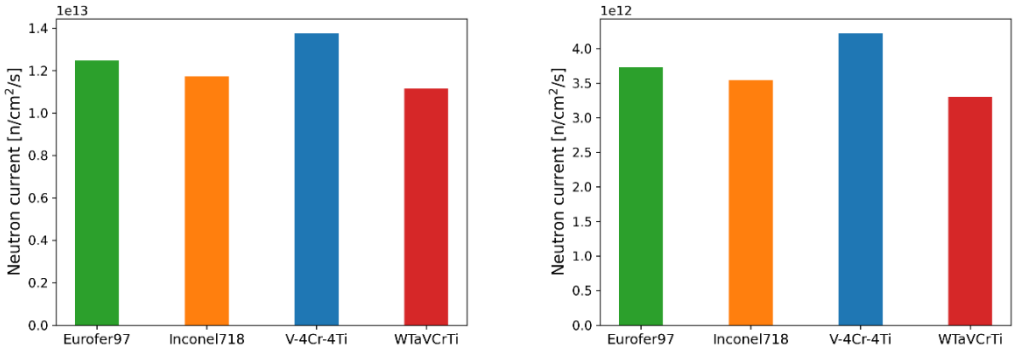

(a) *(b)*

Figure 11: Neutron current exiting the blanket from the high field (a) and low field (b) sides.

Finally, results regarding the structural materials themselves and information on the irradiation effects are here presented. Figure 12 displays the main quantities of interest that the OpenMC code can provide in this framework. STR1 and STR2 cells have very similar results. Therefore, it has been chosen to show STR1 values as reference, seeing as how STR1 is closer to the neutron and heat source and more endangered. Figure 12 (a) and (b) show the cell fluxes and relative spectra

for the different materials. Values are very similar in both figures. It is possible to notice that the high entropy alloy has a slightly lower moderating capability, probably because of the much higher molecular weight due to the Ta and W presence. Figure 12 (c) and (d) show the gas transmutation rate occurring in the material itself. Hydrogen and helium are the most transmuted gas by far.

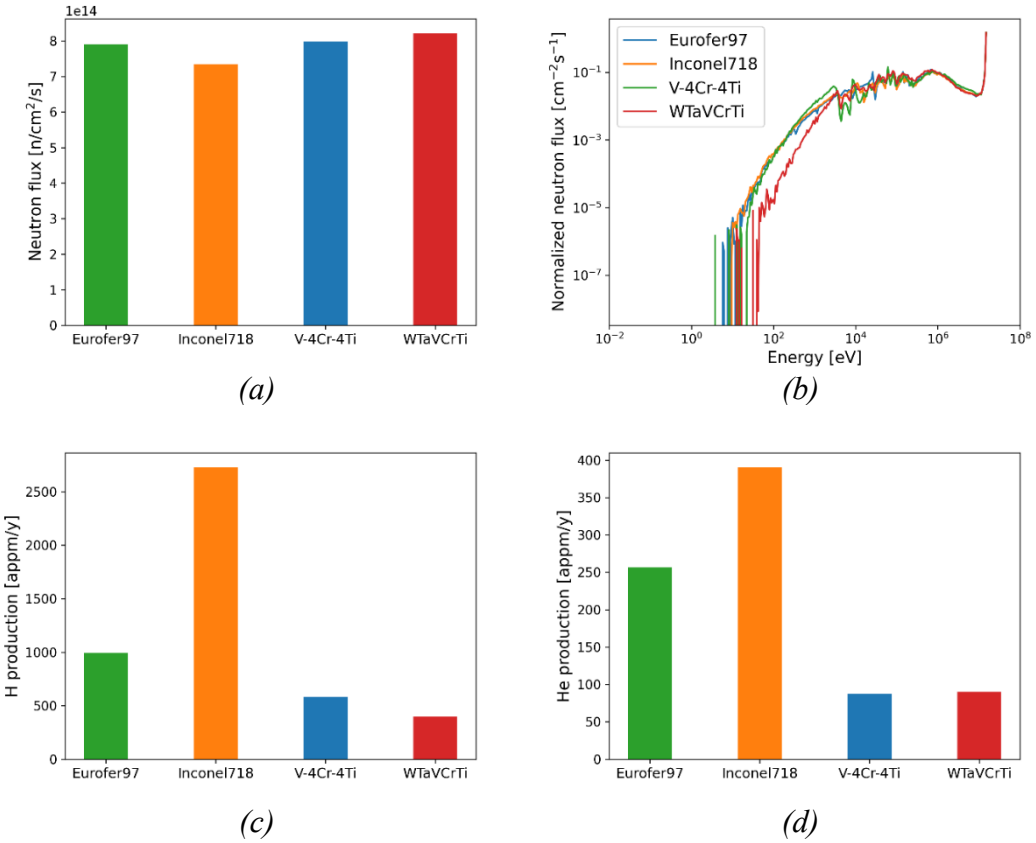

Figure 12: Figures of merit for irradiation damage tallied on the STR1 cell. (a) neutron flux, (b) neutron flux energy spectra, (c) hydrogen production rate and (d) helium production rate.

Results suggest that irradiation effects on the materials considered are qualitatively similar. An exception to this statement can be made for the TBR and the gas transmutation rate. However, it is necessary to perform a deep discussion on such results in order to identify the actual differences and the possible consequences of the material choices.

3.5 Discussion

It is necessary to specify that this work is interested on the order of magnitude of neutronics results rather than the specific values. This is given by the fact that the model has been generalized as much as possible and some design features of ARC have not been chosen yet. Considering the modeling choices, it is worth to

acknowledge that the OpenMC algorithm for parallelization and the simplicity of the model have successfully managed to speed up the process. The simulation time was kept below very few tens of minutes while achieving maximum standard deviations on the order of 1e-3.

Because of the thin nature of the vacuum vessel structure, results here obtained are similar for different materials applied. Table 6 shows that all the structural materials allow for a TBR > 1, which is acceptable in ideal conditions. However, considering modeling uncertainties and tritium leakage and losses, TBR requires to be higher than 1.10-1.15 [117]. Inconel718 is the only structural material that does not meet such requirement. It is likely that an Inconel-based structure would require additional actions to effectively multiply neutrons and enhance the tritium economy. This holds particularly true when it comes to consider also the material tritium absorption [118]. It seems that Inconel would absorb a particularly high tritium inventory from the blanket. VCrTi systems on the other hand show a TBR high enough to open to the possibility of removing the additional neutron multiplier layer [115], [116]. Figure 12 (b) shows that the vessel structures experience extremely fast neutrons with a huge peak at 14.06 MeV. According to the main cross sections (Figure 6), V and Fe do show a slightly higher probability of multiplying neutrons and a lower absorption capability. This can be combined to a lower material density which leads to fewer interactions. These aspects allow Fe- and V-based alloys to enhance the reactor TBR with respect Ni-based materials. Similarly, Ta and W hold a much higher multiplying capability than the other elements considered. Nevertheless, they have a high absorption rate at lower neutron energies and they raise the material density as well. A sensitivity analysis on Ta and W concentrations in the HEA should be carried out in order to optimize the TBR and provide tritium production rate curves as a function of the HEA composition. Figure 10 shows that almost all the tritium is bred in the very first centimeters of the blanket. This is true especially in this case where the breeder is a 90% Li-6 enriched FLiBe [116]. A reduced thickness blanket can leave space for neutron shields, where needed, which is essential for the magnets integrity in compact tokamak designs. In fact, despite being a breeder with good shielding capabilities, 20 cm of FLiBe reduce neutron current only by one order of magnitude, while 50 cm of thickness reduces it by two orders of magnitude (see Figure 11). In this configuration, a fluence on the order of 1e+20 $\frac{n}{cm^2}$ per full power year would reach the high field side magnets. Such a high fluence is not sustainable [19], [119]. On the other hand, considering ARC design provided by Kuang et al. [27], 20 cm of blanket would leave tens of centimeters for neutron and thermal shields designed with ad hoc functional materials.

For what concerns the irradiation damage, materials should not be chosen on the basis of the flux experienced, seeing as how it does not change much from a material to another. They rather should be chosen on the basis of the element

cross sections in comparison with the neutron energy spectrum. It is clear that Fe- and Ni-rich materials transmute much more gases than other transition metals in the ARC neutron spectrum. Gas transmutation in Ni-based alloys can be one order of magnitude higher than Fe- and Ni-poor materials. This can be a key factor in the choice of structural materials as gas transmutation and swelling are expected to be particularly intense when it comes to evaluate neutron damage in fusion energy domains [111]. Despite that, it is important to acknowledge that gas transmutation rates are not sufficient to assess the swelling phenomenon in a material. Indeed, although nickel can lead to accelerated swelling [120], Inconel complex microstructure owns effective mechanisms that work as gas atom sinks and that improve swelling resistance [121]. It is possible that this behavior would be observed also in some HEAs because of their likely microstructural complexity. This aspect highlights the necessity for experimental campaigns aimed to assess the actual swelling resistance of materials in fusion conditions.

3.6 Conclusions

This chapter focused on the evaluation of structural materials nuclear properties and the analysis of the behavior of such materials in ARC neutronics conditions. In this respect, the main issues identified are the irradiation damage on the material and its tendency to affect the machine tritium breeding ratio. Damage in particular is often a function of the neutron flux and, especially in the case of fusion reactors, transmuted gas buildup. Cross sections relevant for the mentioned aspects have been analysed. Cross sections for neutron capture and multiplication are of main interest for the TBR, while gas transmutation cross sections are relevant for damage, swelling and embrittlement mechanisms. Cross sections suggested that Ni, Ta and W would absorb a high quantity of neutrons in the fusion-relevant energy range. Still, Ta and W showed a good multiplication capability over a wide range of energy as well. In addition, Ni and Fe displayed a high gas transmutation probability with respect the other transition metals. After the first qualitative considerations a versatile and fast-running neutronics model of the reactor core has been presented. The model perfectly accomplished its purposes as the simulations run fast, it eased the parametrization and results were accurate enough for the analysis performed and in good agreement with previous studies. From neutronics results it is possible to state that few centimeters of different structural materials do not affect most of the figures of main interest. The most affected are the TBR and the gas transmutation rate in the material itself. Results of these quantities confirmed what cross sections suggested. Inconel718 would need additional neutron multipliers for reaching a sufficient value of TBR, which is set above the value of 1.10. On the contrary, V-Cr-Ti systems may allow to remove the beryllium layer present in the baseline VV design. It is also clear that MPEAs could optimize the TBR value by changing the concentration of some elements. Regarding radiation damage it was possible to explore the gas transmutation rates in view of the swelling mechanisms. In this sense, without

additional information coming from complex microstructure mechanisms, it seems that alloys with low concentrations of Fe and, especially, Ni should be preferred. On the other hand, materials with high concentrations of V, Cr, Ti and, especially, the refractory Ta and W should be applied in order to enhance the reactor fuel cycle and reduce the risk of high swelling rates.

Additional effects of neutron irradiation on materials regard the induced radioactivity. Despite induced radioactivity is not of main importance for the structure integrity, it is considered a key aspect of the fusion projects as it affects the reactor safety as well as its attractiveness. Chapter 4 of this thesis will indeed address these issues in ARC-like conditions.

Chapter 4

Irradiation analysis

4.1 Introduction

The radiation environment of a reactor affects the structures themselves. This chapter focuses on the effects of radiations on structural materials, like Chapter 3 of this work focused on the effects of structural materials on core neutronics. From an engineering viewpoint, neutron irradiation causes two major issues on materials, namely radiation induced activation and radiation damage. This chapter focuses mainly on induced activation and reactor radioactivity. Despite the nuclear reaction of D and T fusion does not produce radioactive elements, a fusion reaction is still expected to be a source of radioactive materials. Radioactivity in fusion reactors comes from two main sources. The first one is part of the fusion fuel, namely tritium. Tritium will be just introduced here as it is not of main interest for this work, but it is worth to be mentioned because of its importance in the whole machine and plant. Tritium is produced and burned inside the reactor and it has a relatively short half-life (i.e. 12.3 years). Thus, it is not considered as a major problem for radioactive waste while it is of main concern in case of accident and release. As part of the fuel, tritium is unavoidable in the reactor but it is possible to apply several techniques in order to minimize the tritium inventory and confine it within several barriers [117], [122]. The second source of radioactivity is given by core materials that experienced neutron irradiations. Neutron induced radioactivity is caused by transmutation. Neutron absorption and anelastic scattering cause an atom to change atomic mass, ultimately becoming another isotope or transmuting in another element of the periodic table. Resulting atoms are often unstable, which dramatically increases the material radioactivity. Activated materials are of main concern both for safety and waste reasons. Safety and radioactive waste aspects are known for heavily affect attractiveness and economics of nuclear reactors. Nevertheless, in fusion reactors it is possible to

effectively reduce and minimize the amount of radioactive waste and the reactor inventory by carefully choosing core materials and applying optimization techniques [109]. This chapter addresses the effects of irradiation on the structural materials analysed throughout this thesis in terms of induced radioactivity. Low activation materials will be identified, and additional optimization techniques will be applied in order to get as low activation as possible. In addition, radioactivity limits are proposed in order to ease the management of radioactive waste for fusion industry. The goals are to provide an easy procedure for predicting and assessing radioactive induced activation and to identify the most promising structural materials able to reduce the radioactivity problem. Lastly, the main figures of merit that characterize radiation damage (i.e. dpa and gas transmutation) are assessed and confronted with the same results presented in Chapter 3.

4.2 Methodology

The analysis takes advantage of the FISPACT-II inventory package [123]. FISPACT-II is a software developed by UK Atomic Energy Authority at the Culham Science Center. FISPACT is mostly used to compute the inventory of radioactive materials produced by nuclear reactors. Knowing exactly the type and the amount of radioactive material in a power plant is a necessity of main importance for both computing source terms for safety reasons and developing an effective radioactive waste management strategy. FISPACT-II solves the rate equation (Eq. 4) for all the species (elements, isotopes) involved a given inventory.

$$\frac{dN_i}{dt} = \sum_j (\lambda_i^j + \sigma_i^j \cdot \phi^{int}(t)) \cdot N_j \qquad \text{Eq. 4}$$

where N_i is the inventory of nuclide i at time t, λ_i^j is the decay constant of nuclide j producing i, σ_i^j is the reaction cross section on nuclide j producing i and ϕ^{int} is the time dependent neutron flux experienced by the inventory of nuclides i [123].

In order to solve Eq. 4, FISPACT-II requires the initial inventory of elements that experience the neutron flux, a flux history (i.e. time dependent flux magnitude and energy spectrum), a library for the decay constants and cross section libraries totally analogous to libraries described in Chapter 3. The code is able to produce several time-dependent results on both irradiation phase and post-irradiation decay phase (i.e. cooling). Quantities such as specific activity (SA), contact dose rate (CDR) produced are of main interest for this work. Such quantities are sufficient for a comparison between irradiated materials. They also provide basis information to start setting up a radioactive waste management strategy. Results such as ingestion and inhalation doses are not considered in this work as materials studied are expected to stand in solid state in place in the reactor or in eventual casks for disposal. Such quantities could be nevertheless

useful in future safety-related works in order to compute source terms in case of accidents that involve components melting or breaking. Specific activity is the sum of the overall activity of all radionuclides composing a kg of material in the model. Contact dose rate computes the contact dose caused by an infinite slab of material in the model if put in contact with a subject directly on the skin. Alpha and beta particles are considered as stopped by the first layer of the skin and then neglected. Contact dose rate is computed as in Eq. 5 [123]:

$$CDR = C \cdot \frac{B}{2} \cdot \sum_{i}^{N_\gamma} \frac{\mu_a(E_i)}{\mu_m(E_i)} \cdot S_\gamma(E_i) \qquad \text{Eq. 5}$$

where C=3.6e+9·|e| is the conversion factor from $\frac{MeV}{kg \cdot s}$ to $\frac{Sv}{h}$ (with |e| being the electron charge). B=2 is the buildup factor. N_y is the number of energy group in the γ spectrum. μ_a, μ_m and S_y are the air mass energy absorption coefficient, the material mass energy attenuation coefficient and the rate of γ emission as a function of the average energy E_i of the i-th group, respectively [123].

This chapter main goal is to analyse the main effects of neutron irradiation on the structural materials considered in this work, namely Eurofer97, Inconel-718, V-4Cr-4Ti and WTaVCrTi. A worst-case scenario in terms of activation is modeled. More specifically, the material is considered at the maximum irradiation conditions. 1 m3 of material is modeled as if it was placed in the inner wall of ARC vacuum vessel. Neutron energy spectra are provided from the OpenMC model described in Chapter 3. The neutron flux in the inner wall of the vacuum vessel is averagely around 8.0e+14 $\frac{n}{cm^2 \cdot s}$, as resulted in Chapter 3. Flux is here modeled equal to 1.0e+15 $\frac{n}{cm^2 \cdot s}$ for all materials to get a more generalized comparison still standing in ARC conditions. One full power year (FPY) is considered as reference time of continuous irradiation. Outputs are recorded for about 300 years of cooling time.

The analysis is divided in 4 steps. In the first step pure elements composing the alloys are irradiated alone (Fe, Ni, Ti, V, Cr, W and Ta) with particular attention given to their natural isotopes. Table 7 summarizes element isotopes and their natural abundancy.

Table 7: List of main elements composing the alloys considered, their isotopes and natural abundances.

Element	Isotope	Abundance [%]	Element	Isotope	Abundance [%]
Fe	Fe-54	5.85	Ti	Ti-46	8.25
	Fe-56	91.75		Ti-47	7.44
	Fe-57	2.12		Ti-48	73.72
	Fe-58	0.28		Ti-49	5.41

Ni	Ni-58	68.08	Ti	Ti-50	5.18
	Ni-60	26.22	V	V-50	0.25
	Ni-61	1.14		V-51	99.75
	Ni-62	3.63	Ta	Ta-181	100
	Ni-64	0.93	W	W-180	0.12
Cr	Cr-50	4.35		W-182	26.5
	Cr-52	83.79		W-183	14.31
	Cr-53	9.5		W-184	30.64
	Cr-54	2.36		W-186	28.43

In the second step Alloys are considered in the same composition as they have been modeled in Chapter 3 and they are listed here in Table 8 as well. FISPACT-II can also provide few basis irradiation damage figures of merit (dpa and gas production rate), in this step such quantities will be assessed and compared with OpenMC results of Chapter 3.

Table 8: List of materials, composition and density.

Material	**Composition [at. %]**	**Density** $\frac{g}{cm^3}$
Eurofer97	Fe 88.66 – Cr 9 – W 1.5 – Mn 0.4 – V 0.2 – C 0.11 – Ta 0.07 – Ti 0.01	7.798
Inconel718	Ni 53 – Cr 19.06 – Fe 18.15 – Nb 5.08 – Mo 3.04 - Ti 0.93 – Al 0.52 – Co 0.11 – C 0.02 – Cu 0.02	8.19
V-4Cr-4Ti	V 92 – Cr 4 – Ti 4	6.06
WTaVCrTi	W 20 – Ta 20 – V 20 – Cr 20 – Ti 20	10.74

In the third step, optimization techniques are applied to reduce the radioactivity of the most promising alloys. Isotopic tailoring (it) is the first technique applied. It is assumed that it is possible to enrich each alloying element with its lowest activation natural isotope, which is identified in the first step of the analysis. Enrichment techniques are not new to the nuclear industry. U-235 enrichment is particularly common in both energy and military industries [124]. Boron-10 enrichment is often used for neutron shield optimization [125]. W-184 enrichment is sometimes applied to reduce neutron absorption in core components [126]. An additional technique is the radioactive gas removal (degas), proposed in this framework [127]. It is assumed that it is possible to remove gases from

irradiated materials in a reprocessing phase. Ideally, it could be possible to activate gas desorption from temperature increase. Nevertheless, tailoring should be preferable as it prevents radioactivity while degas is more of an inventory separation.

The fourth step assesses the effect of impurities on the most promising materials. The analysis that includes impurities is performed on non-optimized materials. Optimization techniques are virtually viable but have yet never been commercially applied on large and standardized components. Hence, while the case study with optimization aims to the lowest activation achievable, the case with impurities shows what to actually expect in a commercial compact tokamak in terms of activated materials. Impurity type and concentration are provided by a literature analysis. Impurity analysis will not be performed on Inconel as nickel is a well-known high activation element and it is often considered an impurity in other non-nickel alloys [109]. Hence, the effect of impurities in Inconel activation would not be observable and would not affect the overall induced radioactivity by no means. According to literature, impurities typically identified in Fe-Cr systems such as Eurofer97 and ODS-Eurofer97 are Si, Ni, Mo, Cu, Nb, Al, Co, Sn, Zr and Sb [109]. V-Cr-Ti systems typical impurities are C, N, O, Al, Si, Fe, Ni, Cu, Nb, Mo and Te [109]. For the refractory HEA not enough literature data were found about impurities. However, tantalum and tungsten samples have similar impurities to V-Cr-Ti systems [128], [129]. Hence, for WTaVCrTi alloy the same configuration of impurities of V-4Cr-4Ti is assumed. Common impurity concentrations are listed in Table 9.

Table 9: Typical impurity concentrations for Eurofer97, V-4Cr-4Ti and WTaVCrTi alloys.

	Concentraton [wppm]		
Impurity	**Eurofer97**	**V-4Cr-4Ti**	**WTaVCrTi**
C	-	50	50
N	-	100	100
O	-	200	200
Si	500	300	300
Fe	-	100	100
Ni	50	100	100
Mo	50	25	25
Cu	50	5	5
Nb	10	1	1
Al	100	100	100

Co	50	-	-
As	50	-	-
Sn	50	-	-
Zr	50	-	-
Sb	50	-	-
Te	-	20	20

Lastly, it is necessary to discuss the limits of radioactivity considered in this work. The choice is to compare induced activation results with the most stringent limits on irradiated material management, namely recycling limits proposed for nuclear fusion materials [130], [131]. Recycling limits are here explained:

- Recycling limit in the nuclear industry ("in-plant recycle"): 1e-5 $\frac{Sv}{h}$ on the contact dose rate. It corresponds to 20 $\frac{mSv}{y}$ in the conservative case of direct contact with the material for 8 hours per day, 5 days per week. 20 mSv/y is the dose limit for radiation workers worldwide.
- Recycling limit in the industry ("out-plant recycle"): 1e-6 $\frac{Sv}{h}$ on contact dose rate. corresponds to the 1 $\frac{mSv}{y}$ regulatory limit for non-nuclear workers. Again, assuming a contact time limited to normal working hours.
- Comparison with average natural background ("comparable to background"): 1.14e-7 $\frac{Sv}{h}$, as reference to the natural background average dose (1 $\frac{mSv}{y}$), assuming a 24/7 contact. Although this is not an actual recycling index, it is considered useful to compare the dose caused by a direct contact with the irradiated material with the dose an average individual directly takes.

The target is to minimize the radioactive waste. As such, this chapter focuses on the 10-100 years of cooling time interval in order to leave the high-activity and short-lived nuclide to decay. Reaching low radioactivity within 100 years from shutdown is one of the goals set for fusion waste [109].

4.3 Results

In this section all results of the FISPACT-II simulations are shown. Vertical purple areas have been set at 10, 50 and 100 years of cooling as time references. Green areas have been set corresponding to recycling limits and natural background reference.

4.3.1 Alloying element results

SA and CDR of Fe and Ni are displayed in Figure 13. As previously mentioned, nickel is particularly sensitive to activation and generates long lived nuclides. Ni-58 and Ni-64 generate Ni-59 and Ni-63, respectively. Such nuclides are characterized by relatively low energy β decay and relatively long half-lives, being principal components for the SA but not for the contact dose rate. High CDRs after 100 years are dominated by Co-60, which is characterized by a very high energy β decay (2.82 MeV). Ni-62 generates Ni-63, which causes a high activity but does not affect the CDR so heavily, letting the material reach the first recycling limit. Iron, on the other hand, has two isotopes that could reach very low values of activity and dose (i.e. Fe-56 and Fe-57). Fe-56 is also the most abundant isotope of iron (about 92%). There is just one iron isotope that does not reach any recycling limit in the long term, namely Fe-54. Irradiated Fe-54 generates Mn-53, which is the cause of 99.98% of the specific activity after 50 years of cooling. Mn-53 decays by electron capture and has a half-life of 3.74e+6 years.

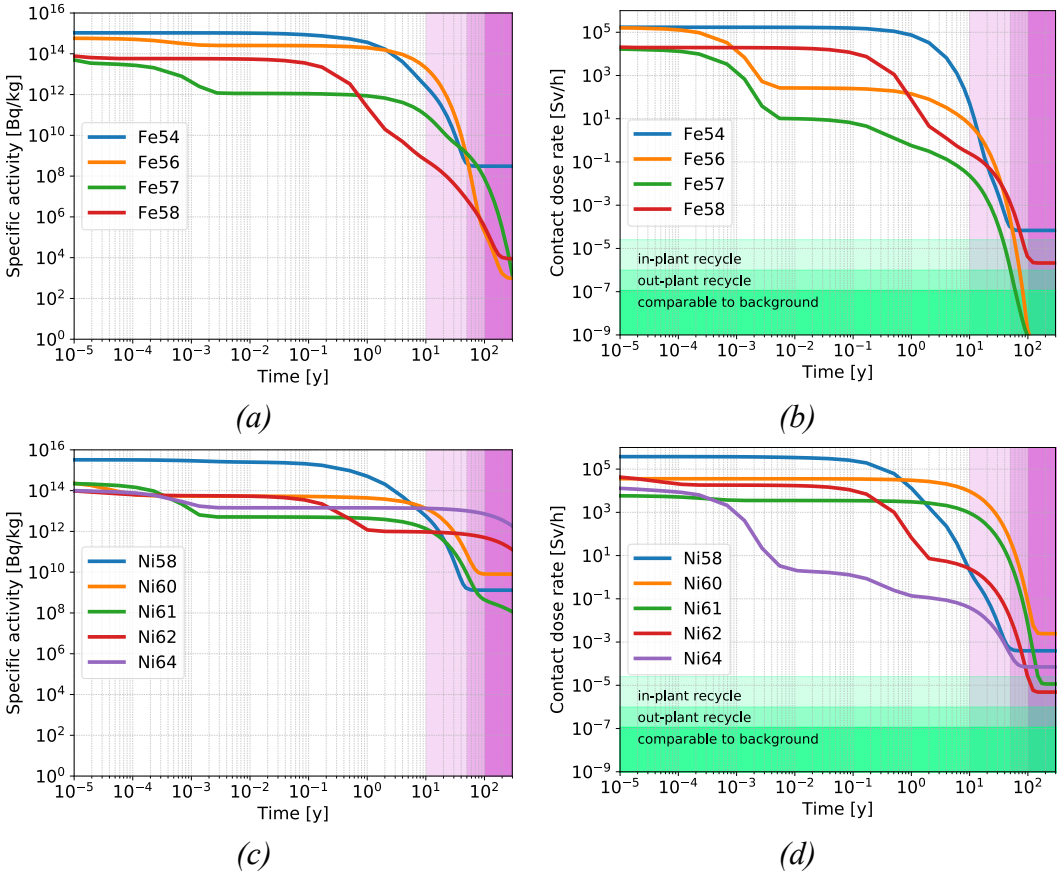

Figure 13: Specific activity and contact dose rate of iron (a) and (b). Specific activity and contact dose rate of nickel (c) and (d).

Figure 14 depicts SA and CDR of irradiated V, Cr and Ti natural isotopes. V-Cr-Ti systems are known for being the lowest activation alloys. V and Cr reach

extremely low values of activity and dose rate in few decades of cooling. Also, most Ti isotopes can be considered as low activation. At 10-300 years of cooling time, the CDR of all Ti isotopes is dominated by K-42, daughter of the short-lived Ar-42. Heavier Ti isotopes are less likely to be teared down to Ar-42 by neutrons than lighter Ti isotopes, which is why heavier isotopes are characterized by lower contact dose rate.

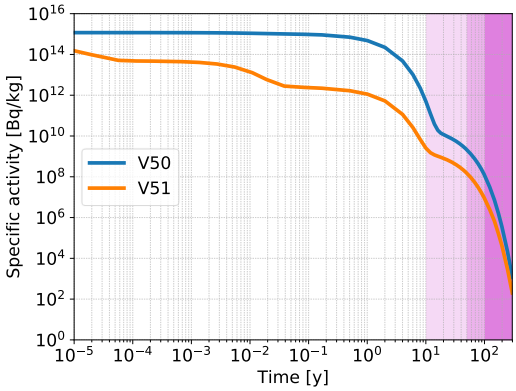

(a)

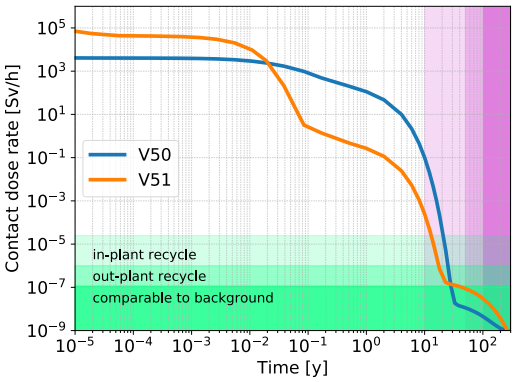

(b)

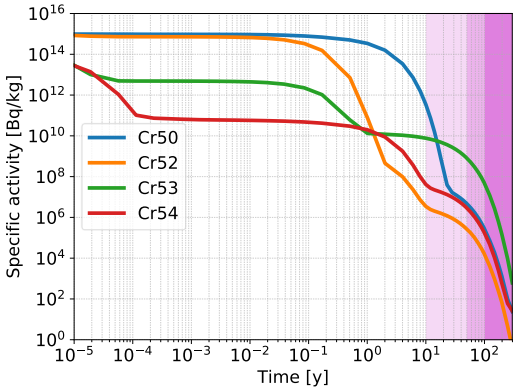

(c)

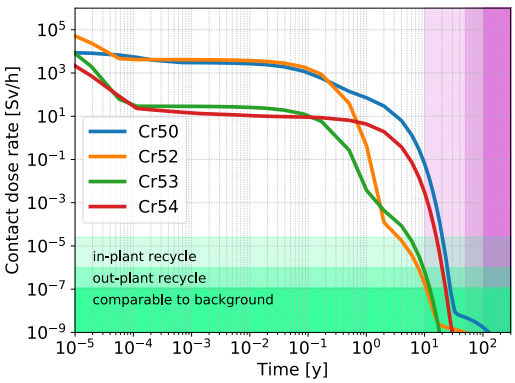

(d)

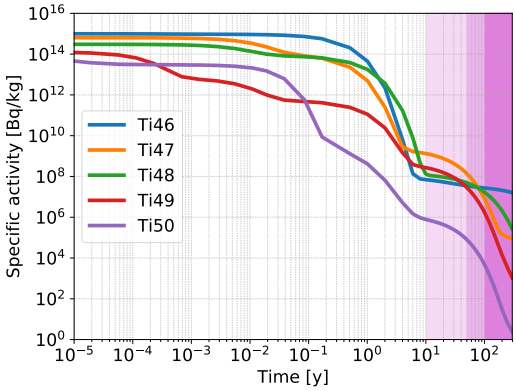

(e)

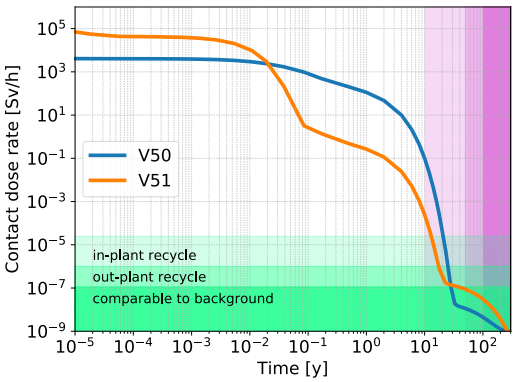

(f)

Figure 14: Specific activity and contact dose rate of vanadium (a) and (b). Specific activity and contact dose rate of chromium (c) and (d). Specific activity and contact dose rate of titanium (e) and (f).

Figure 15 shows activity and dose rate of Ta and W after 1 FPY of irradiation in ARC-like conditions. SA of irradiated tantalum at long term cooling (above 100 years) is dominated by tritium and metastable Hf-178. Likewise, light W isotopes activation and dose are dominated by tritium and metastable Hf-178. Like Ti isotopes, ligher W elements are more likely to get teared down to lighter and unstable nuclides. This time the (n, t) reaction (tritium transmutation) has a non-negligible effect.

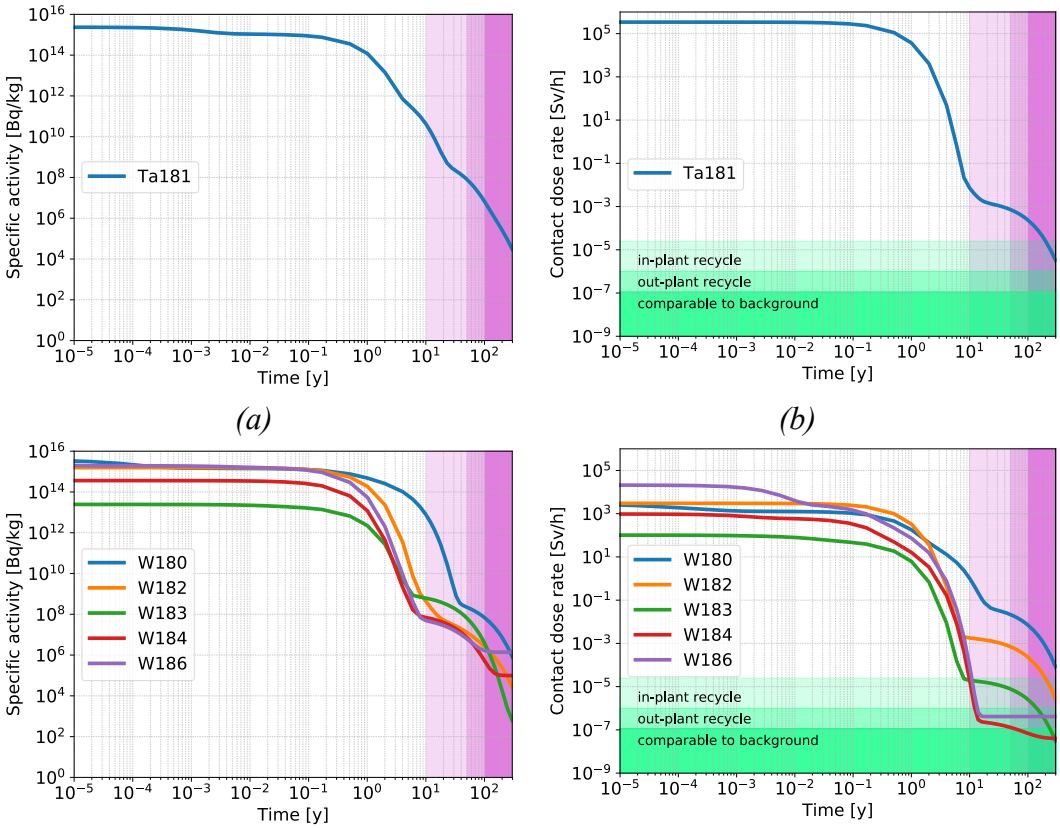

Figure 15: Specific activity and contact dose rate of tantalum (a) and (b). Specific activity and contact dose rate of tungsten (c) and (d).

4.3.2 Material results

Figure 16 shows the results relative to the considered alloys without impurities. As previously anticipated, Inconel SA and CDR stabilize at values that are more than 2 orders of magnitude higher than the other alloys. Alongside nickel, the relatively high concentration of Nb and Mo worsen the performance of such superalloy. Eurofer97, V-4Cr-4Ti and WTaVCrTi SA and CDR decrease much more. CRD in

particular gets very close to recycling limits in about a century of cooling time. The CDR of the high entropy alloy decreases slower than the V-Cr-Ti system, this is due to the additional W and Ta elements as well as a higher concentration of Ti.

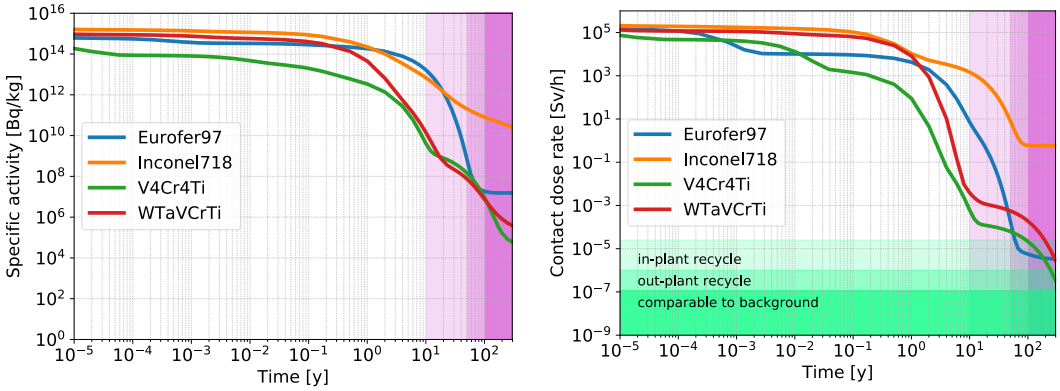

(a) *(b)*

Figure 16: Specific activity and contact dose rate of the studied alloys in pure conditions (a) and (b).

4.3.3 Optimization techniques

Two types of optimization techniques have been applied to Eurofer97, V-4Cr-4Ti and WTaVCrTi: isotopic tailoring (it) and radioactive gas removal (degas). Isotopic tailoring is applied to elements that have some isotopes that experience a lower activation than others. It is assumed to be doable with a 100% of isotope separation. Results shown that Fe-57, Ti-50 and W-184 provide the lowest SA and CDR among other isotopes and it is applied by replacing Fe, Ti and W with only such isotopes. Cr has not been included in the tailoring process as all of its isotopes can be considered low activation and the effect would not be visible in the 10-100 years interval. The other optimization technique applied is the radioactive gas removal. It is applied to the alloys that are already tailored in order to gradually achieve the lowest values of induced radioactivity virtually achievable. Figure 17 displays the SA and CDR of alloys with the mentioned optimization techniques applied. Isotopic tailoring has shown to be effective in most cases reducing both SA and CDR in the 10-100 years range. An exception is observable in the case of tailored Eurofer97. Despite its CDR lowers, the SA is higher of the non-optimized Eurofer97 in the 50-100 years span. This is due to the fact that Fe-57 transmutes much more tritium than the more abundant Fe-56. Tritium takes over activity in the 50-100 years region but its low energy β decay does not affect the CRD. Tritium effect is indeed removed in the degas process. Eurofer97 and the HEA CDRs do not change in the case of it and it+degas. Non-gaseos radionuclides take over the CDR in the whole 0-300 years region. VCrTi systems can take advantage of both tailoring and gas removal. In the case of isotopic tailoring it is possible to prevent the formation of K-42 daughter of Ar-42, which transmutes from light titanium isotopes. Ar-32 has a 32 years half-life and relatively low energy β decay, but the daughter K-42 has a low half-life (12

hours) and high energy β decay (3.5 MeV). Activity of pure VCrTi systems is dominated by tritium in the 10-300 years span, which can be removed by the degas technique. The Ar-42/K-42 effect is visible also in the WTaVCrTi HEA. However, the presence of W and Ta and their transmutation products reduces such effect. Most of the SA and CDR is caused by tantalum activation, which cannot be tailored.

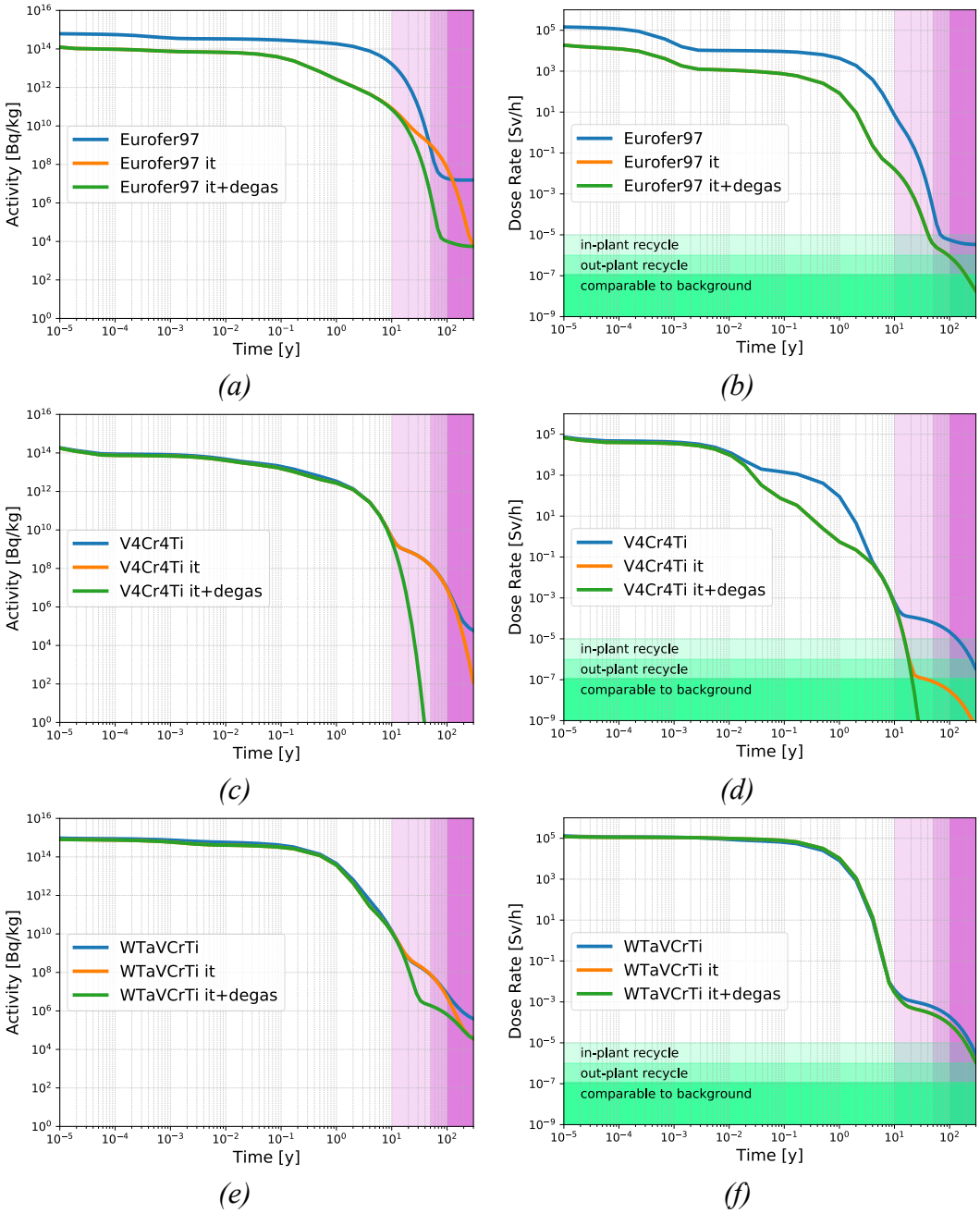

Figure 17: Specific activity and contact dose rate of 97 (a) and (b). Specific activity and contact dose rate of V-4Cr-4Ti (c) and (d). Specific activity and contact dose rate of

WTaVCrTi (e) and (f). Confronting classic and optimized alloys. Isotopic tailoring (it) and radioactive gas removal (degas) as optimization techniques.

4.3.4 Impurity analysis

A preliminary step of the impurity analysis is given by providing the effects of irradiated elements that are here classified as impurities (Figure 18). Impurities like C, O, Si and As are characterized by negligible SA and CDR with respect alloying elements. However, in most cases impurities heavily affect activation results. For instance, Mo, Al, and Nb show CDR orders of magnitude higher than Fe, V and Cr. Hence, even an extremely low concentration of them is expected to modify the SA and CDR behavior.

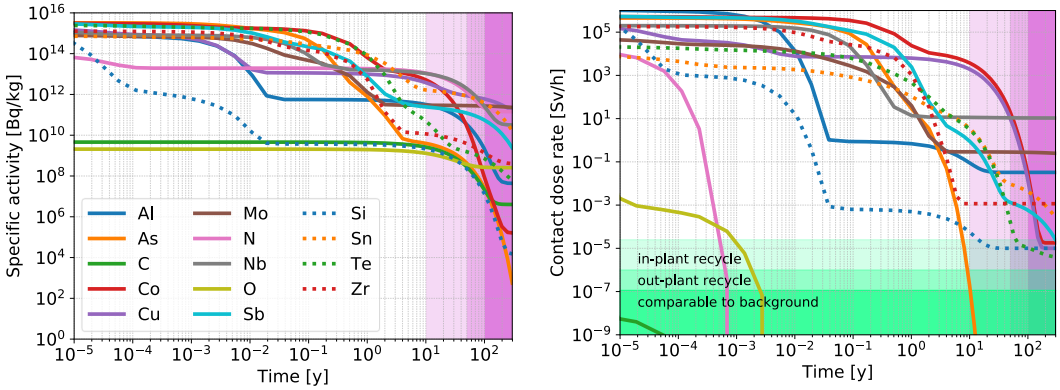

(a) *(b)*

Figure 18: Specific activity (a) and contact dose rate (b) of the elements that are classified as impurities. The legend in (a) is representative for both (a) and (b).

Figure 19 shows the effects of impurities on the three alloys of interest. The comparison is between the alloys with impurities (imp) at the concentration listed in Table 9 and the same alloys as if they were pure (equal to Figure 16). Above 10 years of cooling time impurities cause the specific activity to stand higher than pure alloy. In some cases SA is more than one order of magnitude higher. Regarding CDR results, impurities cause Eurofer97 and V-4Cr-4Ti to miss the recycling limits that the pure cases used to meet within 100 years of cooling time. Nevertheless, V-4Cr-4Ti with impurities seems to be able to meet the in-plant recycling limit slightly after 100 years of cooling time.

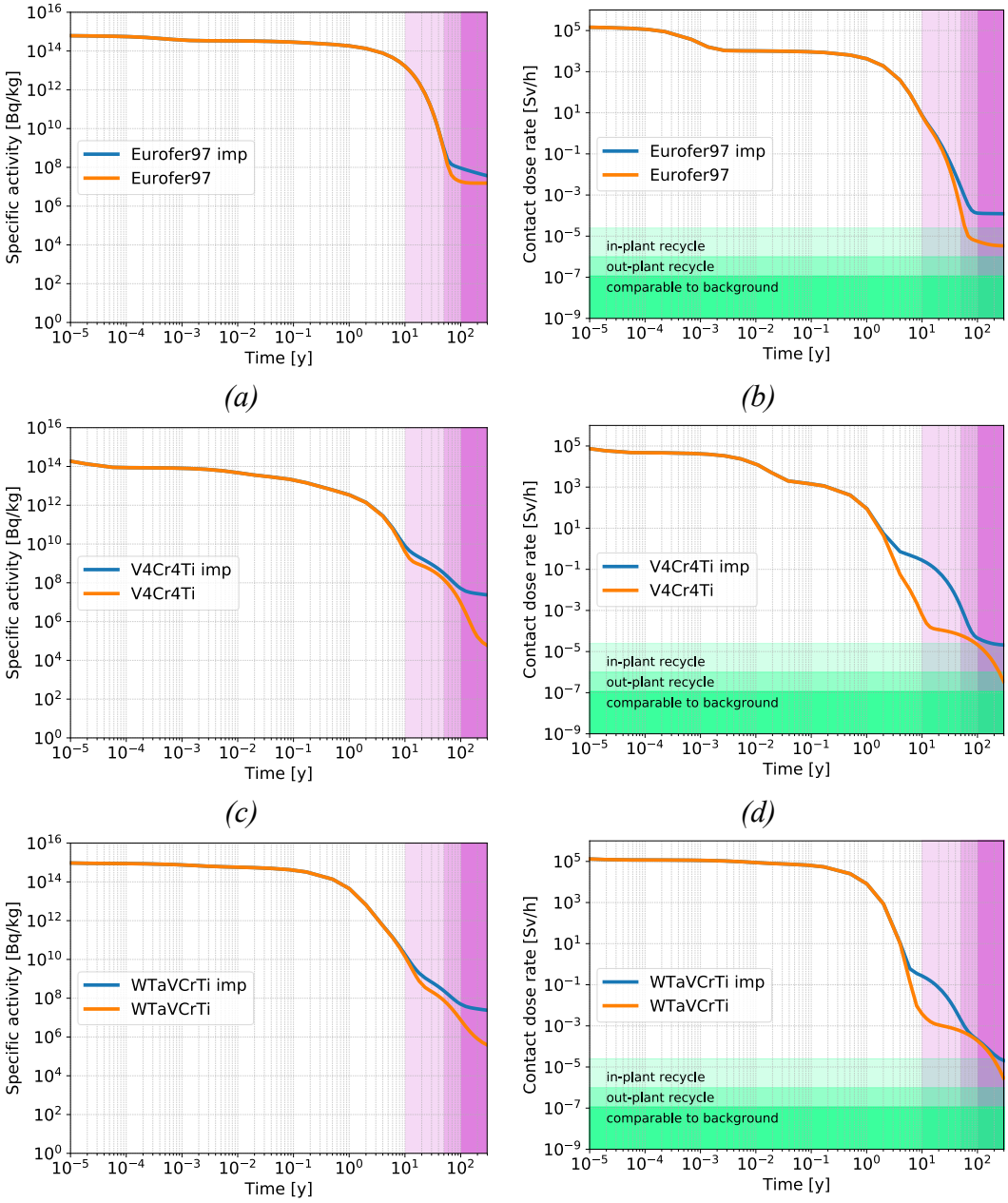

Figure 19: Specific activity and contact dose rate of Eurofer97 (a) and (b). Specific activity and contact dose rate of V-4Cr-4Ti (c) and (d). Specific activity and contact dose rate of WTaVCrTi (e) and (f). Confronting alloys with impurities (imp) and pure alloys.

4.3.5 Irradiation damage

FISPACT-II can compute some 0-D results on the main radiation damage figures of merit. Of main interest for this thesis are the gas generation rate and the displacement per atom (dpa) figures. Transmutation of gas has been already

mentioned in Chapter 3. The dpa figure is a measure of the cumulative microstructural damage caused by irradiation in solid microstructures and it will be deeply discussed in Chapter 5. Figure 20 displays the dpa rate caused by 1 FPY of operations in ARC-like conditions.

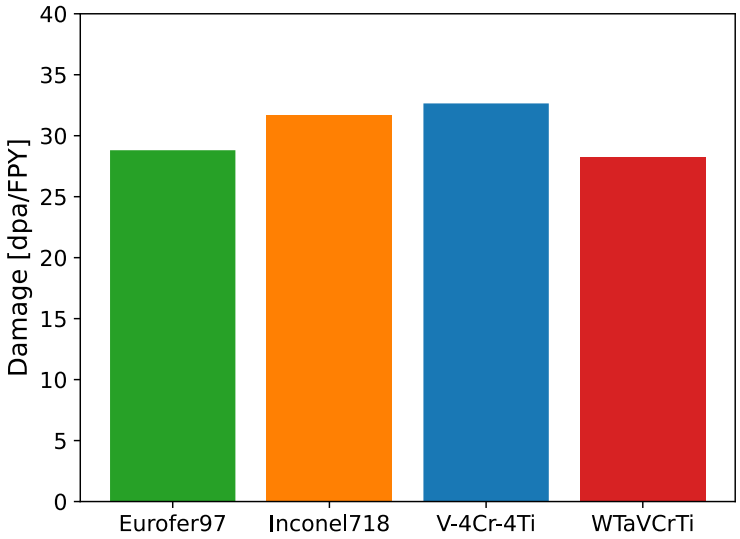

Figure 20: Damage rate (dpa/FPY) for the four alloys studied.

The dpa rate is similar for all the alloys. V-Cr-Ti systems tend to have slightly higher dpa rate because of the lower average mass number of their atoms. For the same reason, a W-Ta rich HEA experiences a lower dpa rate. Figure 21 (a) and (b) depict the gas transmutation rates for the four alloys considered.

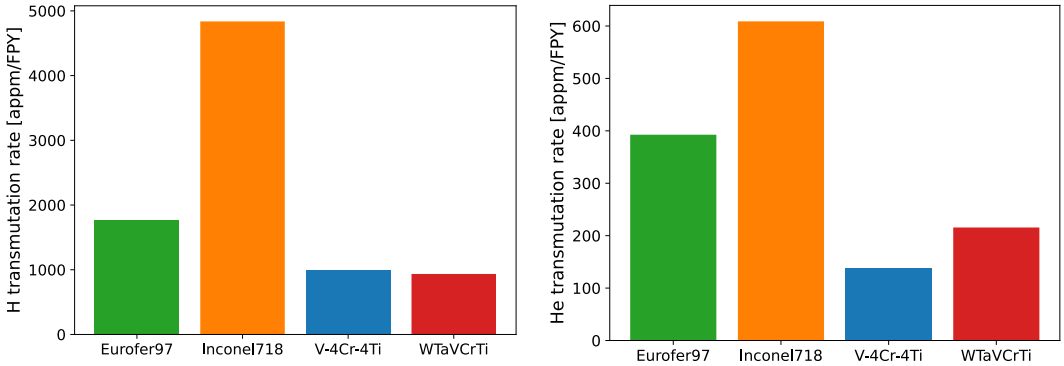

(a) *(b)*

Figure 21: Gas transmutation rate(appm/FPY) for the four alloys studied. Hydrogen transmutation rate (a) and helium transmutation rate (b).

Inconel is the most gas transmutation-intensive alloy, showing a transmutation rate more than doubled with respect other alloys. In some cases, the transmutation rate is more than four times higher. Nickel gas transmutation cross sections for fast neutrons are higher than many other elements, causing Inconel to

transmute much more gas than all the other alloys. On the other hand, V-4Cr-4Ti and WTaVCrTi show a quite low transmutation rate.

4.4 Discussion

Similarly to Chapter 3, this chapter interested the qualitative comparison between materials rather than the precise value of results. Material choice is still on going in the ARC conceptual design. Also, there is lack of information regarding ARC operating conditions. The actual power, the steady state or pulsed plasma operations, the core configuration and geometry and the material management strategy heavily affect activation and damage results. For instance, depending on the component replacement costs and on the waste management costs it could be possible to choose either a radiation damage replacement strategy or an induced activation replacement strategy. In the latter case the strategy would be to replace the component before its induced activation overcomes defined limits. In view of this, the 1 FPY modeling choice seems to be particularly useful as it provides a neutron fluence on the order of 1e+22 $\frac{n}{cm^2}$ on a target on the order of 1e+23 particles, suggesting that on the order of units of years of irradiation the induced activity results would roughly scale linearly with the fluence. The rest of the modeling choices (i.e. fluxes and spectra) are considered a good tradeoff between ARC case study and a generic compact tokamak radiation environment.

Regarding the alloys chosen and in view of advanced alloys (MPEAs), it is clear that material research should put some efforts in substituting nickel with lower activation alloying elements. On the other hand W, Ti and Fe seem to be sufficiently low activation to be kept in consideration. V and Cr are most likely the lowest-activation elements among the transition metals. Ta, on the other hand, should be avoided or minimized. Hence, if the aim is the design of low activation advanced materials, scientists should start from V, Cr, W, Ti and Fe. It has been found that transmutation mechanisms in fusion reactors can be different from fission reactors. More specifically, most transition metals see their neutron multiplication and gas transmutation cross sections dramatically rise above 8-10 MeV. Such rise in the mentioned cross sections causes fusion materials to experience different transmutation mechanisms that are not dominant in fission materials. One main mechanism is the gas transmutation, which is detrimental for the structural properties of materials. On the other hand, there are some elements that transmute by being teared down even to 2 or 3 smaller atomic numbers. It is the case of Ti, for instance. Lighter Ti isotopes tend to be teared down to Ar-42, which has a half-life of 32 years. Ar-42 daughter is the highly radioactive K-42 that takes over the SA and CDR of Ti-based alloys.

Despite three out of the four alloys considered demonstrated to be almost low activation, in most cases the optimization techniques here proposed and modeled proven to be effective. Isotopic tailoring demonstrated to dramatically preventing a high share of radioactivity to be generated. Such technique should be pursued

for the potentiality it has. Radioactive gas removal, on the other hand, has the capability of taking apart a portion of induced radioactivity. In some cases the gas removal is enough for letting the alloy to reach extremely low-radioactivity. Still, the gas removed should be managed somehow. Isotopic tailoring and radioactive gas removal techniques have never been applied but could be technically viable. Isotopic tailoring is based on the same concept of isotopic enrichment. Gas removal could be accomplished through high-temperature enhanced desorption and in this instance the material decay heat could play a role without straining additional energy. As mentioned, at this stage of the analysis ideal conditions have been assumed. More specifically a perfect tailoring of elements (i.e. 100% of a single isotope of choice) and a perfect gas removal have been assumed. It is likely that the effectiveness in reducing the activation would in reality be lower. It and degas techniques are not expected to be viable at least for the first versions of ARC-like reactors as they are quite pioneering and never been applied before on large and standardized components. It is also clear that such techniques require to be cost-effective, especially with respect a classic fission-like waste management. More specifically, the cost reduction given by the reduced radioactivity must compensate the application of such techniques. Since it and degas are not supposed to be soon applied, a more realistic case study has been performed excluding optimization techniques and implementing impurities. Induced activation figures of merit tend to scale linearly with impurity concentration. Hence, a sensitivity analysis has not been considered necessary. In the long term the impurity effect is not negligible. Putting more efforts in the production of highly pure materials for reactor cores would likely pay-off in the waste management phase.

The proposal of recycling strategies should be integrated with inhalation and ingestion doses at least. This is because during component machining, handle, deployment and in case of accidental conditions radioactive dust and microscopic particles are likely to get generated and transported. Nevertheless, recycling within the plant, in rarely frequented areas (e.g. reactor building), could be a practicable and sustainable way to deal with low-activated materials.

Concerning damage, results of Figure 21 are directly comparable to Chapter 3 results. Qualitatively they are very similar, identifying Inconel as the most gas transmutation-intensive alloy. Results are however quite different from chapter 3 results, this is mainly due to the fact that in the present analysis the neutron fluxes have been increased and aligned to 1e+15 $\frac{n}{cm^2 \cdot s}$. To perform a proper comparison, damage results of this chapter should be reduced with multiplication factors that range between 0.7 and 0.8 depending on the alloy considered. Applying the proper reduction factor, results of Chapters 3 and 4 become very similar. Inconel-718 seems to be particularly sensitive to gas transmutation, hence it might be particularly prone to swelling mechanisms. Fe-based alloys seem to have similar

but reduced issues. V-Cr-Ti and W, Ta based alloys show the lowest gas transmutation rates.

4.5 Conclusions

This chapter modeled and simulated the effects of neutron irradiation on the considered alloys and particular focus has been given to the radiation induced activation. Such aspect is a key aspect for assessing the sustainability of such nuclear technology. The modeling phase has been taken enough generic to provide results useful for a broad range of fusion concepts and technologies. Still, the irradiation environment matches ARC conditions providing good guidelines on what to expect from the machine core materials. From the neutron induced activation analysis it is clear that Ni-based alloys should be avoided as much as possible, considering the high concentration of long-lived nuclides they transmute. Considering alloys without impurities, Eurofer97 and V-4Cr-4Ti are the most effective in terms of low activation. WTaVCrTi HEA reaches SA and CDR values that can be 3-4 orders of magnitude lower than Inconel. It is virtually possible to further reduce the HEA activation by reducing Ta and Ti concentrations. Optimization techniques such as isotopic tailoring and radioactive gas removal have the capability of further reducing the activation figures of merit by orders of magnitude. It is therefore suggested to keep researching technologies able to implement them. Since is it not expected to get a perfect effectiveness of such techniques they should be mixed ad applied together to reduce the material radioactivity. On the other hand, impurities can overshadow the effect of optimization techniques. Hence, research on low activation materials should keep putting efforts in the formation of extremely pure materials as well as in the mentioned optimization techniques. Particular focus should be given to the removal of Al, Nb, Mo and Sn impurities. In real conditions (i.e. with impurities and without optimization) none of the alloys reach the recycling limits within 100 years of cooling time. Though, V-4Cr-4Ti reaches the first limit soon after (110 years of cooling time). The HEA would show similar results in the case of reduced Ta and Ti concentrations.

Considering the limits and the waste management strategy here proposed, future studies should focus on and implement inhalation and ingestion dose evaluations. In the meanwhile, future works should also perform assessments for the application of more classic fission-like radioactive waste management and activity limits (i.e. shallow land burial and low- and medium- level waste), for safety and licensing purposes.

Damage FOMs confirm that swelling is most likely the mechanism that most harms irradiated materials in fusion reactors. Damage rates identify V-Cr-Ti and the HEA as the best performing alloys in fusion reactor radiation environments. Alongside damage and low activation properties, tritium breeding and thermal

properties of analysed in previous chapters appear to indicate V-Cr-Ti systems as the best fitting materials for a fusion reactor core structures.

Chapter 5

Primary radiation damage

1.1 Introduction

This chapter focuses mainly on radiation damage in structural materials. Alongside thermal and structural properties discussed in Chapter 2, radiation resistance of materials is one of the key aspects determine the actual feasibility of a prototype reactor. Radiation damage is one of the most concerning aspects in a fusion reactor and it is surely one of the technical issues with the most uncertain outcomes. In fact, it is extremely hard to experimentally reproduce neutron flux and spectra analogous fusion reactor ones. Furthermore, it is unlikely that many results will be shortly available as tritium is extremely rare and laboratory scale DT facilities [22] will not achieve high level of neutron fluence on surrounding materials. Hence, it is likely that most experimental results will be made available by unique experimental machines [1] or directly by full scale pilot power plants [27]. With these premises, computational methods for modeling irradiation damage become extremely important. However, because of the extreme complexity of radiation damage mechanisms and uncertainty regarding material response to fusion neutrons a predictive approach may not be pursuable. It is therefore preferable to adopt a damage minimization approach. In this work elementary mechanisms of irradiation damage are modeled in order to provide an accurate insight and physical understandings. Once the mechanisms are known optimization techniques are applied to materials to provide basic rules for maximizing material radiation resistance and minimizing the damage. More specifically, recent studies suggest highly mixed systems such as MPEAs might have enhanced radiation resistance due to the high configurational entropy and system Potential Energy Landscape (PEL) characteristics (e.g. Energy of mixing) [132], [133]. This part of the work aims to verify and expand these theories on

reactor-relevant mixed systems (Ni-Fe, V-Cr, W-Ta) in order to pave the way for ARC-suitable advanced materials. Which is why this chapter, despite providing useful data for classic alloys, becomes much more focused on advanced materials and MPEAs aiming also to push forward research in this field.

1.1.1 Damage mechanisms

From a macroscopic viewpoint, radiation damage in structural materials causes several significant changes in the mechanical and thermal properties of the materials themselves, dramatically undermining their integrity and functionality. With respect to metallic materials, usually thermal conductivity tends to decrease while yield strength raises in spite of an increased hardening and material embrittlement [28], [29], [134], [135]. Embrittlement is probably the most threatening effect as it switches components failure mode from gradual and predictable (ductile failure) to an abrupt failure mode, which is also harder to predict in terms of operating lifetime. High operating temperatures and post irradiation annealing could help mitigating the embrittlement effects [136].

The root causes for these macroscopic property deviations must been searched at nano and microscale level. When neutrons interact with atoms of a structural material three main phenomena may be observed: scattering, transmutation and fission. Fission is extremely rare and requires neutron interaction with fissile elements usually not present in fusion components (U, Pu, etc.). The effects of scattering on structural materials are several point defects (vacancies and clusters) that can merge in defect clusters, and any sort of dislocations. Transmutation is caused either by neutron absorption or expulsion of lighter elements from lattice atoms, mainly other neutrons and gas nucleons (H and He). These elementary effects (point defect production and gas transmutation) can be observed at ps-to-ns timescales and nm-to-μm length scales. At relatively higher scales (also called mesoscales) these effects and defects tend to migrate and interact with each other. Transmuted impurities, especially hydrogen, and even alloying atoms may be segregated near the grain boundaries or give birth to precipitates and other second phases. Vacancies defects can accumulate in clusters and give birth to voids. Such voids are usually unstable and tend to recombine. However, if helium is present nearby, it might stabilize them giving birth to thermodynamically stable helium bubbles and, ultimately, swelling. As mentioned in previous chapters, swelling is expected to be a major threat in fusion reactor and fast reactor materials. Core materials are invested by an extremely high number of neutrons which repeatedly cause this type of phenomena whose effects buildup and evolve quickly. Segregates, precipitates and especially swelling are the main causes of radiation induced embrittlement in structural materials.

Exception made for the recently born HEA WTaVCrTi, the other three alloys, namely Eurofer97, Inconel-718 and V-4Cr-4Ti have been characterized for irradiation in experimental fission reactor and accelerator conditions. As

previously mentioned, all the alloys here considered, although with different sensitivity, are subjected to embrittlement because of the formation of precipitates, grain boundary segregations, second phases, gas transmutation and void swelling [68], [136]–[139]. Literature studies acknowledge that V-Cr-Ti systems seem to have a superior radiation resistance than other alloys. Still, they seem to be particularly sensitive to low-temperature irradiation and hydrogen embrittlement [68], [71], [78], [140]. Regarding HEAs in general, some initial studies on irradiation response on MPEAs suggest that some MPEAs may have a superior radiation resistance with respect classic alloys [141]–[143]. Nevertheless, much more studies need to be carried out in order to identify the best elements and relative concentrations for a radiation resistant HEA.

1.1.2 Primary radiation damage

Understandings of radiation damage mechanisms and metrics is crucial for the characterization of radiation response and resistance in materials. Being microstructural defects production the most shared effect of neutron irradiation within solid materials, historically scientists identified the number of defects produced as measure of the irradiation effect [144]. Ever since, nuclear material research put some efforts in both analytical and computational quantitative modeling of the link between defect production and radiation fluence.

The most known and widely accepted models propose a hard sphere-like simplification of particles and atoms. In this instance, neutrons are seen as spheres that bombard material atoms. Each neutron gives part of its kinetic energy to atoms of the irradiated materials. According to a simple binary collision approximation model, the energy transferred can be computed with Eq. 6:

$$\frac{T_d}{E_0} = \frac{A^2 + 2 \cdot A \cdot cos\theta + 1}{(A+1)^2} \qquad \text{Eq. 6}$$

where E_0 is the incident neutron energy, T_0 is the energy transferred to the target atom, A is the target atomic number and θ is the collision angle. If the energy provided is higher than the energy required to displace the atom from its lattice position (E_d), the receiving atom, also called Primary Knock-on Atom (PKA), is knocked on from its lattice position interacting with the surrounding atoms. If the PKA kinetic energy is sufficient, the PKA knocks-on the other lattice atoms giving birth to a collisional cascade. Most of the cascade recombines within the first picoseconds, however few point defects, like self-interstitial atoms or Frenkel Pairs (FP), are always stably left behind [145]. Figure 22 schematically shows the nanoscale effects of radiation damage [146].

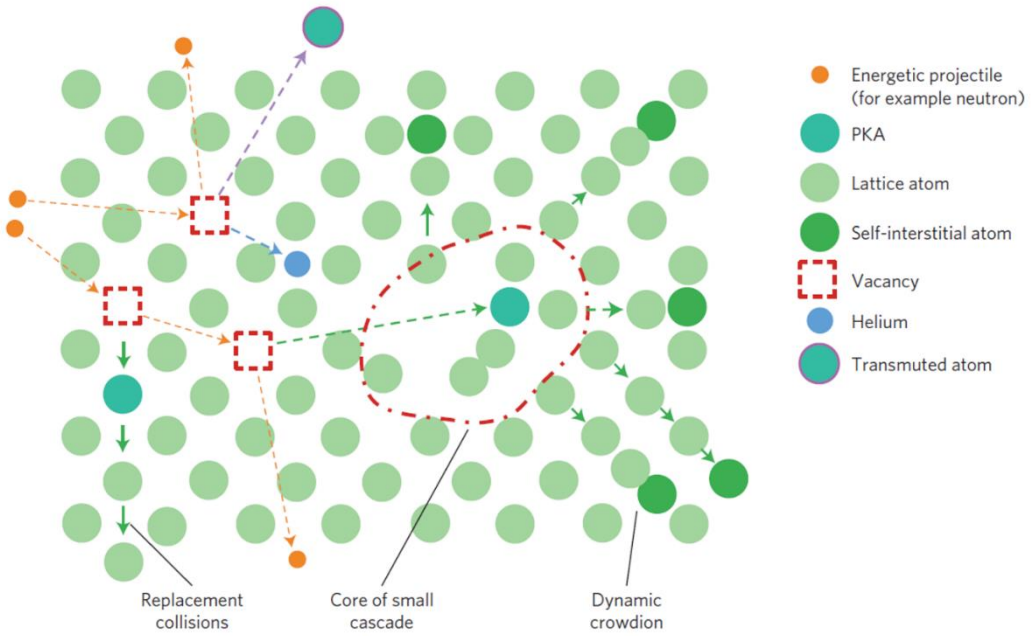

Figure 22: Schematic illustration of radiation damage effects at nanoscale level [146].

One of the first analytical models for the defects produced by a neutron collision with atoms of solid material was proposed by Kinchin and Pease (K-P model) [144], [147]. The Kinchin-Pease model, based in the binary collision approximation, links the number of defects produced (N_d) with the initial PKA energy. Eq. 7 summarizes the Kinchin-Pease formalism [144]:

$$N_d(T_d) = \frac{T_d}{2 \cdot E_d} \qquad \text{Eq. 7}$$

and it has validity for $T_d > E_d$, otherwise $N_d = 0$ for $T_d < E_d$ and 1 for $T_d = E_d$. E_d has been characterized and tabulated for a broad range of pure elements [145]. Normalizing the number of defects predicted by the K-P model on the number of atoms involved it is possible obtain the K-P displacement per atom (dpa_{KP}) figure of merit [144]. Soon after, Norgett, Robinson and Torrens improved the K-P model implementing the effect of cascade recombination [144], [148]. Eq. 8 describes the NRT model for $T_d > E_d$:

$$N_d(T_d) = \frac{0.8 \cdot T_d}{2 \cdot E_d} \qquad \text{Eq. 8}$$

The dpa_{NRT} formalism is by far the most accepted and applied model for the estimation of dose and damage on irradiated materials. More recently, the increase of available computational power allowed for the development of advanced modeling tools, able to simulate a relatively high number of particles and timesteps, such as Molecular Dynamics (MD) techniques [144]. With MD computational modeling, researchers could characterize with a higher precision

the effects of primary radiation damage on a high number of materials. Sensitivity analysis on PKA kinetic energy displayed that the correlation between T_d is less than linear [145]. A damage efficiency (ξ) has been thus defined as $\xi(T_d) = \frac{N_{d,MD}(T_d)}{N_{d,NRT}(T_d)}$, where $N_{d,MD}$ and $N_{d,NRT}$ are the number of defects observed in MD simulations and computed with the NRT formalism, respectively. It has been noticed that for relatively low values of T_d the efficiency can be higher than 1 but it decreases with increasing T_d. For most of the transition metal elements, ξ stabilizes at values of 0.2-0.3 with PKA energies equal or above 5-10 keV. At around 5 keV of PKA kinetic energy, the cascades tend to subdivide in several sub-cascades stabilizing the correlation defects-T_d to a linear fashion, but still with values that are 3-5 times lower than the values computed with the NRT model [144]. Recently, Nordlund et al. [145] proposed a further improvement of the dpa metrics in order to take into account for the mentioned damage efficiency. Nordlund et al. explain the damage efficiency with the prompt effects the recombination right after the cascade peak [145]. The equation proposed is the athermal recombination-corrected dpa (arc-dpa), described in Eq. 9:

$$N_d(T_d) = \frac{0.8 \cdot T_d}{2 \cdot E_d} \cdot \xi(T_d)$$
$$\xi(T_d) = \frac{1 - c_{arcdpa}}{\left(2 \cdot \frac{E_d}{0.8}\right)^{b_{arcdpa}}} \cdot T_d^{b_{arcdpa}} + c_{arcdpa} \qquad \text{Eq. 9}$$

Alongside E_d, c_{arcdpa} and b_{arcdpa} are parameters that characterize the element type and should be estimated through MD simulation.

The primary radiation damage models described so far are widely accepted and describe relatively well collisional effects of radiation. They are still open to improve their precision and physical explanations of damaging processes. For instance, while this link between irradiation and damage to materials can scale with their displacement threshold energies (E_d) for displacing atoms from their lattice position, several transition metals show very similar threshold energies but different values of primary damage [144]. It is therefore possible that, alongside E_d, other material thermodynamic properties play a role in defining primary radiation damage resistance. The arc-dpa model includes c_{arcdpa} and b_{arcdpa} to improve the model precision and include a better description of differences between different target materials. It however requires a high number of MD simulations in order to perform sensitivity analysis on PKA energy and fully evaluate c_{arcdpa} and b_{arcdpa}. That should be done for all the different elements and each type of mixed systems. The advent of MPEAs dramatically increases the complexity of such task. Furthermore, the aforementioned studies, like many, simulate one to very few cascades in the same system, reaching very low levels of dose (order 10^{-3} dpa) [145]. It is nonetheless known that, in absence of other damaging phenomena (e.g. gas production), primary radiation damage saturates and stabilizes at much higher radiation doses (i.e. about 0.1-0.5 dpa) [133]. For

these reasons, researchers are attempting to ease the arc-dpa model keeping included the damage efficiency effect and, on the other hand, efforts are being made to provide information regarding materials response to primary damage at saturation [133], [149]. In this sense, recent studies conducted by Jin et al. [133] proposed, providing also initial hints, that the Potential Energy Landscape (PEL) of a material can play an important role on the radiation response of the material itself, especially at damage saturation. One of the aims of this work is to explore the validity of such hypothesis and raise, if possible, the level of knowledge of the physical rules that dominate such link. Paragraph 1.1.3 provides a detailed description of the mentioned hypothesis and main goals of the present work.

1.1.3 Damage minimization and alloy design

The complexity of radiation damage mechanisms as well as the multi-scale nature of their evolution and macroscopic effects require the development and applications of modeling strategies, material characterization and alloy design. In this respect, this work aims to investigate the roots of the mechanisms behind radiation damage in order to find simple technical and physical rules for their minimization and that apply for a wide range of materials. In this way it is possible to characterize the behavior of the studied alloys and elements (Fe, Ni, V, Cr, Ti and W) and to provide useful information and models for the damage minimization of such alloys and, especially, MPEAs. The roots of radiation damage mechanisms are identified as the effects of primary damage and gas transmutation within the material microstructure. Reducing the transmutation of gas is the first step to inhibit swelling and hydrogen segregation. Previous chapters addressed this issue showing that V, Cr, Ti, W and Ta are preferable to Ni and Fe. But there are many other elements that should be analysed (e.g. Co, Mo, Mn etc.). On the primary damage side, the production of defects and defect clustering are the most important effects. Such phenomena require to be minimized in order to raise the material radiation resistance. In this sense, Jin et al. [133] suggested that there is a link between the thermodynamic properties of a solid system and its radiation resistance, introducing the concept of Potential Energy Landscape (PEL) to the radiation damage modeling research. The PEL is given by the interaction between particles also called interatomic potential. Figure 23 graphically depicts the potential energy landscape of some particles ordered similarly to a transition metal lattice at equilibrium. The energy wells are the regions at lower potential energy, and it is where atoms stand at equilibrium. The saddle points give the preferential direction for atoms and defects migration (Figure 23 (b)). The magnitude of the saddle point is the Migration Energy Barrier (MEB) that the atom/defect has to overcome to complete one migration step. Mixed systems like MPEAs are qualitatively characterized by an increased complexity in their PELs, though a quantitative measure of PEL heterogeneity does not always follow directly from increased mixing.

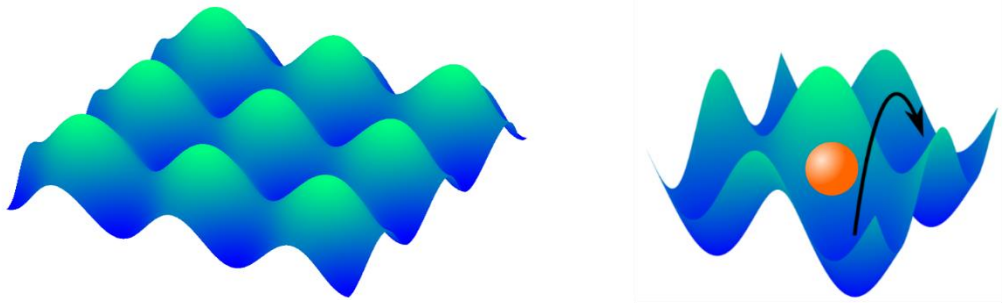

(a) *(b)*

Figure 23: Qualitative graphical representation of a Potential Energy Landscape (PEL) surface (a). Blue regions are the wells at lower potential energy, where atoms tend to stand at equilibrium. Saddle points are atoms/defects preferential migration directions, as shown in (b), as they represent the minimum Migration Energy Barrier (MEB).

Jin et al. [133] focused on mixed systems and proposed that the energy of mixing and the MEBs play an important role in the radiation resistance of the solid solutions. Their studies were performed with Molecular Dynamics (MD) on NiFe mixed systems and simulated primary damage up to saturation (roughly 0.5 dpa) [133]. Results showed that NiFe systems with low mixing energy, high defect Migration Energy Barriers (MEBs) and high heterogeneity in the MEB values had a relatively high resistance to primary radiation damage. The information on the mixing energy and the MEB heterogeneity are of main interest for MPEAs, while the results on the MEB value itself is relevant either for classic alloys or pure metals and for MPEAs. Regarding MPEAs, there is a competing hypothesis stating that the alloy primary radiation damage resistance is directly linked to the high configurational entropy provided by this type of materials [132]. This work aims to expand the study performed by Jin et al. with two main goals. The first goal is to assess the radiation resistance of advanced reactors and ARC-relevant elements for core structures widely discussed in this thesis (i.e. V, Cr, Ti, Ta and W). For this reason, also relevant mixed systems are included (i.e. VCr and WTa), according to the MD current possibilities. The second goal is to shed some light on the likely link between the PEL and the primary radiation damage at saturation for transition metals and mixed systems, as it might be the searched rule for damage minimization that applies to a wide range of materials. To do so, this work focuses on the role of the system potential energy (U) and the defect migration energy barrier (MEB), as well as their heterogeneity, in imparting resistance to primary radiation damage via reduced FP survival following subsequent radiation damage cascades. Uncovering the links between PEL features and primary radiation damage would accelerate the identification and characterization of radiation resistant materials. Lastly, it would provide effective guidelines for an efficient and more targeted design of radiation resistant MPEAs, helping a quicker navigation of the nearly infinite compositional complexity where islands of stability may be waiting for discovery.

1.2 Methodology

Molecular Dynamics is a widely applied method when it comes to model primary radiation damage. MD is also particularly suitable for the characterization of an atomistic system thermodynamic properties (e.g. PEL characterization. Hence, in order to carry out the study, molecular dynamics modeling and simulation method has been heavily applied in this chapter. For this reason, a relatively deep explanation of MD algorithm and mathematical framework is here proposed.

1.2.1 Molecular Dynamics method

Molecular Dynamics (MD) is a deterministic numerical method used to simulate the motion of a very large number of atoms or molecules. MD determines the properties the system following the laws of classic mechanics [150], [151]. More specifically, MD method solves Newton's equations of motion (F=m·a) in many body (N-body) systems, relying on precompiled interatomic potential libraries. Interatomic potentials determine how particles interact with each other, modeling a force field the particles themselves are immersed in. In this way, MD can avoid the application of complex and computationally expensive quantum mechanics. Considering the large number of particles that need to be simulated, MD usually require the application of dedicated software able to integrate and solve Newton's equations for each of the particles in the system for every timestep. The generic algorithm that MD software implement is rather simple, and it is here described with the flow chart of Figure 24.

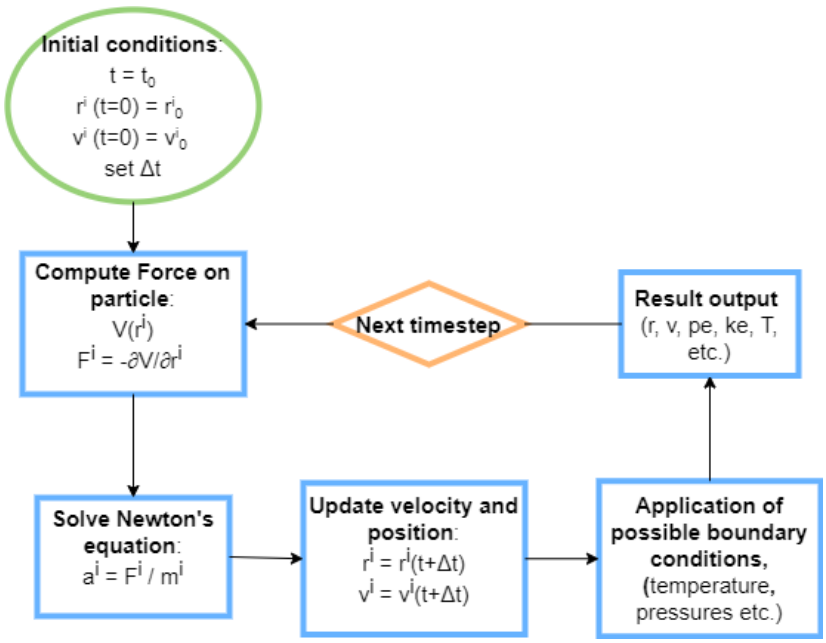

Figure 24: Generic algorithm for molecular dynamics resolution, pe and ke are the potential energy and the kinetic energy, respectively.

Because of the very high number of particles involved, MD models complex systems relying on the statistical mechanics framework [151]. Since it is not the aim of this work, statistical mechanics will not be discussed here, if not in few words and only in concern of the study proposed. Physical properties such as temperature (T), internal energy (U), velocity (v) etc. are not the same for each particle but they are rather attributed to particles according to a given statistical distribution. In this instance, Maxwell-Boltzmann, Fermi-Dirac and Bose-Einstein distributions are the most relevant by far. Maxwell-Boltzmann distribution, which is the simplest and it consider particles as distinguishable, is particularly suitable for the description of crystalline systems like transition metal solids [152]. Through statistics it is possible to treat a high number of particles as ensembles and to compute and model the ensemble thermodynamic properties. There are different types of statistical ensembles depending on the thermodynamic constraints applied to the group of particles involved [153]:

- microcanonical ensemble, also called NVE ensemble, is a statistical ensemble that represents a completely isolated system. In a microcanonical ensemble the system cannot exchange neither mass nor energy with the surroundings. NVE stands indeed for fixed and constant number of particles (N), system volume (V) and total energy (E).
- In the canonical ensemble the mass exchange is not allowed and the system is in thermodynamic equilibrium with the surroundings. Namely, the system is allowed to exchange energy with the environment. The canonical ensemble is also known as the NVT ensemble, where the system number of particles (N), the system volume (V) and the average temperature (T) are constant. In deterministic simulations, such as molecular dynamics techniques, the algorithm that models the canonical ensemble has been developed initially by Nosé and perfectioned by Hoover [154], [155]. Such algorithm is also called the Nosé-Hoover thermostat and it is widely used for modeling isothermal systems.
- The third principal type of statistical ensemble is the grand canonical ensemble. Such ensemble represents an open system able to exchange both matter and energy with the surroundings. The grand canonical ensemble is also known as the TμV ensemble and it is characterized by a constant temperature (T), chemical potential (μ) and volume (V).
- Alongside the three main statistical ensembles, other ensembles are widely applied in the modeling field. It is the case of the Gibbs ensemble, that models and isothermal-isobaric system (NPT) and the isoenthalpic-isobaric system (NHT).

Each of the mentioned ensembles is suitable for modeling different conditions and phenomena taking place in a simulation. For instance, the Gibbs ensemble can be used to relax the volume of a metal system in which the lattice constant is unknown or variable all along the box. Ensembles that define the overall average temperature (e.g. the Nosé-Hoover thermostat) can be used to model an energy

(thermal) sink in which particles velocity is constantly scaled down to satisfy the ensemble fixed temperature. The methodology section of this work makes explicit which type of statistical ensemble is applied to each model described and used.

Interatomic potentials

The algorithm applied in the MD methods is quite simple. Still, there are some aspects that complicate the computation. Each atom experiences a force that is dictated by all the surrounding atoms. As mentioned in Figure 24, MD method computes the force differentiating atoms potential energy (U). Potential energy is mainly a function of particles type and their spatial distribution and it can be seen as a 3D energy landscape that surrounds each atom. Particles tend to find their equilibrium position on the U local minima. Most known interatomic potential is the Lennard-Jones (LJ) potential. Eq. 10 describes the LJ potential in a two atoms system [156]:

$$U_{LJ} = 4\varepsilon \cdot \left[\left(\frac{\sigma}{r}\right)^{12} - \left(\frac{\sigma}{r}\right)^{6}\right] \qquad \text{Eq. 10}$$

where U is the potential energy of each of the atoms, ε is the depth of the potential well, r is the particle relative distance and σ is the atom radius as in a hard sphere model. The behavior of the LJ potential as a function of particles distance (r) is shown in Figure 25.

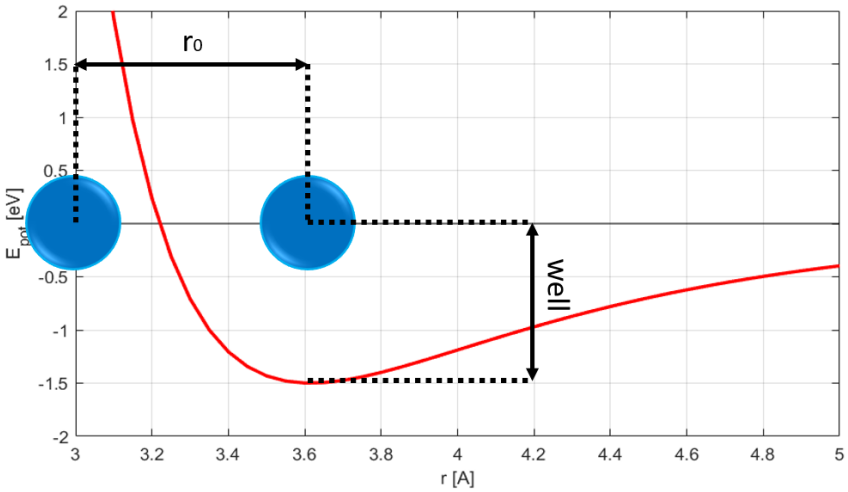

Figure 25: Qualitative 2-D behavior of a Lennard-Jones-like interatomic potential as a function of particles distance (r). Blue circles represent the particles.

When the potential is positive the two atoms experience a reciprocal repulsive force. At very low r, the repulsive force shows an asymptotical behavior to infinite because of the Coulomb interaction. At relatively higher distances the van der Waals attractive forces counterbalance the Coulombic ones leading to a potential minimum, which defines the equilibrium distance. Seeing as how in MD models there are many interacting particles, the computation of the potential must take into account, for each particle, the reciprocal effect ideally with all the

surrounding particles. In reality, a cutoff distance beyond which the Van der Waals attraction is considered negligible is set.

LJ potential is usually implemented in MD codes. Nonetheless, several other methods for the potential description have been developed to satisfy different modeling necessities and to get closer to experimental results. Of main interest for this thesis is the Embedded Atom Method (EAM), typically used for transition metals and relative alloys.

The EAM is a method that computes pairwise interactions for metals and metal alloys. The energy of the i-th atom is given by [156]:

$$U_i = F_{Ti}\left(\sum_{j\neq i}\rho_{Tj}(r_{ij})\right) + \frac{1}{2}\sum_{j\neq i}\Phi_{TiTj}(r_{ij}) \qquad \text{Eq. 11}$$

It shows that the embedding energy F is a function of the electron density ρ of all the atoms surrounding the i-th particle within the cutoff distance chosen. Φ is a pair potential interaction. Subscripts Ti and Tj refers to the types of atoms i and j, respectively. Both ρ and φ depend on the relative distances between the i-th and j-th atoms. In literature there are also several types or corrections of EAM, like the Modified Embedded Atom Method (EAM) and the Finnis-Sinclair formalism (FS) [156], [157]. Of particular interest for this thesis is the possibility of implement the Ziegler-Biersack-Littmark (ZBL) pair style [158]. Such formalism for particle interaction calculations mainly considers the particle electric charges and the particle repulsive effect [158]. The ZBL potential is hence suitable for modeling particle collisions. In the specific case of this thesis, it is useful when it comes to model the atom cascade, where particles have a high kinetic energy and often interact and exchange forces at distances that are shorter than the typical radius of the potential well, that is where the Coulomb repulsive effect rises steeply. Because of the solely repulsive nature of the ZBL pair style, in practical models it is often joined to other potentials (e.g. LJ, EAM etc.). Usually, the ZBL potential is switched on with a smooth function when two or more particles come closer than a given distance [156]. The ZBL formulation for the i-th atom energy is given by [156], [158]:

$$U_i = \frac{1}{4\pi\epsilon_0}\frac{Z_i Z_j e^2}{r_{ij}}\Phi(r_{ij}/a) + S(r_{ij})$$

$$a = \frac{0.46850}{Z_i^{0.23} + Z_j^{0.23}} \qquad \text{Eq. 12}$$

$$\Phi(x) = 0.18175e^{-3.19980x} + 0.50986e^{-0.94229x} + 0.28022e^{-0.40290x} + 0.02817e^{-0.20162x}$$

where ϵ0 is the electrical permittivity of vacuum, Zi and Zj are the nuclear charges of the i-th and j-th atoms and e is the electron charge. S is the switching function that joins the ZBL pair style with the coupled interatomic potential.

Main thermodynamic properties

It is now possible to compute the overall thermodynamic properties of the system. Potential energy (U) of each particle is derived from the input interatomic potential and atoms relative distances and applied in the MD algorithm shown in Figure 25. The system potential energy (U) is given by the sum of the potential energy of each particle. Ideally, in a fully static and homogeneous system at equilibrium, each particle stands in the potential well and the system potential energy is equal the value of the potential well time the number of particles. Kinetic energy (KE) of particles is directly related to their temperature (T) through classical mechanics. Also it is possible to come up with the system kinetic energy (KE) by summing up the particles kinetic energy for each of the three directions [156]:

$$KE = \frac{3}{2} N k_B T = \frac{1}{2} \sum_{i=1}^{N} m_i v_i^2 \qquad \text{Eq. 13}$$

where k_B is the Boltzmann's constant, mi is the i-th particle mass and v_i is the i-th particle velocity component in each of the three directions. System internal energy (E) is the sum of the potential energy and the kinetic energy, namely $E = U + KE$. Thermodynamic pressure is given by a kinetic component and a potential component, as follows [156]:

$$p = p_{KE} + p_U = \frac{1}{3V} \sum_{i}^{N} m_i v_i^2 + \sum_{i}^{N} r_i f_i \qquad \text{Eq. 14}$$

where V is the system volume, ri is the i-th atom position vector and fi is the force vector on i-th atom that can be derived by the force field (namely, the interatomic potential through the Newton's equations). System enthalpy (H) sums up the internal energy and the product of pressure and volume, namely $H = E + pV$ [156].

Other additional thermodynamic properties are the free energies. Usually, they are not directly computable in absolute terms because of the difficulty in the evaluation of the system entropy [156]. However, their differences can be computed, like in the case of the mixing energy. Gibbs free energy is a potential energy defined as the reversible work that can be done by a system in isothermal-isobaric conditions [156]:

$$G = H - TS \qquad \text{Eq. 15}$$

where G is the Gibbs free energy, while H, T and S are enthalpy, temperature and entropy of the system, respectively. Similarly, the maximum work that a system can do in isothermal-isochoric conditions is given by the Helmoltz free energy [156]:

$$F = E - TS \qquad \text{Eq. 16}$$

where F is the Helmoltz free energy, while U, T and S are internal energy, temperature and entropy of the system, respectively. In this case, because of the isochoric conditions, the enthalpy is substituted only by the internal energy term.

1.2.2 Modeling strategy

Molecular dynamics simulations are performed by means of the Large-scale Atomic/Molecular Massively Parallel Simulator (LAMMPS) open-source code, developed at Sandia National Laboratory [159]. The main strategy is to model boxes of single-phase solid solutions of the same size (i.e. same number of particles), characterize and confront their main thermodynamic properties (i.e. U, MEB) and perform radiation damage simulations. As mentioned, the main elements that can either compose classic alloys or multiple principal element alloys studied in this work are Fe, Ni, V, Cr, Ti, W and Ta. Such elements are the main components of the short-term (Eurofer, Ni-based superalloys) medium term (V-Cr-Ti systems) and long term (refractory, low-activation MPEAs and HEAs) fusion-relevant alloys. Jin et al. [133] provided significant results for a binary NiFe system that become relevant for both Fe- and Ni-based alloys. For the purpose Jin et al. took advantage of the NiFeCr EAM interatomic potential provided by Bonny [160]. Considering the interatomic potentials available in literature as well as the attractive properties of V, Cr, W and Ta found in previous chapter, this work focuses therefore on a pair of binary alloys cuts of the WTaVCrTi system – WTa and VCr. VCr at low Cr concentrations becomes relevant for the V-Cr-Ti systems. Models of W, Ta, and the WTa binary system apply the Embedded Atom Method (EAM) with the Finnis-Sinclair (FS) formalism potential provided by Chen [161]. V, Cr, and the VCr system are modeled taking advantage of the EAM-FS potential proposed by Fu [162]. With the aim of enriching the pool of results available, another BCC metal (Niobium – Nb), the fourth element present in Inconel-718 by concentration, has been included in the study, where an EAM potential provided by Fellinger is applied [163].

In order to provide consistent results, the methodology here adopted is similar to that of Jin et al. [133]. This study takes advantage of three different models to perform the analysis. The first model simulates the system in quasi-static conditions to thermodynamically characterize the materials and to build the initial model for collision cascade simulations. The second model takes advantage of the quasi-static system to perform a forced defect migration to evaluate the defect migration energy barriers (MEB) for each material studied, and their heterogeneity quantified by their variance. The first two models characterize relevant properties of the PEL of each single-element and binary alloy system under investigation. The third model performs the irradiation damage simulations. It provides statistics on defect production and survival, to quantify “primary radiation damage resistance” and link it to aspects of the PEL for each material.

The Open VIsualization TOol (OVITO) is applied to perform part of the MD results postprocessing and visualization [164].

The heterogeneous nature of some results and the randomness of several modeling inputs required the implementation of repeated simulations to obtain meaningful statistics. All results represented with statistics are provided with error bars equal to one standard deviation on both sides of the sample average. For a more comprehensive discussion, some relevant results regarding the FCC Ni, Fe, and the Ni-Fe system from Jin et al. [133] are interpolated and included as-is, without statistics. Those statistics can be found in the reference paper [133].

Quasi-static model

In the quasi-static model the system is defined and allowed to evolve to stability while an annealing-like method is applied. This is necessary because, especially for mixed systems, the exact value of lattice constant is unknown and it is necessary to leave atoms position to the PEL wells by themselves. The annealing process is required on mixed systems as LAMMPS generates atoms position with a random fashion and the configuration of first attempt might not be the most stable one (i.e. the lowest potential energy configuration). For FCC metals Jin builds a box of 108,000 particles (30x30x30 lattice constants) [133]. Here a box of 128'000 particles (i.e. 40x40x40 lattice constants) is designed. Periodic boundary conditions are defined in all cube surfaces to simulate an infinite medium. The system temperature is first set to 300 K, and is then left to stabilize for about 100 ps in the isothermal-isobaric (NPT) ensemble, which is applied every 0.1 ps [165]. In the case of binary systems a combined Monte Carlo – Molecular Dynamics (MC+MD) algorithm is applied [166], [167]. This is in fact the method that mimics annealing effects. The MC+MD algorithm swaps two atoms of different type and computes the change in the system potential energy (ΔU). The swap is accepted with probability $P = \exp\left(\frac{\Delta U}{T \cdot k_B}\right)$, where k_B is the Boltzmann constant, or 1, whichever is smaller [133]. In order to achieve significant levels of annealing, the simulation performs 500 swap attempts every 0.05 ps in the 100 ps NPT phase, for a total of 106 swap attempts. In this way, the mixing energy of the model is maximized. Lastly, the conjugate gradient energy minimization algorithm is applied [167], [168]. For the aim of this work, the system potential energy (U) is the most relevant result of this first type of simulations. In order to compare this work results and Jin's study, which have different microstructure and box sizes (128,000 atoms and 108,000 atoms), potential energy is normalized over the system number of particles $\left[\frac{eV}{atom}\right]$.

Migration Energy Barrier (MEB) model

Migration energy barriers are evaluated through the application of the Nudged Elastic Band (NEB) method to the system [169]. The NEB method is specifically designed to evaluate the energy barrier and profile of a transition between two equilibrium states. Conceptually, in the NEB method several replicas of a particle

are built from an equilibrium state to another one (e.g. a defect initial and final state of a single migration). Usually, 2-8 replicas are created. All replicas are interconnected by nudged spring forces while all the other system atoms work just as background energy landscape definition. The NEB computation is done in two steps, each of them can be considered as an energy minimization towards one of the two directions of the PEL saddle point. In the first step energy is minimized in order to place the line of replicas on the minimum energy path. In the second step, the highest energy replica is placed on the top of the saddle point (barrier-climbing [169]) while the other replicas are equally spaced. At the end of the two phases the energy barrier and profile are univocally characterized [156]. This work specifically analyses migration energy barriers of vacancies, as the use case of these MPEAs for fusion first-wall materials [144] is well above 30% of the homologous temperature for each, where vacancies are expected to be mobile. The NEB method is applied to the annealed systems provided by the quasi-static models. An atom in the center region of the box is randomly selected and removed to form the vacancy. The NEB algorithm is applied to all of its nearest neighbors to simulate vacancy migration on all possible pathways, and MEB values are measured. In this case the quickmin algorithm is applied for energy minimization [156]. Pure metals show a constant migration energy barrier as a function of position, while solid solutions may experience very heterogeneous MEB values [133]. Hence, this study applies a Python routine to automate the process until the MEB standard deviation stabilizes, normally requiring about 160 vacancy migrations. The value of a stabilized standard deviation is in fact a measure of the material intrinsic MEB heterogeneity, and thus the roughness of the PEL of the system.

Primary radiation damage model

Primary radiation damage is modeled through the simulation of subsequent collision cascades. Potentials are smoothly joined to the Ziegler-Biersack-Littmark (ZBL) formalism for simulating short range interactions [158]. Hybrid EAM-ZBL interatomic potentials are implemented in order to properly model the collisional cascade, as discussed by Béland [170]. Figure 26 shows a graphic example of EAM, ZBL and hybrid interatomic potential for the case of W-W interaction.

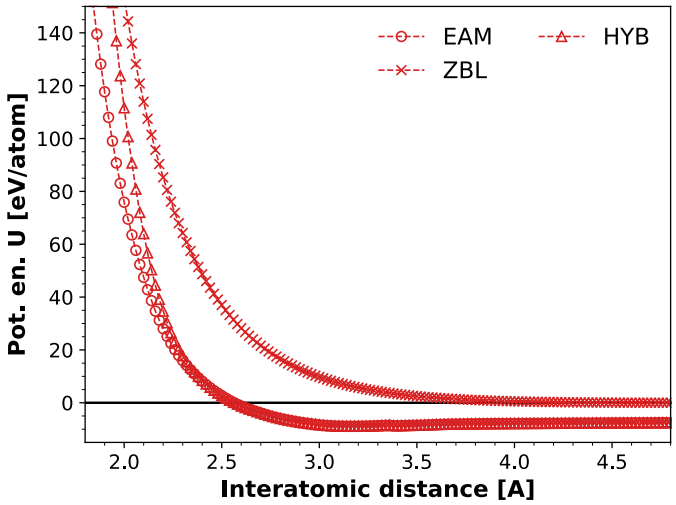

Figure 26: W-W interatomic potentials with different formalisms: embedded atom method (EAM), Ziegler-Biersack-Littmark (ZBL) and hybrid EAM-ZBL (HYB).

The model takes the annealed system from the quasi-static model and applies periodic boundary conditions to the box. The system temperature is set to 300 K, which is not expected to heavily affect damage results, as reported by Nordlund [144]. The box is stabilized for 50 ps in the isobaric-isothermal (NPT) ensemble. Afterwards, the algorithm picks a random particle and shifts the box to position the atom at its center. In this way the collision cascade fully evolves within the box without approaching the periodic boundaries, which has been previously checked [133]. A kinetic energy of 5 keV is given to the chosen particle (PKA) with a random direction. PKA energy of 5 keV may be considered low, seeing as how 14 MeV neutrons can produce PKAs with much higher energies (up to 10 MeV). Nevertheless, 5 keV should be sufficient for reaching the plateau of damage efficiency [145]. In addition, raising PKA energy is extremely computational demanding as the box length would increase linearly with the cascade size and the number of atoms – which directly affects the computational burden – increases with a cubic power fashion. In this model, a PKA speed-dependent adaptive timestep is set in order to raise the cascade simulation precision. The cascade is left to evolve for about 50 ps. Usually 5 keV cascades were observed to evolve and recombine within the first 10 ps. During the cascade evolution a Nosé-Hoover isothermal bath has been set to 300 K and applied to the box boundary atoms in order to dissipate the cascade kinetic energy [154], [155]. The microcanonical ensemble (NVE) condition is then applied to the core of the box. Subsequent collision cascades are performed with a loop algorithm. The Nth cascade takes as input the system of the (N-1)th cascade and in the end stores the system for the (N+1)th cascade. Consistent with Jin et al.'s studies, 1500 subsequent cascade simulations are performed, corresponding to a total of 7.5 MeV deposited and 0.3-0.6 dpa depending on the system under investigation. 1500 cascades ar[171]e considered sufficient to reach primary damage saturation,

where we observe the accumulation of defective atoms to level off. For the sake of completeness and testing our assumptions, an attempt of 2500 cascades with W to verify and confirm the presence of a plateau in defect production has been performed. The postprocessing applies the Wigner-Seitz defect analysis for the FP tally [172], [173]. OVITO cluster analysis with a cutoff radius of 2NN (nearest neighbor) is applied to tally and measure defect clusters [164]. Atomistic temperature distribution, PKA identity, and direction are randomly chosen. It is therefore necessary to perform several simulations and compute statistics of results. Because of the computational cost, only pure metals have been simulated several times (10 simulations per material). Chauvenet's criterion is applied to results because of rare but present OVITO's bias in the post processing of defects in subsequent cascades [171].

1.3 Results

In this section all the relevant results coming from the MD simulations are displayed and explained. Meaningful results will be then deeply discussed in the Section 1.4. Results have been divided in two main subsections. The first subsection shows quasi-static and MEB model results together, as they compose the system PEL characterization. The second subsection lists the primary radiation damage results. A relation between PEL and primary radiation damage resistance has been actually observed. Then, the results section provides also a rearrangement of the most meaningful results, which is useful to highlight the mentioned relation.

1.3.1 Quasi-static and MEB models results

In the quasi-static model, the relaxation of the system left to evolve in the NPT ensemble and energy minimization algorithm allow atoms to position themselves in the PEL wells. This allows LAMMPS to compute the actual lattice constant (ao) of the system, which is useful especially in the case of mixed alloys. Figure 27 shows the lattice constant variation with composition for the two VCr and WTa mixed systems.

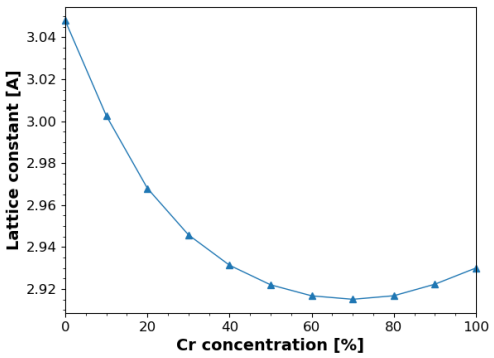

(a)

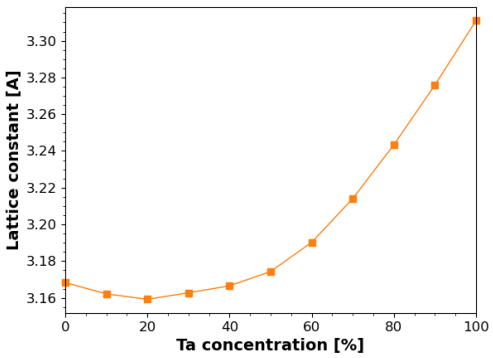

(b)

Figure 27: Computed lattice constants for VCr (a) and WTa (b) as a function of the system concentration.

Alongside volume relaxation, the quasi-static model features the MC+MD forced annealing method to provide the most thermodynamically stable system possible for characterization and radiation damage simulation. This is valid for mixed systems where there are several different configurations dictated by the type of atoms that surround and interact with each other. While potential energy of pure metal systems is constant. In order to show that the systems found with the MC+MD method were the most stable possibly achievable, Figure 28 displays the evolution of the system potential energy (U) and the MC+MD method acceptance rate of swaps evolution as a function of the swap attempts. It confirms that the number of swap attempts are enough to saturate the potential energy decrease.

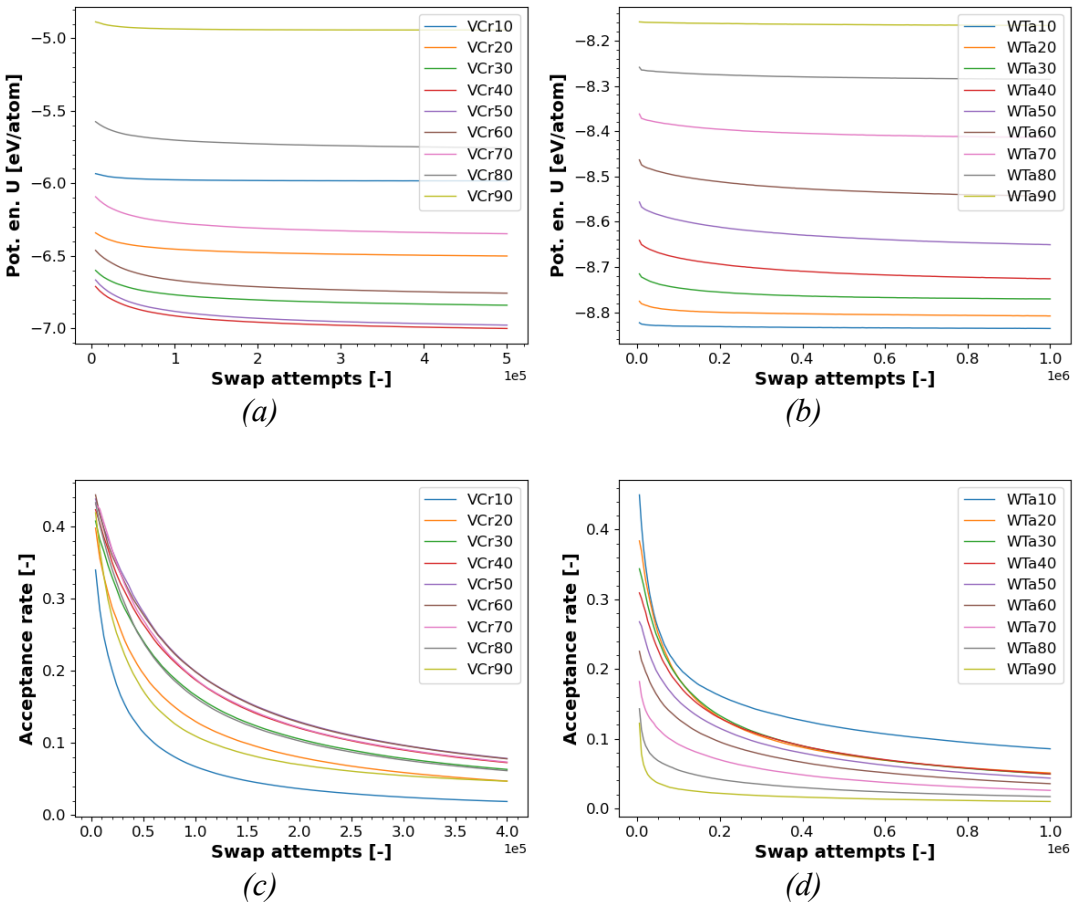

Figure 28: Results of the MC+MD annealing method for the two considered mixed systems. Potential energy (U) as a function of swap attempts for the VCr (a) and WTa (b) mixed systems. Swap acceptance rate for the VCr (c) and WTa (d) mixed systems.

The MEB model as well required the application of several attempts to achieve a stabilized value for the MEB figure. Once again, this is valid for mixed

systems. MEB of defects is usually constant in pure metal systems. The nanoscale-level configurational heterogeneity of mixed systems brings with it heterogeneous MEB values. Figure 29 (a) and (b) show the MEB sample average evolution with the number of MEB sampled. The sample average eventually stabilizes. Figure 29 (c) and (d) display the evolution of the MEB standard deviation. The standard deviation stabilizes as well but, in most cases, it stabilizes at values that are well different from zero. This is because of the MEB heterogeneity. The standard deviation value is indeed a good index for the MEB heterogeneity within the system.

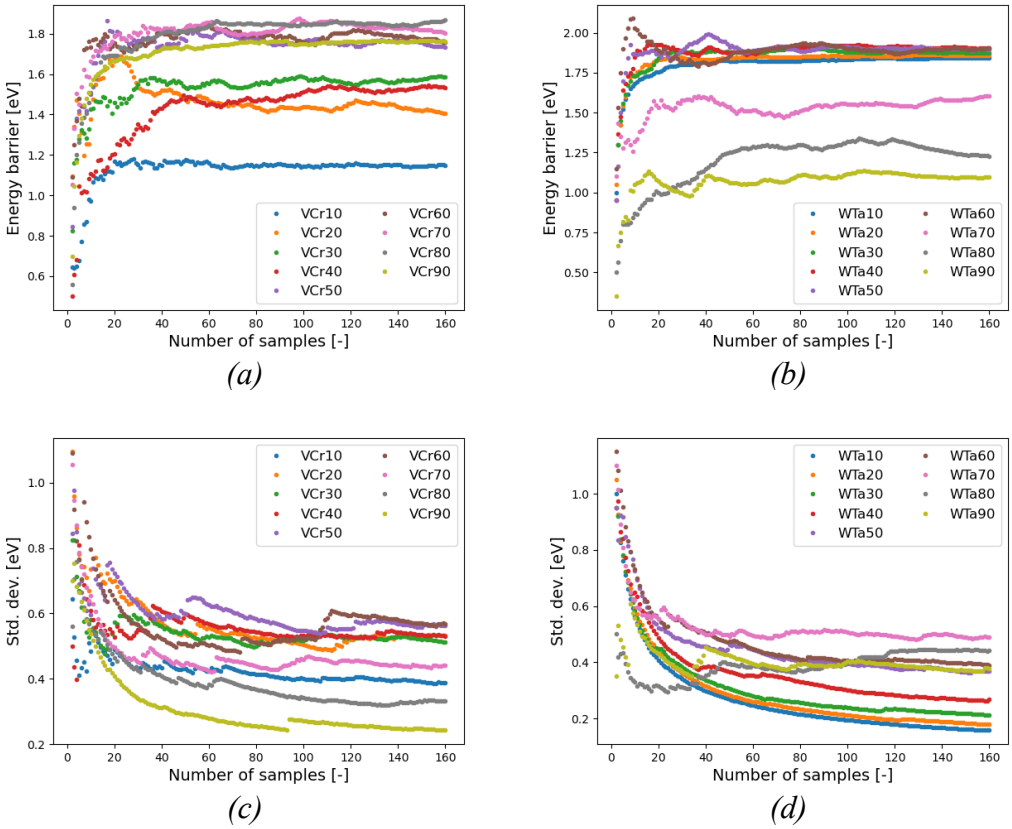

Figure 29: NEB method results as a function of number of MEB samplings. Evolution of the MEB sample average for VCr (a) and WTa (b) mixed systems. Evolution of the standard deviation for the VCr (c) and WTa (d) mixed systems.

Figure 28 and Figure 29 acknowledge that the statistical part of quasi-static and MEB models is sufficient to provide statistically reliable results. Figure 30 shows the main results for the PEL characterization of mixed VCr and WTa systems. Both systems experience the effects of mixing energy. In fact, mixed system potential energy is much lower than the ideal linear potential energy. In addition, it is worth to point out that these two systems are in a different situation with respect Jin et al. NiFe mixed system [133]. More specifically, the NiFe system MEB sample average and standard deviation were at their highest around the

same composition, which was in turn at the lowest system potential energy. So NiFe system has high MEB heterogeneity where MEB value is high and U low. In this study VCr and, especially, WTa are in a different situation: the MEB highest heterogeneity (defined by the MEB standard deviation) is not necessarily found in correspondence of the highest MEB value. Similar difference applies for the system potential energy behavior. WTa with increasing Ta concentration shows a decreasing MEB value and increasing MEB heterogeneity. This enriches the PEL case studies meaningfully.

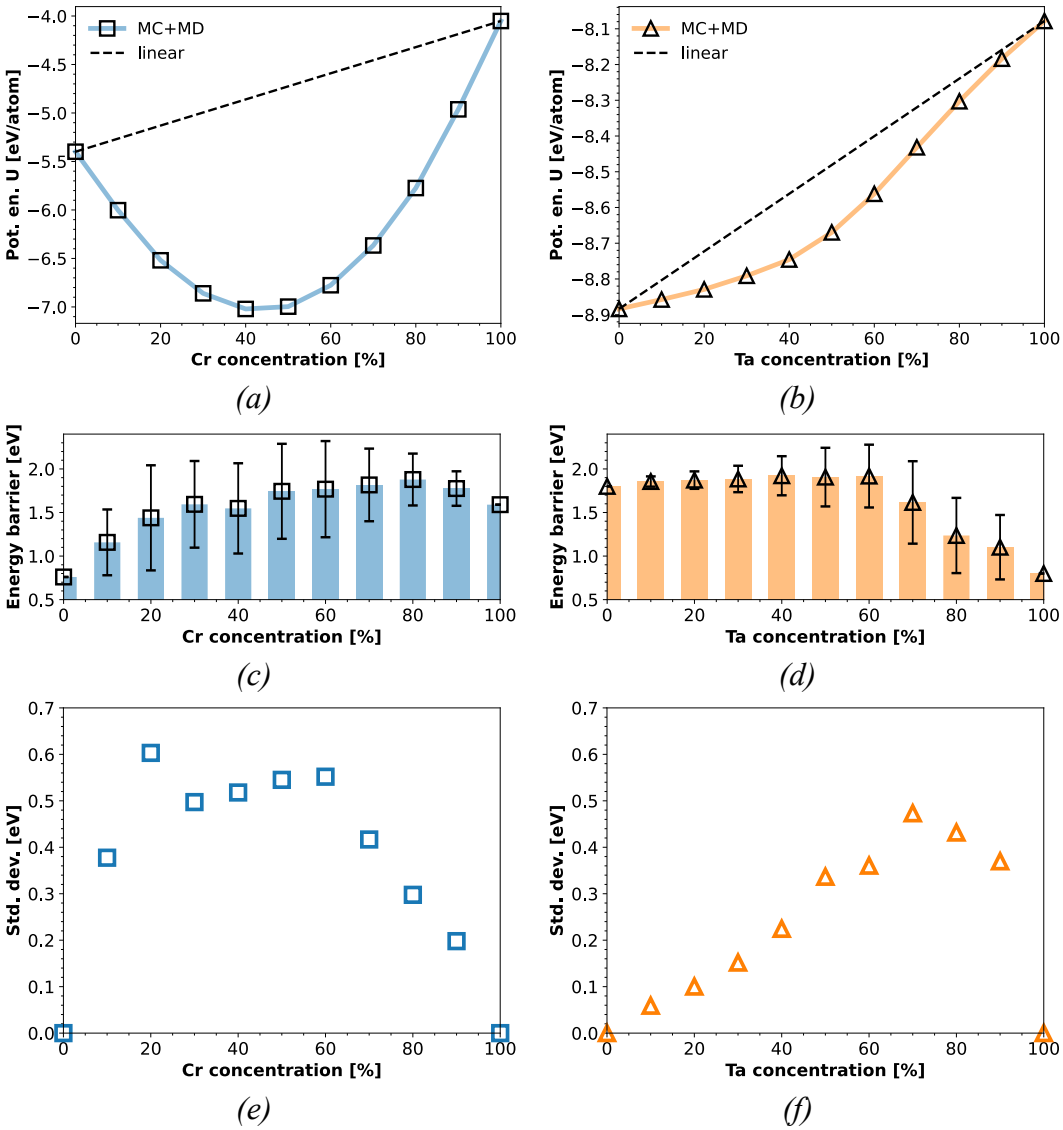

Figure 30: PEL characterization results as functions of mixed systems concentration. Potential energy (U) of VCr (a) and WTa (b) mixed systems. MEB values of VCr (c) and WTa (d) mixed systems. MEB standard deviations of VCr (e) and WTa (f) mixed systems.

Figure 9 provides data for mixed systems and for V, Cr, W and Ta pure systems. As mentioned, an additional pure metal has been included in the study (Nb), such metal showed a potential energy $U_{Nb} = 7.09 \frac{eV}{atom}$ and a MEB equal to 0.65 eV. All the MEB values are in good agreement with experiments and other computational modeling results present in literature, except for Cr which would require additional studies [161], [163], [174]–[176].

1.3.2 Primary radiation damage model results

Once the PEL has been characterized the stable model provided with the MC+MD method is prepared for the primary radiation damage simulation with repeated collisional cascades. As mentioned, if other damaging mechanisms are excluded (e.g. transmutation), primary radiation damage tends to saturate eventually. Figure 31 shows the evolution of potential energy of mixed systems normalized on the initial U at increasing dose (i.e. number of subsequent cascades). Potential energy U reaches a good degree of saturation within the 1'500 cascades here simulated.

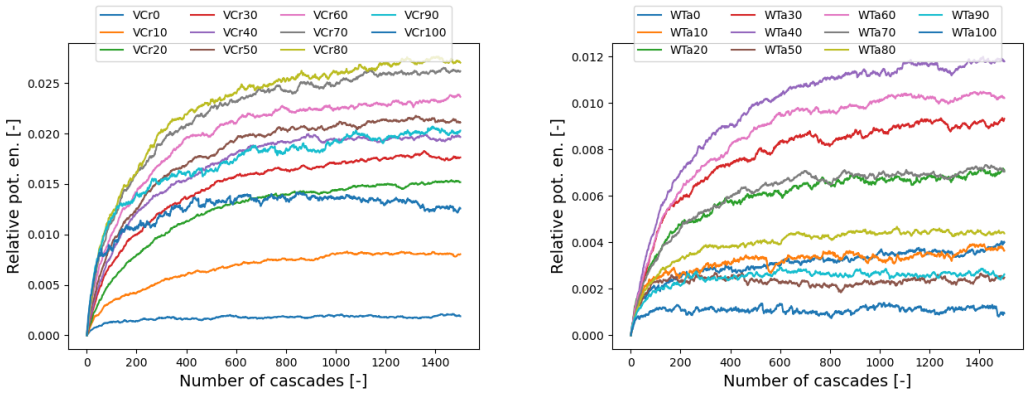

(a) *(b)*

Figure 31: Relative increase of the system potential energy as a function of the number of subsequent cascades (i.e. function of dose) for VCr (a) and WTa (b) mixed systems.

The increase in the potential energy of the system through primary radiation damage simulation is explained with the microstructural defects that each collisional cascade leaves behind. Such defects can either stand alone in the lattice or merge in defect clusters. Figure 32 shows how defects and clusters look like in MD collisional cascade simulations for seven of the modeled materials. It is clear that not only the number of defects is extremely variable but also their distribution within the simulation box.

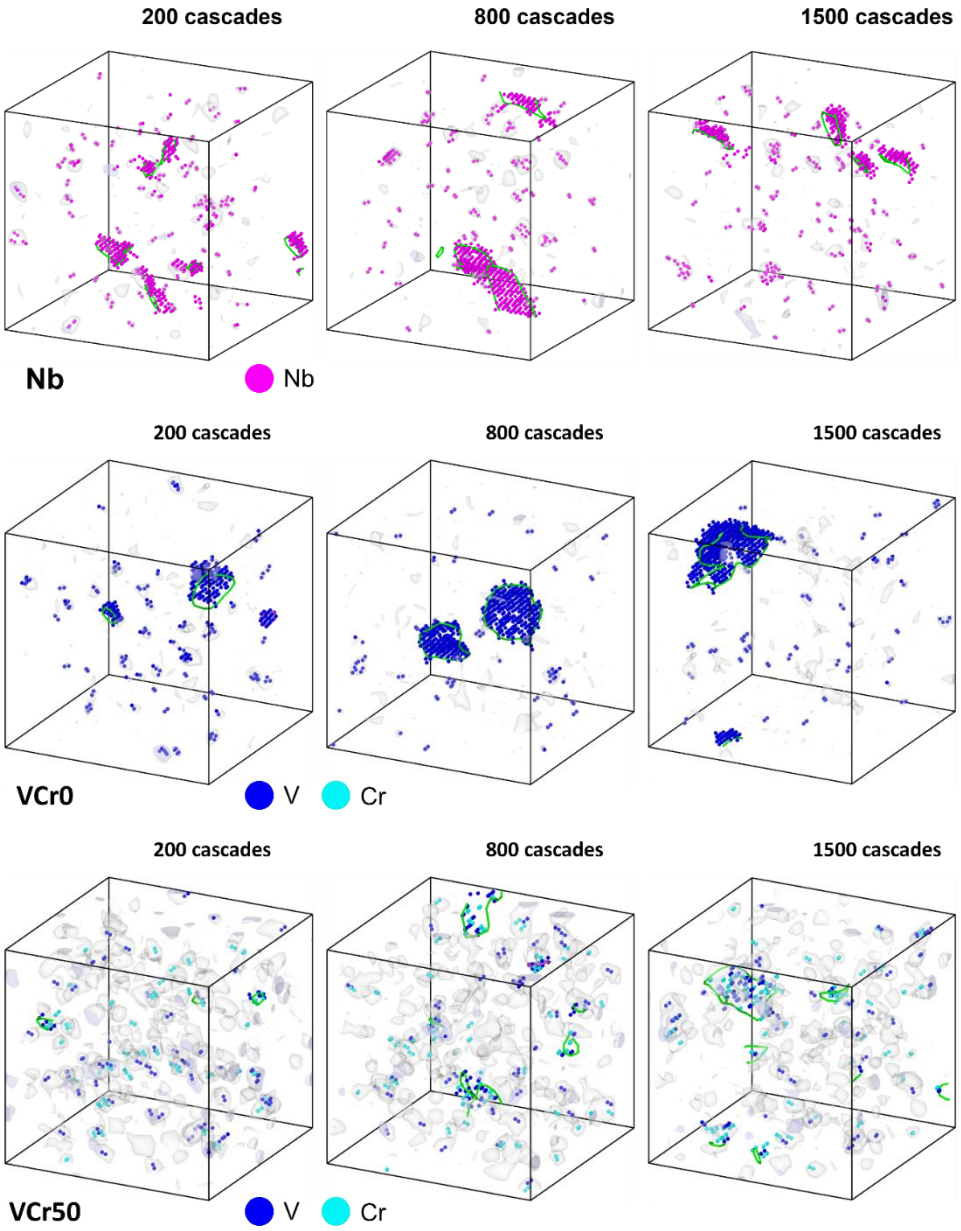
200 cascades
800 cascades
1500 cascades
Nb
Nb
200 cascades
800 cascades
1500 cascades
VCr0
V
Cr
200 cascades
800 cascades
1500 cascades
VCr50
V
Cr

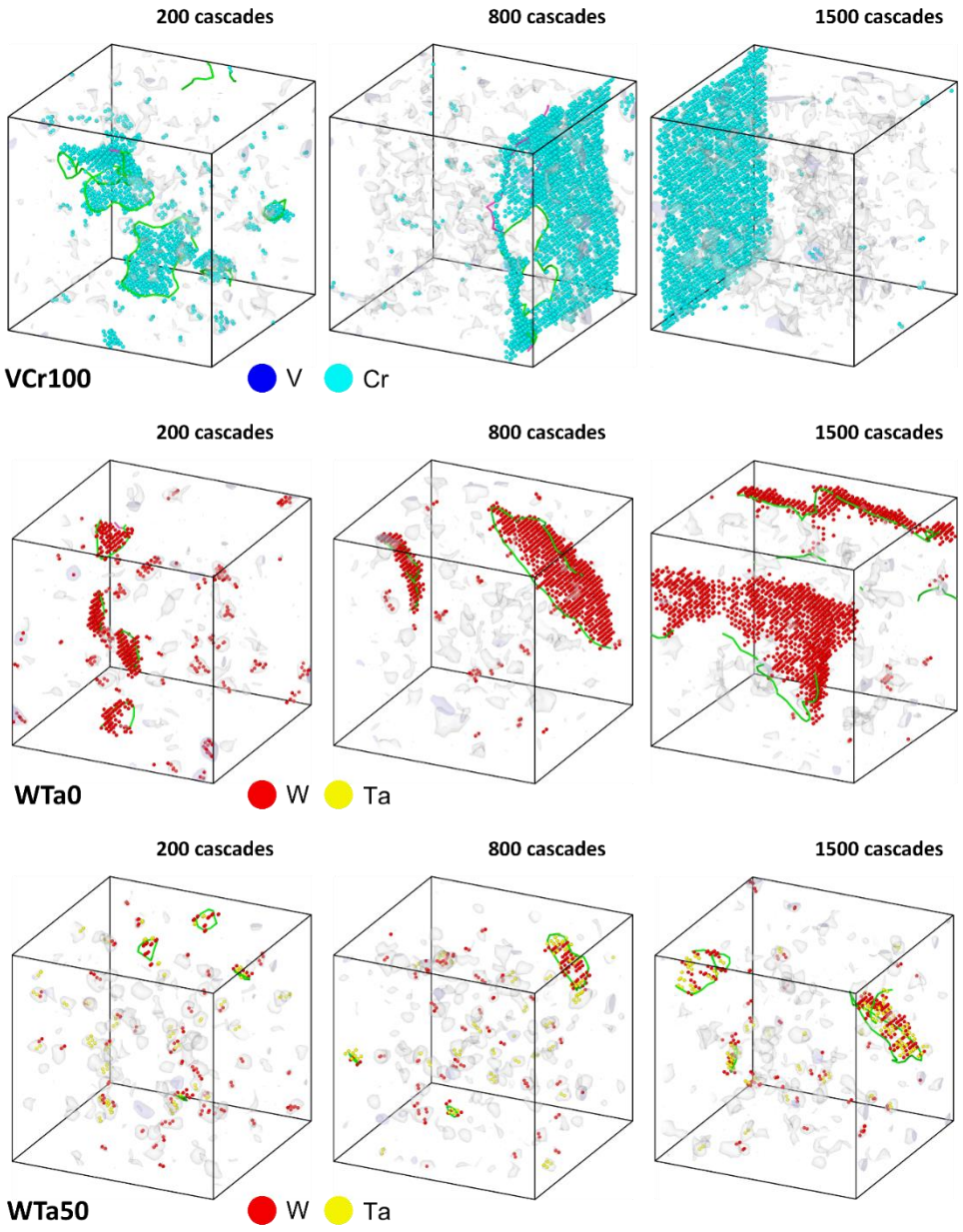
200 cascades
800 cascades
1500 cascades
VCr100
V
Cr
200 cascades
800 cascades
1500 cascades
WTa0
W
Ta
200 cascades
800 cascades
1500 cascades
WTa50
W
Ta

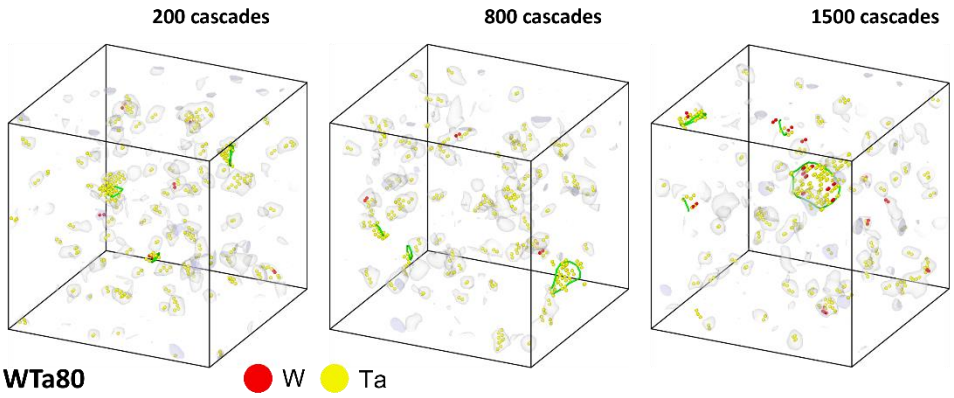

Figure 32: Examples of microstructural defect evolution for 7 systems (Nb, V, VCr50, Cr, W, WTa50 and Ta) recorded at 200, 800 and 1500 cascades.

The complete evolution of point defects formation with statistics in the case of pure metals is depicted in Figure 33 (a), while Figure 33 (b) displays the FPs behavior in the case of some representative binary alloy systems. From Figure 33 (a) saturation is observable after only a few hundred cascades in most systems, with only WTa20 and VCr70 continuing to build up FPs. It is also worth noting that these compositions have the minimum PEL heterogeneity in each set of three.

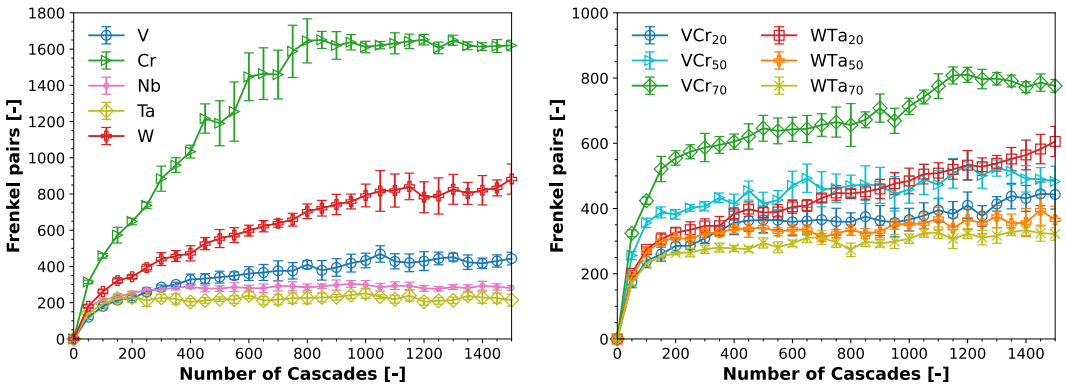

(a) *(b)*

Figure 33: Point defect (FP) evolution as a function of the number of subsequent cascades for the pure metals modeled (a) and 6 example of mixed systems (b).

Figure 34 (a) and (b) display respectively the number of FPs and the size of the biggest defect cluster for the binary systems after primary radiation damage saturation. It is notable that fewer FPs are observed in the V-rich region of the VCr system, corresponding to the maximum in MEB variance. Similarly, fewer defects are observed in the Ta-rich region of the WTa system, also corresponding to higher MEB variance.

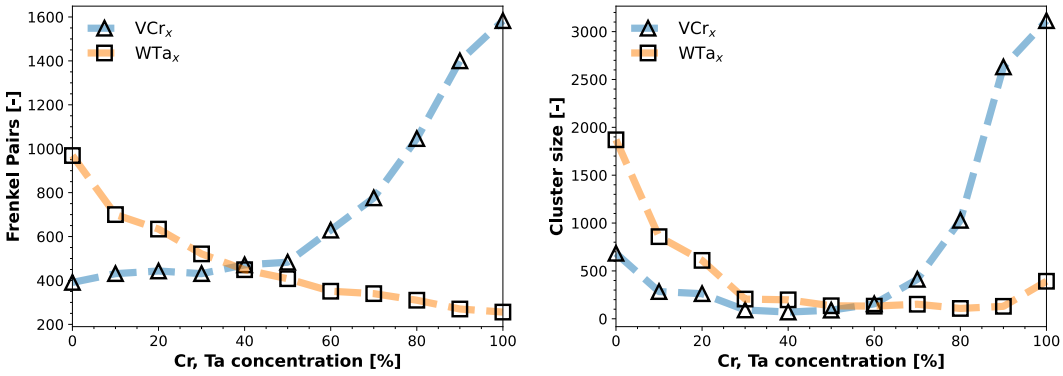

(a) *(b)*

Figure 34: Damage results at saturation for the VCr and WTa mixed systems as a function of the concentration. Frenkel pair defects (a) and size, in terms of number of point defects, of the biggest defect cluster recorded (b).

Data trends in Figure 30 and Figure 34 (a) as well as results on pure elements suggest a proportionality between number of FPs and MEB sample average values, and an inverse proportionality between FPs and the absolute value of the potential energy |U|. A figure of merit called MUR (MEB – U Ratio) is introduced to study the dependency. Eq. 17 defines the MUR:

$$MUR = \frac{MEB}{|U|} \qquad \text{Eq. 17}$$

Table 10 summarizes the results for pure metals including the MUR values. The table includes also results from Jin's work. In this respect, it is necessary to recall that pure FCC Fe was not fully characterized in that study, so MEB and FP have been interpolated [133].

Table 10: Summary of pure metal results. Model characteristics (box size, interatomic potential library), PEL main figures (U, MEB, MUR), damage figures (defects).

Element (crystal structure)	**atoms in box**	$U\left[\frac{eV}{atom}\right]$	**MEB [eV]**	**MUR** $\left[\frac{eV \cdot atom}{eV}\right]$	**FP @ 1500 cascades**	**FP/atom@ 1500 cascades** $[\cdot 10^{-3}]$	**Potential**	**Reference**
V (BCC)	128,000	-5.40	0.76	0.14	444 ± 35	3.47 ± 0.27	VTiCr EAM-FS	This work
Cr (BCC)		-4.05	1.59	0.39	1628 ± 35	12.72 ± 0.27		
Nb (BCC)		-7.09	0.65	0.09	279 ± 16	2.18 ± 0.13	Nb EAM	
Ta (BCC)		-8.08	0.80	0.10	221 ± 37	1.73 ± 0.29	WTa EAM-FS	
W (BCC)		-8.88	1.80	0.20	883 ± 83	6.90 ± 0.65		
Fe (FCC)	108,000	-4.40	0.75	0.17	≈ 500	≈ 4.63	FeNiCr EAM	Jin et al.
Ni (FCC)		-4.45	1.09	0.24	≈ 900	≈ 8.33		

Figure 35 makes explicit the results arranged by the MUR ratio – Frenkel Pairs phase space. There is a clear proportional correlation between the two figures. Pure metals in particular show a strong linear correlation.

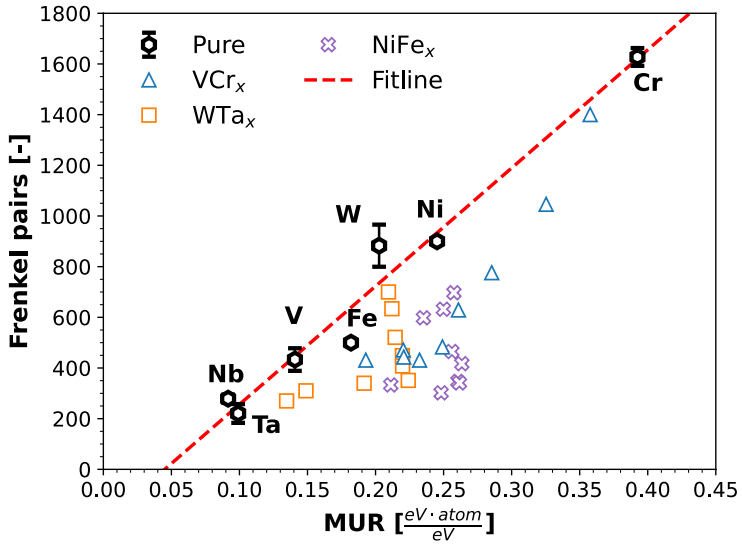

Figure 35: Point defects as a function of MUR (MEB-to-U ratio) for pure metals and mixed systems after primary radiation damage saturation. Ni, Fe, and Ni-Fex results extracted from Jin et al. [5]. Statistical results are applied for the pure metals that have been analyzed in this work. A fitting line for pure metals is included (red dashed line).

Eq. 18 makes explicit the fitting line found for pure metal data. The coefficient of determination R^2 is equal to 0.967. Eq. 19 is the same equation in a dpa-like magnitude. Namely, it is based on the same results normalized on the number of atoms in the simulation box. It is characterized by a $R_{PEL}^2 = 0.975$.

$$FP(7.5\,MeV) = 4637 \cdot MUR - 205 \qquad \text{Eq. 18}$$

$$dpa_{PEL}\,(7.5\,MeV) = 0.03714 \cdot MUR - 0.00149 \qquad \text{Eq. 19}$$

R^2 reaches lower values when including mixed system data, indicating bad predictions with respect the pure metal fitting lines proposed. The best fitting lines that consider results of all the pure and mixed systems studied are shown in Eq. 20 and Eq. 21:

$$FP(7.5\,MeV) = 18666 \cdot MUR^2 - 4973 \cdot MUR + 657 \qquad \text{Eq. 20}$$

$$dpa_{PEL}\,(7.5\,MeV) = 0.12785 \cdot MUR^2 - 0.0295 \cdot MUR + 0.00424 \qquad \text{Eq. 21}$$

Nonetheless, the corresponding R^2 and R_{PEL}^2 only reach values of 0.717 and 0.700, respectively, indicating less of a good fit when comparing MUR alone with number of FPs produced. Clearly additional variables must be elucidated to better explain the results.

The lines provide negative defect production results for very low MUR values. So, either additional elements could provide more precision in finding the actual fitting line or it is possible to that no element has MUR values lower than ~ 0.6 $\left[eV \cdot \frac{atom}{eV}\right]$. For sake of clarity in Figure 35 horizonal error bars belonging to mixed systems have not been added. Error bars can however be derived from Figure 30(c) and (d). It is worth mentioning that binary alloy systems stand in the lower-right side of the pure elements fitting line. They therefore show lower damage in correspondence of a higher MUR ratio driven, in this case, by a higher average MEB and higher heterogeneity by definition compared to single elements. This could be attributed to the effect of the system mixing energy and MEB heterogeneity. For this reason, Figure 36 is shown. It displays VCr and VTa systems in MUR – FP phase space with a focus on the element concentrations.

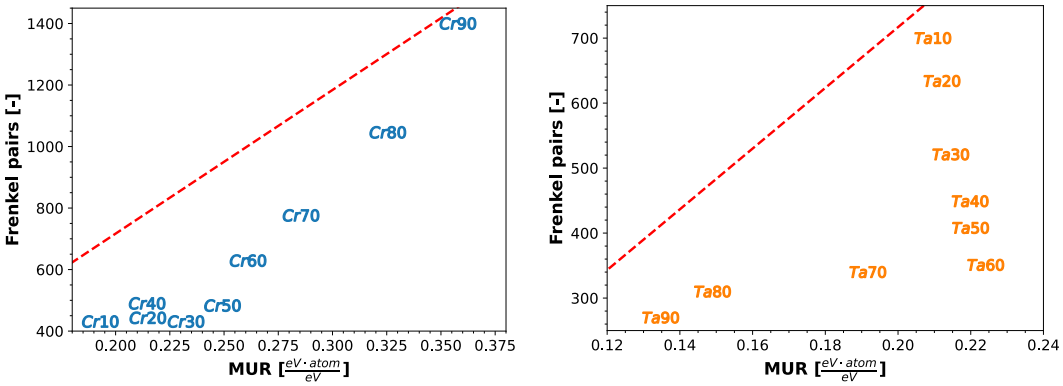

(a) *(b)*

Figure 36: FP Vs MUR for mixed systems. VCrx (a) and WTax (b). Concentrations are made explicit in the figure markers.

Figure **37** depicts the extent of damage as a function of MEB heterogeneity. More specifically, FPs have been plotted against MEB standard deviation, our quantitative measure of PEL heterogeneity, for the VCr and WTa systems. Jin et al showed that in NiFe primary damage is smaller in concentrations where the MEB heterogeneity is higher [133]. Figure 36 and Figure 30 (e) and (f) and, especially, Figure 16 confirm a similar trend also for VCr and WTa systems, in a manner more readily visualized farther away from the equiatomic (50/50) composition compared to the NiFe system. It is also worth acknowledging that while NiFe system characterized by Jin has high MEB values, high MEB heterogeneity and high radiation resistance at high |U| and at the mixing energy maximum (equimolar concentration), VCr and WTa are different situations, enriching the case for our core hypothesis.

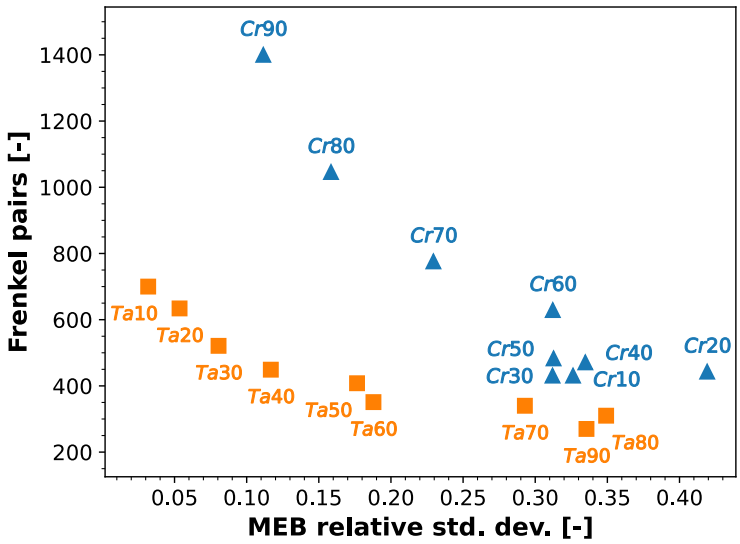

Figure 37: Frenkel Pairs Vs MEB relative standard deviation for VCrx and WTax systems. Concentrations are made explicit near the figure markers.

1.4 Discussion

Results from MD simulations strengthen the PEL heterogeneity – primary damage relation correlation. Both U and defect MEBs seem to play an important role in the primary radiation damage of metals. Considering pure metals, it seems that there is a strong linear correlation between the defects produced and the MUR. This makes sense for several reasons. It is true that systems with lower potential energies are more stable. Hence, it is reasonable to expect a more effective cascade recombination. Alongside the quasi-static parameter given by U, there are two dynamic properties that play a role in the cascade evolution and defect production. Ed is the first one and describes the initial phase of the cascade, in effect dividing normalizing cascade energy by this value to return number of defects. It would be logical that the higher the Ed, the smaller would be the cascade as the PKA and every surrounding atom would require and dissipate more energy in its knocking on phase.

DPA models so far apply E_d as main material parameter for the computation of the defects production and describe the dose. Additional works tried to explain also the ending phase of a cascade, namely recombination, and enhanced the analytical model with ad hoc coefficients [145], [149]. Such coefficients take into account the defect production efficiency (ξ), which depends on the recoil atom energy. Still, these studies did not manage to study the PEL in order to explain recombination rates, and they focused on few cascades, missing the defect saturation phenomenon.

Here we provide an explanation of the cascade recombination through the PEL. It is possible that in the very last phase of the cascade (the cascade tail),

atoms still have some energy to move a little, but they have largely reached their lattice-ordered configuration already. Lower and more uniform MEBs suggest a "smoother" PEL, increasing the likelihood for atoms with still little energy left to diffuse and find an energy well in a correct lattice position, ultimately reducing the number of defects left. Given the magnitude of the energies this could be considered "thermal" phase of the cascade recombination, in contraposition with its preceding phase, namely the "athermal" phase discussed by Nordlund [145]. The defect MEB is thus the second thermodynamic parameter that affects the defect production.

A linear correlation between the MUR and the defect production has been observed at primary damage saturation. Therefore, a formalism is proposed including MUR and damage saturation effects in order to increase the precision of the dpa figure of merit (Eq. 22).

$$dpa_{PEL} = \frac{0.8 \cdot E}{2 \cdot E_d} \cdot \xi \cdot f(MUR) \cdot c_s \qquad \text{Eq. 22}$$

where ξ is the defect production efficiency and cs is a correction coefficient for considering damage saturation. This work focused only on 5 keV of recoil energy, hence additional data should be provided to verify the dpa_{PEL} equation. Nonetheless, 5 keV has been chosen because it is expected to stand where damage efficiency ξ stabilizes for most metals (around the value of 0.2-0.3). It is therefore possible to suggest that the validity region of the proposed dpa_{PEL} formalism is at energies higher than the defect production efficiency stabilization and above the primary damage saturation dose. With the Ed values summarized by Nordlund [145], a defect production efficiency of 0.25 and a cs equal to 0.21, Eq. 22 and present results at 1500 cascades show a coefficient of determination R^2 equal to 0.83, with the highest error given by Ed of tungsten [145]. Without tungsten, R^2 would be above 0.95.

Comparing pure elements and mixed systems in Figure 35, it is found that mixed systems stand in the lower-right region of the MUR – FP phase space. Namely, mixed systems have lower damage and higher average MURs than the fitting line found for pure metals. Including mixed systems in the model required a change in the fitting lines that became quadratic. Still, the quality of the predictive model found was only R^2=0.7, suggesting that the model for just pure metals has much better prediction capabilities. This could be expected, as pure metals should display very low PEL heterogeneity due to their high symmetry, and thus the MUR/FP ratio may be the only variable at play. The FP and MUR values of mixed systems tend to stand between the corresponding values of their composing elements. This can be attributed to the heterogeneity of MEB values. In fact, Figure 36 and Figure 30 (e) and (f) confirm that single-phase, binary alloy systems that have higher MEB heterogeneities tend to show better irradiation resistance, as observed by Jin [133]. In addition, it seems that the FP and MUR of mixed systems stand between the same figures of the composing elements. Hence,

a mixed system has, in the worst-case scenario, the radiation resistance of its least resistant element. In other words, a mixed system stands somewhere between better than the best, and equal to the worst, of its constituent elements, in terms of radiation resistance. So, it is possible to qualitatively predict the damage resistance of highly mixed systems by characterizing the PEL of the single composing elements, namely by characterizing the MUR of composing elements and comparing them with the model here proposed in Eq. 18 and Eq. 19, and adding an effect of PEL heterogeneity of the mixture. The effect of the system mixing energy best is observed in the size of the biggest cluster. Mixed systems indeed experience smaller defect clusters where the composition is nearly, but not quite equimolar, in fact skewing together with the composition of maximum PEL heterogeneity. This is another important result as bigger vacancy clusters could result in bigger swelling bubbles when they interact with helium transmuted in the matrix.

It is thus possible to suggest some guidelines for the design of MPEAs resistant to primary damage. For the element selection lower MUR values should be preferred. Similarly, higher MEB heterogeneities should help encourage intracascade defect recombination, reducing the amount of residual radiation damage. Lastly, nearly equimolar compositions should generally enhance the size minimization of defect clusters, though this is not a strict guideline.

Lastly, it is necessary to discuss the level of uncertainty of the results and its limitations. It is clear that this work focuses only on primary radiation damage, given the space and time scale limits of MD. The system is assumed in ideal conditions (perfect mixing, no grain boundaries, and no elemental transmutation). This may be oversimplified for real conditions. Nonetheless, it isolates the dynamic effects of the collision cascade which would not be otherwise observable. This aspect makes this type of simulations a powerful tool for theoretical evaluations. Another cause of uncertainty is the dependence of results on the interatomic potential applied. It is usually necessary to accurately chose interatomic potentials accordingly to the phenomenon that has to be modeled. However, the number of available potentials is often too limited. In some instances, it somehow possible to correct potentials, like in the case of EAM-ZBL hybrid potentials for correctly describing the collision cascade. Still, in some cases potentials may not properly model a given phenomenon. It is the case of the MEB value for pure Cr which does not match experimental data. The potential was designed for ternary systems with high V and low Ti and Cr concentration [162]. Results on the other pure elements and on NiFe and WTa already provide enough consistent results for this work. While Cr might require additional analysis. To confirm and increase the precision of this studies results, future works should apply different potentials built ad hoc for the purpose. In addition, more pure elements should be included. Lastly, the work should be expanded to other binary and additional ternary, medium and high entropy alloy systems once suitable interatomic potentials are developed.

According to the results obtained, it is possible to assess the primary radiation resistance of the structural materials considered in this thesis. Figure 35 shows that Ta and V have the best thermodynamic PEL properties that minimize the primary radiation damage. This could be part of the reason why scientists found V-based alloys to have a relatively high radiation tolerance. There are surely several radiation damage mechanisms at higher time and length scales that could overshadow the primary damage effects. Nevertheless, regarding the elementary damaging mechanisms it is possible to assess the resistance of the main classical alloys here studied. As mentioned, V-based systems, such as V-Cr-Ti (especially with low Cr content, like V-4Cr-4Ti), are expected to have a high radiation resistance, followed by Fe-based alloys (e.g. Eurofer-97) and Ni-based alloys (e.g. Inconel-718). It is worth to recall also that Ni-based alloys have a FCC microstructure while V-based and most reactor relevant Fe-based alloys have a BCC microstructure, which favours radiation resistance. On the other hand, Ni-bases superalloys can be considered, to some extent, MPEAs as they often have 50-60% of Ni and 10-20% of Fe and Cr, depending on the alloy type. Inconel-718 in particular has about 20% of Cr, 20% of Fe and 5% of Nb. Despite the medium-high MUR of Ni-rich systems, it his highly probable that Inconel-718 has a high MEB heterogeneity, increasing the likelihood of a relatively good radiation resistance. Results of this chapter might be even more useful for the design of advanced materials (i.e. MPEAs). In particular, it is ideally possible to chose 2 or more elements with relatively low MUR and combine them with concentrations able to maximize the MEB heterogeneity. Assuming the systems found would be microstructurally stable, the alloy formed would have a high chance to be radiation resistant, at least for what concerns the primary radiation damage mechanisms. The HEA considered in this work, namely the WTaVCrTi, is expected to have a quite good radiation resistance. Given that V, Ta and W are present. Cr, as mentioned, could require additional studies, while Ti has not been assessed in this study. For WTaVCrTi, it would be worth to expand the study in order to find the compositions that minimize the MUR and, especially, maximize the MEB heterogeneity.

1.5 Conclusions

This chapter focused on pushing forward research about primary radiation damage mechanism on pure transition metals and mixed systems. The goal was to investigate the likely link between a system PEL and its primary radiation damage resistance in order to shed some light on the actual mechanisms behind this phenomenon as well as to contribute to enhance the precision of the dpa figure of merit. The wider goal was to use the link found to assess the theoretical radiation resistance of the ractor-relevant classic alloys studied in this thesis as well as provide guidelines and simplified figures of merit for designing advanced materials with high radiation tolerance. The study performed molecular dynamics modeling of primary damage in low activation transition metals and selected

single phase, binary alloy systems. Elements explored are V, Cr, Nb, Ta, and W, while binary alloy systems considered are VCrx and WTax. Results regarding Ni, Fe and NiFex systems were derived from previous works. The analysis targeted the possible links between PEL parameters of systems (U, MEBs, MEB variance) and primary radiation damage defect production (FPs at damage saturation). The main modeling choice was to reach both the damage efficiency plateau and defect production saturation (EPKA=5 keV, 1500 collision cascades). Regarding the modeling method, it has been found that both PEL characterization and primary damage results are particularly sensitive to the interatomic potential chosen. Consistency in their correlation is still likely. Focusing on the goals of the work, the study confirmed that a system PEL and its primary radiation damage tolerance are linked and shed some light on what the actual links are. There is a direct proportionality and a linear correlation between the MEB-U ratio (MUR) and primary radiation damage for the pure elements considered. For this reason, it is possible to expect that V-based alloys would have a higher radiation resistance than Fe-based and, especially, Ni-based alloys, if intended as classic alloys (very high concentration of the alloy main element). Regarding MPEA-relevant results, average MURs of mixed systems are between MURs of their composing elements or slightly higher. Defect production of mixed systems stand between the defect production of their composing elements or slightly lower. In addition, nearly equimolar concentrations of mixed systems (high mixing energy) seem to correspond to smaller defect clusters. Higher MEB heterogeneities seem to correspond to higher primary radiation resistance in single-phase, binary alloy systems. According to the results presented it should be possible to enhance the precision of defect production predictions in metals with irradiation dose. In second instance, it is possible to compare the primary damage resistance of materials through a PEL characterization. Lastly, it is possible to qualitatively predict the damage resistance of solid solutions starting from the PEL properties of the single composing elements. Hence, it is possible to speed up the design process of radiation resistant MPEAs by a targeted characterization of the composing elements as well as a careful composition choice.

Chapter 6

Conclusions

This work goals were to assess the main issues for structural materials in compact tokamaks and identify the most suitable existing materials for the purpose. An additional goal, more focused on pushing forward fundamental research, was to explore physical rules and improve figure of merits in order to ease and accelerate the existing material selection as well as to provide solid guidelines for the design of next generation materials (i.e. MPEAs, most likely). The framework for this work is the aim to move ARC reactor from a pre-conceptual design to a conceptual design. Thus, ARC is the main case study for this work.

Chapter 2 focused on an assessment on the main thermal and mechanical properties of the reactor relevant structural materials. In Chapter 3 the necessity to secure a self-sustainable fuel-cycle was addressed. For a correct reactor functionality, the effect of core structural materials on the tritium breeding ratio has been assessed. Structural integrity, thermal effectiveness and the effects on fuel productions are the fundamental functions that need to be satisfied by the vessel materials. In this work additional studies have been conducted on the material response to the reactor radiation environment. More specifically, the radiation induced activation has been assessed in Chapter 4, including the effectiveness of some techniques for the radioactivity minimization. In this framework, gas transmutation rate has been evaluated in order to start facing the likely problem of swelling in fusion reactor materials. Lastly, Chapter 5 proposed a study aimed to provide better understandings of the basic physical principles behind radiation damage and resistance of materials. Primary radiation damage stands behind several irradiation damage mechanisms, including the aforementioned swelling. Such study has clear implications on the reactor-

relevant materials considered and provides meaningful information for the design of radiation resistant advanced materials.

Overall results pointed clearly to V-Cr-Ti systems to be the most attractive in terms of thermal and irradiation properties. Effects on the fuel cycle and radioactive waste have been identified as the most positive, in addition to a likely enhanced radiation resistance. MPEAs and, especially, refractory solid solutions and HEAs have shown the potential to provide similar positive aspects alongside the promise of extremely high temperature resistance and structural integrity, if properly tuned. However, the state of the art and readiness level of V-Cr-Ti systems and especially MPEA technologies seem to not match the timeline of deployment of ARC pilot plant. It is likely that classic alloys will be chosen for the first versions of ARC while advanced materials will be left for the improved versions.

Because of the high mechanical strength and the high operating temperature required, Ni-based superalloys seem to be the best fitting choice for first ARC versions. Ni-based superalloys have already a relatively wide range of tuned options, depending on the composition and microstructure and most of them have already been characterized for specific functions. Depending on the most concerning issue (e.g. corrosion, structural strength, high thermal loads), it is possible to choose an already optimized and characterized Ni-based superalloy. In this respect, an appendix at the end of the work provides a preliminary assessment of Ni-based superalloys and identifies the most attractive ones. Nevertheless, it is clear that the Ni-based version of ARC structures cannot be other than a temporary stage as it would raise the reactor complexity and the radioactive waste concern. It is then suggested that a first ARC vessel version would rely on Ni-based superalloys structures. Meanwhile, research should focus on bridging the gap between laboratory- and commercial-scale V-Cr-Ti systems production, as well as developing effective and reliable machining and welding techniques for such materials. Effective corrosion barriers should be developed, and first ARC version should be involved in an actual assessment of the alloy resistance to fusion radiation environment. In this instance, a second version of ARC core structures should be able to rely on V-Cr-Ti systems. Similar steps should be taken for a MPEA-based third version of the reactor structures. Taking advantage of the knowledge obtained by the first two ARC core versions, which should provide the actual weight of each physical issue faced by materials in the reactor, a set of MPEAs perfectly tuned in order to face at best the mentioned issues should be developed. MPEAs with refractory W, Ta and semi-refractory V have the potential to both maximize the reactor thermodynamic efficiency and provide an enhanced resistance to radiation damaging mechanisms and swelling.

It is the study on radiation damage mechanisms that provided results with a range of practicality that goes also beyond the ARC case study. Main results strengthened the hypothesis of a link between a material potential energy

landscape and its response to radiation. In addition, the main figures that characterize the material potential energy landscape and influence radiation resistance have been identified. More specifically, the potential energy (U), the migration energy barrier (MEB) and its heterogeneity seem to be the driving parameters for a metal radiation response. For pure metals this work found a linear correlation between the U and MEB ratio (MUR) and defects buildup with radiation. This is particularly useful for classic alloys as they have a very high percentage of a single element. The correlation found confirms the expected high radiation resistance of V-rich systems (V-Cr-Ti systems), that researchers observed also experimentally. Ni-based alloys should experience higher radiation damage. However, given the quite heterogeneous concentrations of superalloys, they may benefit from the mixing effects on PEL and radiation response. More specifically, it has been found that highly mixed systems seem to generate smaller defect clusters with radiation, which helps inhibiting the swelling nucleation and growth process. In addition, the migration energy barrier heterogeneity of mixed systems seems to be the key for an enhanced primary radiation damage in MPEAs. These findings provide additional motivations for the development of V-Cr-Ti systems first and highly mixed MPEAs, possibly composed by refractory, low activation and low MUR elements, then.

Alongside the pathway suggested for ARC-relevant advanced materials development, future works should put some efforts in better exploring the potential energy landscape effects on primary radiation damage. A PEL and primary radiation damage characterization on a wider range of materials should be performed. A PKA kinetic energy sensitivity analysis should be done in order to develop a high-precision dpa_{PEL} formalism. In addition, an analysis of primary radiation damage, gas transmutation, grain boundaries and other increased-complexity modeling should be pursued. A broad exploration and characterization of the mentioned parameters would be fundamental not only for the here suggested third version of ARC core structures framework, but also for the development of a family of highly optimized materials able of push forward the limits of resistance in extreme environments.

Appendix

Ni-based superalloys for ARC

Inconel-718 is the baseline material for ARC tokamak vacuum vessel. Moreover, although this work identified vanadium-based alloys as much more suitable for the reactor core structures, Ni-based superalloys readiness level match the reactor design and construction timing. For these reasons, this appendix has been made in order to provide an insight on Ni-based superalloys and relative ARC-relevant information available in literature.

Introduction

ARC reactor core structural materials require outstanding properties in almost all the fields (structural, thermal, chemical and nuclear). More specifically, the requirements are:

- High operating temperature and creep limit
- High yield strength
- Relatively high ductility
- High thermal conductivity
- Low thermal expansion coefficient
- High corrosion resistance in fluoride salt environments
- High neutron transparency or neutron multiplication
- High radiation resistance
- Low gas (H, He) transmutation
- Gas atoms and defect sinking capabilities

Ni-based superalloys do not match all of the listed requirements. However, they are the materials with the highest technology readiness level that can work at

one of the major cut-off parameters: the operating temperatures. Therefore, they are the most likely materials to be adopted in first ARC versions. As the Ni-based superalloys comprehend a wide range of materials, it is possible to identify and assess the best fitting one for ARC environment.

Ni-based superalloys are systems of high performance materials based on Ni-Fe-Cr solid solutions that can be found in a wide range of compositions. Commercially, there are over 20 type of alloys divided in more than 4-5 major brands. Because of the high nickel content such alloys present an FCC microstructure. High structural resistance, high temperature of operations and high corrosion resistance are probably the most important features of superalloys. Because of such characteristics Ni-based superalloys are the most applied materials when it comes to build structural components for extreme environments. In fact, they are largely applied in the aerospace field and the energy sector. Ni-based superalloys are often applied also in the nuclear field. Being developed and applied since the beginning of the XX century, the technology readiness level of such alloys is then advanced already. A large pool of experimental data is available for each field of application. Several formation and machining techniques have been developed and optimized for such alloys. Techniques to further increase the structural performance, such as strengthening precipitates and second phases, have been widely studied and well understood already.

Both material performances and the advanced experience developed with this family of materials lead nuclear reactor designers to propose it as baseline structural material for the core of advanced reactors like Gen-IV fission and nuclear fusion reactors (like, in fact, the MIT-CFS ARC reactor). However, despite the wide experience achieved about this family of alloys, their application in advanced reactor cores still raises some level of uncertainty in several physical aspects. Alongside an extreme mechanical, thermal, nuclear-related loads, the core environment of such machines is also the cause of some effects for which information and data available are quite limited and particularly hard to produce. Effects of very fast neutrons (8-14 MeV), corrosion effects and prolonged irradiation-corrosion-high temperatures synergistic effects are among the most concerning aspects that might dramatically change the suitability of such materials in the core of an advanced reactor.

In this work different families of alloys (Fe-based, Ni-based, V-based and advanced alloys) have been already compared precisely for assessing their suitability as structural materials in the ARC reactor core. However, it is worth to focus a deeper literature analysis and overview on Ni-based superalloys. In fact, the canonical aspects of the reactor operating conditions (mainly thermal and chemical) and the timeline proposed by the Commonwealth Fusion Systems for the construction of the reactor match Ni-based superalloys better than other structural materials. Inconel-718 is indeed currently the baseline material for ARC vacuum vessel, even though it is necessary. In this case, the readiness level of the

technology and the experience gained by the application of such materials in extreme environments over the last century play a huge role on the choice.

This chapter proposes a literature overview of different commercial Ni-based alloys focus on their response to ARC-relevant and most concerning aspects of physics. More specifically the thermal, structural, radiation and corrosion aspects are evaluated on the basis of available information provided by literature.

Alloys and Compositions

The most applied and studied Ni-based superalloys brands and nomenclature are Inconel, Incoloy, Hastelloy and Nimonic with surely several other less known brands. Table 11 lists some of the most successful and best performing alloys of such brands and relative composition. Compositions have been taken from the same database (i.e. Matweb website [177]). Superalloys are characterized by a high number of different elements and a wide range of possible compositions. Despite the system usually being Ni-Fe-Cr plus additional elements. Some Hastelloys often reduce iron in favor of molybdenum and Nimonic ones behave similarly with cobalt instead. C, Mn, Mo, Al, Co, Cu, Ti and Si are present in almost all the alloys considered. It is possible to find refractory metals in significant concentrations (Mo, Nb and W). More specifically, Inconel and Incoloy adopted Mo and Nb while Hastelloys adopted Mo and W. Hastelloys are the only superalloys found that use tungsten.

Table 11: Main Ni-based superalloys and relative compositions (from the Matweb website [177]).

Alloy		Composition [%]												
		Ni	**Fe**	**Cr**	**C**	**Mn**	**Mo**	**Nb**	**Al**	**Co**	**Cu**	**Ti**	**Si**	**W**
Inconel	**600**	> 72	6-10	14-17	0.15	1	-	-	-	-	0.5	-	0.5	-
	625	> 58	5	20-23	0.1	0.5	8-10	3.15-4.15	0.4	1	-	0.4	0.5	-
	718	50-55	17	17-21	0.1	0.35	2.8-3.3	4.75-5.5	0.2-0.8	1	0.3	0.65-1.15	0.35	-
	X750	>70	5-9	14-17	0.08	1	-	0.7-1.2	0.4-1	1	0.5	2.25-2.75	0.5	-
Incoloy	**825**	38-46	>22	19.5-26.5	0.05	1	2.5-3.5	-	0.2	-	1.5-3	0.6-1.2	0.5	-
	945	45-55	5.7-28	19.5-23	0.005-0.04	1	3-4	2.5-4.5	0.01-0.7	-	1.5-3	0.5-2.5	0.5	-
Hastelloy	**B3**	>65	15	1.5	0.01	3	28.5	-	0.5	3	-	0.2	0.1	3
	C22	56	3	22	0.01	0.5	13	-	-	2.5	-	-	0.08	3
	N	>71	5	7	0.08	0.8	16	-	0.5	0.2	0.35	0.5	1	0.5
	S	67	3	14.5-17	0.02	0.3-1	14-16.5	-	0.1-0.5	2	0.35	-	0.2-0.75	1
	X	>47	18	22	0.1	1	9	-	-	1.5	-	-	1	0.6
Nimonic	**75**	72	5	18-21	0.08-0.15	1	-	-	-	0.5	-	0.2-0.6	1	-
	85A	69	3	18-21	0.1	1	-	-	1-1.8	2	0.2	1.8-2.7	1	-
	90	55	1.5	18-21	0.13	1	-	-	1-2	0.2	0.2	2-3	1	-

	901	40-45	33	11-14	0.1	0.5	5-6.5	-	0.35	1	0.5	2.8-3.1	0.4	-
	105	51	1	14-15.7	0.12	1	4.5-5.5	-	4.5-4.9	18-22	0.2	0.9-1.5	1	-
	115	54	1	14-16	0.12-0.2	1	3-5	-	4.5-5.5	13-15.5	0.2	3.5-4.5	1	-
	263	49	0.7	19-21	0.04-0.08	0.6	5.6-6.1	-	2.4-2.8	19-21	0.2	-	0.4	-
	PE16	42-45	31	15.5-17.5	0.04-0.08	0.2	2.8-3.8	-	1.1-1.3	2	0.5	1.1-1.3	0.5	-
	PK33	54	1	16-20	0.07	0.5	5-9	-	1.7-2.5	12-16	0.2	1.5-3	0.5	-

Operating temperature and thermo-mechanical properties

Probably the most appreciated aspect of Ni-based superalloys is the elevated operating temperature allowed in combination with the high structural resistance. R&D on such materials permitted energy systems like nuclear reactors and, especially, gas turbines to reach extreme pressures and temperatures and superior power plant thermodynamic efficiencies. Structural properties widely vary for different superalloys. The yield strength varies from 200 MPa up to 1'100 MPa. Moreover, superalloys become appreciably ductile starting from very low temperatures (-100°C for some alloys). The upper limit of operating temperature allowed by such alloys without an extreme strength degradation and before creep kicks in is between 550°C and 800°C (~ 800-1050 K). The creep limit is not a precise temperature and it may vary depending on several parameters (composition, microstructure, grain size, purity, thermal treatments etc.). However, it is of common use to indicate the creep limit of a metal alloy qualitatively around 2/3 of its melting point. Figure 38 shows, for each alloy, the yield strength and the qualitative creep limit computed as 2/3 of the solidus temperature. Yield strength shown is considered at room temperature. Still, it is necessary to acknowledge that it tends to slightly lower with increasing temperature. In all the figures, *Inl*, *Ily*, *Hay* and *Nic* are shorts for *Inconel*, *Incoloy*, *Hastelloy* and *Nimonic*, respectively.

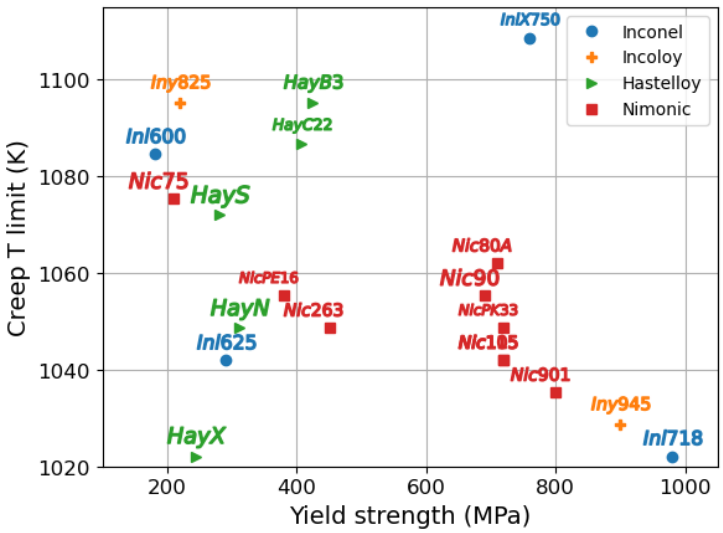

Figure 38: Creep limit [K] vs Yield strength [MPA] of the Ni-based superalloys considered in this work.

It should be possible to relax a little this limit with an ad-hoc alloy tuning (e.g. thermal treatment and increased grain size). While structural resistance is quite scattered, the upper bound of the operating limit is relatively similar for all the Ni-based systems considered (i.e. between 1000 K and 1100 K). According to ASME code Section III, the maximum primary stress allowed should be, for ductile materials, $\frac{2}{3}\sigma_y$ [178]. Here, the maximum primary stress allowed varies from about 120 MPa of Inconel-600 up to 650 MPa of Inconel-718. Considering nuclear reactors, in normal operating conditions thermal stress reach often concerning level. Once again, ASME Sec. III provides a limit on secondary stresses equals to 3 times the limit on the primary stresses, in this case about $2\sigma_y$ [178]. The secondary stress limit for such alloys range from about 350 MPa (Inconel-600) to almost 2'000 MPa (Inconel-718). The yield strength tends to degrade with temperature. Hence, for high temperatures such limits are expected to be a little lower. Inconel-718 at its creep limit (i.e. about 1020 K) is expected to have about 630 MPa and 1880 MPa as primary and secondary stress limits, respectively. According to Hooke's law for continuum mechanics, induced thermal stress is directly proportional to the material thermal expansion coefficient and inversely proportional to the thermal conductivity. In this instance, all the Ni-based superalloys here considered seem to behave similarly. Despite some minor difference of less than 5-10%, the thermal expansion coefficient of all the alloys is around 12-13e-6 K^{-1} with a similar evolution with temperature. Thermal conductivity is between 10 and 14 $\frac{W}{m^2 \cdot K}$ but at high temperature it raises between 21 and 23 $\frac{W}{m^2 \cdot K}$ for all the studied materials.

Corrosion

Ni-based superalloys are also extremely stable when it comes to withstand highly oxidizing environments. Nonetheless, ARC reactor entirely relies on FLiBe molten salt as coolant. Hence, this work focuses on the corrosion resistance of such alloys in fluoride-salt environments. Several studies identified the Cr content in the alloy as the main driver of corrosion resistance as it seems that the Cr depletion has, by far, the highest rate with respect all the other corrosion mechanisms [179], [180]. This is mainly due to the particularly low potential energy of formation of CrF_3 [32]. Some studies also suggested that the presence of Cr could trigger an accelerated Fe corrosion by the fluoride salt [39]. The corrosion of chromium, which is usually added to raise the oxidation resistance, is a twist for the choice of the alloy. It is the case of Hastelloy-X, which is often considered the reference superalloy for corrosion resistance [181]. Its high Cr content (about 22%) makes Hastelloy-X a quite endangered material in fluoride-salt environments. For this reason it is clear that materials with a low chromium content should be preferred so as to dramatically reduce the potential impact of fluoride-salt corrosion. Raising other elements with a low chemical affinity with fluorine (e.g. Mo and W) could hugely enhance the material corrosion resistance. Figure 39 focuses on the chromium content of the considered superalloys. Figure 39 (a) shows both Cr and Ni concentration for each alloy. Figure 39 (b) puts in the same graph the Cr content and the yield strength as it is one of the most relevant properties and it is variable in different alloys.

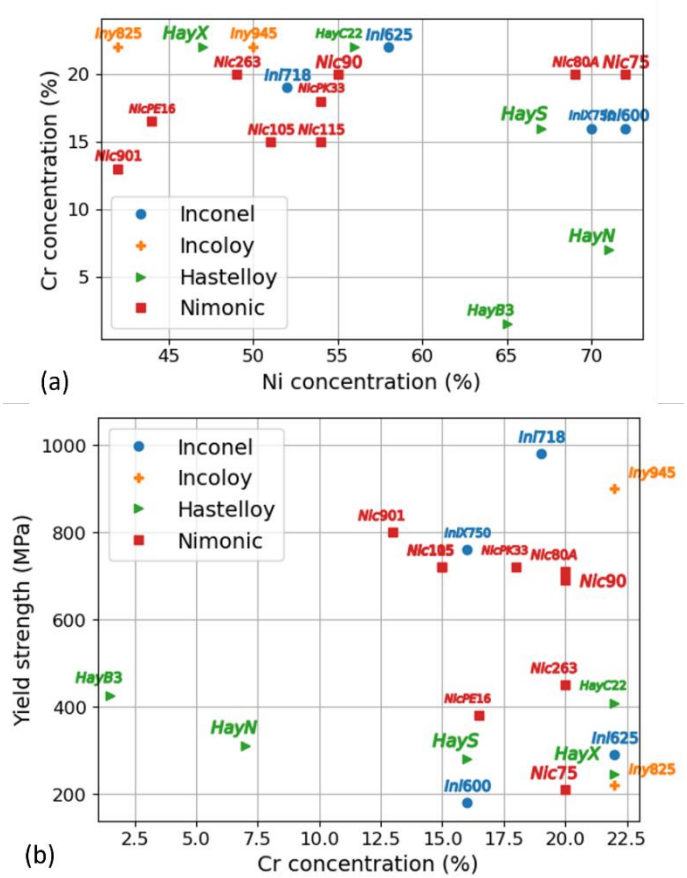

Figure 39: Cr-concentration vs Ni-concentration [%] (a) and Yield strength [MPa] vs Cr-concentration [%] (b) of the Ni-based superalloys considered in this work.

Only two Hastelloys present a chromium content lower than 10%. Hastelloy-B3, in particular, has only 1.5% of Cr and about 31.5% of Mo+W making it the superalloy with the highest chances to withstand FLiBe corrosion. However, the two low-Cr Hastelloys show a relatively low structural resistance (420 MPa and 310 MPa for Hastelloy-B3 and -N, respectively). Nimonic-901 seems to be an interesting middle ground between Hastelloy-B3 and Inconel-718. Its Cr content is between 11-14% and the yield strength is about 800 MPa. Still, it could be necessary to identify other superalloys with high strength but very low Cr concentrations. The alloy with the highest yield strength is Inconel-718 (i.e. almost 1'000 MPa) that, nonetheless, has a high Cr content (17-21%).

Lastly, the minimization of Cr content in favor of elements with higher chemical stability in fluoride environment could not be enough. Most works present in literature focused on static corrosion for a few hundred hours and found prohibitive corrosion rates [181], [182]. It is expected that the corrosion mechanism will be exacerbated by flowing FLiBe and irradiation [182].

Nuclear properties and effects

Nickel as an element is not particularly suitable for nuclear reactors. It is highly subjected to neutron induced activation and can cause the generation of high-level waste. Ni holds high neutron absorption cross section, and high gas transmutation rates in fast neutron regimes [110]. It is therefore of main concern for reactors neutron economy and its alloys are expected to be highly subjected to gas-enhanced swelling and embrittlement. In addition, Ni-based compounds tend to form FCC crystal microstructures which are further considered to be lower radiation resistant with respect the BBC crystals [183]. Nevertheless, because of the outstanding structural properties as well as the high temperature of operations allowed, Ni-based superalloys are particularly attractive for the application in advanced reactors. For these reasons nickel superalloys have been widely studied under irradiation. Experimental studies have been carried out both in ion irradiation regime and in fast neutron regimes.

Regarding the superalloy composition, Johnston et al. [184] Found that radiation resistance is higher, with a maximum at about 35-45% of nickel. In the same work some there where some clues that also chromium could play a role in the material radiation resistance. It seems that reducing chromium it should be possible to further reduce the radiation damage in the alloy. Hence, it seems that both for corrosion resistance and radiation resistance properties, a low content of chromium should be preferred. Other works focused on the effects of microstructure with on the material response to irradiation. Here there is the most interesting discovery regarding the swelling resistance of this family of alloys. It seems in fact that the typical strengthening precipitates Ni_3(Ti, Nb, Al) work as very effective defect and void sink. In particular, small and closely spaced Ni_3Nb precipitates have shown a superior capability as defects and void sinks [121]. Ni_3Nb precipitates are typical of the Inconel brand. Inconel superalloys often show a niobium concentration around 3-5%. Clearly, it should be possible to reproduce such type of precipitates also in other Ni-based superalloys by adding a 3-5% Nb.

It is worth to mention that some works showed some inconsistencies when compared to other works, especially swelling results on work that run experiments with ion irradiation and neutron irradiation. it is therefore clear that the radiation resistance and swelling resistance of Ni-based superalloys is hugely dependent on the actual characteristics of the irradiation environment. There is the possibility that a hard 14 MeV neutron irradiation environment will provide considerably different results with respect the ion, and fission neutron irradiation results present in literature. For instance, the Ni_3Nb precipitates may not be able to sink the defect production rate nor the higher gas transmutation or even get destroyed in high energy collisional cascades.

Discussion and Conclusions

Literature provides a considerable amount of information and data about Ni-based. It is clear that such materials have been widely characterized for canonical-but-still-extreme environments (i.e. high mechanical loads, high temperature, high thermal loads, creep, corrosion, fatigue etc.). However, there seems to be a little uncertainty about the behavior in more exotic environments (i.e. advanced reactor cores, fast neutron irradiation and highly corrosive flowing fluids). This work focused and summarized studies results relevant for advanced reactor and, especially for ARC reactor. In this framework, it is possible to note that the expected operating temperature matches the creep limit of this family of alloys. Despite that, because of the high thermal loads and the low thermal conductivity of the material, the alloy temperature is expected to reach values very close to the creep limit.

Having the considered alloys very similar thermal properties (maximum operating temperature, thermal conductivity and thermal expansion coefficient), it is the structural strength the most interesting property for a comparison in view of structural applications in thermal systems. In particular, In ARC primary stresses are expected to be relatively low in normal operations, while secondary stresses could reach values as high as several hundreds of MPa [185]. Hence, it is likely that the alloys with a yield strength around 200-300 MPa (e.g. Incone-600, Nimonic-75, Incoloy-825, Hastelloy-X and -S etc.) would not be suitable for the purpose. Also, although primary stresses are not expected to be extremely high in normal operations, some off normal operations (e.g. plasma major disruptions) require extreme structural resistance. Hence it could be necessary to select the alloy among the highest σ_y holders (e.g. Inconel-718). However, if it is possible to avoid excessively high mechanical loads, probably a material with a yield strength about 400 MPa could be sufficient. In this case even the low-Cr Hastelloy-B3 could be included as possible structural material for ARC.

Regarding corrosion, it is clear that the most effective strategy to adopt against fluoride salt corrosion would be the selection of a material with a low chromium content. Superalloys usually have around 15-25% of Cr. However, Hastelloy-B3 and -N show a relatively low Cr concentration in favor of molybdenum, which is much more chemically stable in fluorine-based environments. Such feature makes Hastelloy-B3 and -N good candidates for ARC vacuum vessel. Hastelloy-B3, in particular, has a very low Cr content (about 1.5%) and an almost acceptable yield strength (above 400 MPa), making it much more attractive than the -N series. Nevertheless, reducing the Cr content could not be enough in corrosion caused by flowing FLiBe in a radiation environment. Hence, it is likely that the development of some type of coatings would be necessary anyway.

Studies on radiation damage provided quite different results depending mainly on the experimental conditions, the type and energy of the incident particles.

However, it seems clear that the presence of small and closely spaced Ni_3Nb precipitates, typical of several Inconel compounds, are particularly effective in sinking defects and voids and hence raise the swelling resistance. Their effectiveness has not been tested with fusion neutrons induced defects nor in the case of high H and He transmutation rates. They are however a feature that should be pursued as best known defense against radiation embrittlement in Ni-based superalloys. In addition, there are clues about the effectiveness of a high Ni and low Cr content in raising the material radiation resistance. In this case the Hastelloy-B3 would be not only corrosion resistant but also slightly advantaged in radiation environments with respect other superalloys. It nonetheless does not have Nb in the matrix, which raises some concerns about swelling resistance.

It is possible to conclude that if the material structural resistance is the most concerning problem Inconel-718 should be the best choice (almost 1'000 MPa of yield strength). Such alloy features also the Ni_3Nb precipitates, which makes it a good choice against swelling. However, if future evidence highlight the possibility of corrosion taking over all the other physical issues in the reactor, Hastelloy-B3 should be considered for the core structures because of the low Cr content and high content of Mo. Also, Hastelloy-B3 seems to be able to operate at slightly higher temperatures. In the case the Cr content could be relaxed a little, but not enough for making Inconel-718 a viable choice, Nimonic-901 seems to be an attractive structural-chemical tradeoff. By logic, a Ni-based superalloy with a composition similar to the Hastelloy-B3 with about 3-5% of Nb should effectively tackle most of the critical issues regarding ARC reactor core environment (operating temperature, structural, chemical and irradiation damage). Table 12 summarizes some main relevant properties of the three most attractive alloys identified in this work. Namely, Inconel-718, Hastelloy-B3 and Nimonic-901. For each alloy the table lists the creep temperature limit, the thermal conductivity (k), the thermal expansion coefficient (α), the yield strength (σ_y), the Cr content as sign of corrosion susceptibility and Nb content as sing of the possibility of the Ni_3Nb precipitates for swelling resistance. Property values are colored from the best (green) to the worst (red). All properties are taken at room temperature even though they are expected to experience a slight variation with temperature.

Table 12: Main ARC-relevant properties of the three most attractive Ni-based superalloys. Property values are colored from best (green) to worse (red) [177].

Alloy	T limit [K]	k $\left[\frac{W}{m \cdot K}\right]$	α [K^{-1}]	σ_y [MPa]	Cr [%]	Nb [%]	Ni [%]
Inconel-718	~ 1'020	11.4	13.0e-6	980	17-21	4.75-5.5	50-55
Hastelloy-B3	~ 1'100	11.2	11.4e-6	425	1.5	-	> 65
Nimonic-901	~ 1'030	11.0	13.5e-6	800	11-14	-	40-45

Technologies for casting, forming and welding Ni-base superalloys are well known and optimized. In fact Ni-based superalloys (especially Inconel alloys) are used in nuclear reactors since the first generations of such machines. Research required would be therefore much less with respect other advanced alloys (ie.g. V-based systems). However, in the specific case of ARC reactor additional studies are strongly recommended. Experimental irradiation studies should be performed at dpa/He transmutation rates similar to the ones predicted in ARC. It is necessary to assess whether Ni_3Nb or other precipitates actually work as void sinks even at high damage and gas transmutation rates (probably a He ion accelerator or a combined fast neutron – He implantation could be useful in this respect). FliBe corrosion – neutron irradiation synergistic effects should be experimentally reproduced and studied. Especially in flowing FliBe regimes with additional fluorine and hydrogen isotopes in order to simulate the transmutation in FLiBe. The development of mitigating strategies (Be doping, W/Mo coatings etc.) may be needed. Lastly, experimental campaigns that aim to evaluate the actual effect of the material on the FLiBe tritium breeding ratio should be carried out. Simulations show that Ni-base superalloys bring the reactor tritium breeding ratio down to insufficient levels. Such aspect could compromise the power plant feasibility as well as the reactor economy.

References

[1] A. Moeslang *et al.*, “The IFMIF test facilities design,”*Fusion Eng. Des.*, 81, 8–14, 863, (2006).

[2] A. Ibarra *et al.*, “A stepped approach from IFMIF/EVEDA toward IFMIF,”*Fusion Sci. Technol.*, 66, 1, 252, (2014).

[3] P. G. Tipping, “24 - Outlook for nuclear power plant life management (PLiM) practices – summary, conclusions, recommendations,” in *Woodhead Publishing Series in Energy*, P. G. B. T.-U. and M. A. in N. P. P. Tipping, Ed. Woodhead Publishing, 2010, 876.

[4] A. B. Lindiard and M. Willieals, “Reliability problems of reactor pressure components,”*Inst. Adv. Financ. Account.*, 1, 233, (1978).

[5] F. J. Blom, “Reactor pressure vessel embrittlement of NPP borssele: Design lifetime and lifetime extension,”*Nucl. Eng. Des.*, 237, 20–21, 2098, (2007).

[6] K. L. Murty and I. Charit, “Structural materials for Gen-IV nuclear reactors: Challenges and opportunities,”*J. Nucl. Mater.*, 383, 1, 189, (2008),doi: https://doi.org/10.1016/j.jnucmat.2008.08.044.

[7] J. Vujić *et al.*, “Small modular reactors: simpler, safer, cheaper?,”*Energy*, 45, 1, 288, (2012).

[8] S. J. Zinkle, “Advanced materials for fusion technology,”*Fusion Eng. Des.*, 74, 1, 31, (2005),doi: https://doi.org/10.1016/j.fusengdes.2005.08.008.

[9] L. Malerba *et al.*, “Advances on GenIV structural and fuel materials and cross-cutting activities between fission and fusion,”*EPJ Nucl. Sci. Technol.*, 6, 32, (2020).

[10] M. J. Loughlin *et al.*, “Neutron activation studies on JET,”*Fusion Eng. Des.*, 58, 967, (2001).

[11] J. L. Luxon, “A design retrospective of the DIII-D tokamak,”*Nucl. Fusion*, 42, 5, 614, (2002).

[12] I. H. Hutchinson *et al.*, “The physics and engineering of Alcator C-MOD,”

(1988).

[13] S. Takeda and R. Pearson, “Nuclear fusion power plants,”*Power Plants Ind.*, 101, (2019).

[14] G. Federici *et al.*, “Overview of the DEMO staged design approach in Europe,”*Nucl. Fusion*, 59, 6, 66013, (2019).

[15] L. Giancarli *et al.*, “Test blanket modules in ITER: An overview on proposed designs and required DEMO-relevant materials,”*J. Nucl. Mater.*, 367, 1271, (2007).

[16] R. Pampin *et al.*, “Activation analyses updating the ITER radioactive waste assessment,”*Fusion Eng. Des.*, 87, 7–8, 1230, (2012).

[17] R. Lässer *et al.*, “Structural materials for DEMO: The EU development, strategy, testing and modelling,”*Fusion Eng. Des.*, 82, 5–14, 511, (2007).

[18] M. Gorley *et al.*, “Materials engineering and design for fusion—Towards DEMO design criteria,”*Fusion Eng. Des.*, 136, 298, (2018).

[19] L. Bromberg *et al.*, “Options for the use of high temperature superconductor in tokamak fusion reactor designs,”*Fusion Eng. Des.*, 54, 2, 167, (2001).

[20] B. N. Sorbom *et al.*, “ARC: A compact, high-field, fusion nuclear science facility and demonstration power plant with demountable magnets,”*Fusion Eng. Des.*, 100, 378, (2015),doi: https://doi.org/10.1016/j.fusengdes.2015.07.008.

[21] R. Mumgaard and S. Team, “SPARC and the high-field path,” in *APS Division of Plasma Physics Meeting Abstracts*, 2018, 2018, GO5.

[22] A. J. Creely *et al.*, “Overview of the SPARC tokamak,”*J. Plasma Phys.*, 86, 5, (2020).

[23] P. Rodriguez-Fernandez *et al.*, “Predictions of core plasma performance for the SPARC tokamak,”*J. Plasma Phys.*, 86, 5, (2020).

[24] R. Sweeney *et al.*, “MHD stability and disruptions in the SPARC tokamak,”*J. Plasma Phys.*, 86, 5, (2020).

[25] Y. Lin *et al.*, “Physics basis for the ICRF system of the SPARC tokamak,”*J. Plasma Phys.*, 86, 5, (2020).

[26] A. Q. Kuang *et al.*, “Divertor heat flux challenge and mitigation in SPARC,”*J. Plasma Phys.*, 86, 5, (2020).

[27] A. Q. Kuang *et al.*, “Conceptual design study for heat exhaust management in the ARC fusion pilot plant,”*Fusion Eng. Des.*, 137, 221, (2018),doi: https://doi.org/10.1016/j.fusengdes.2018.09.007.

[28] G. S. Was, *Fundamentals of radiation materials science: metals and alloys*.

springer, 2016.

[29] K. L. Murty and I. Charit, *An introduction to nuclear materials: fundamentals and applications*. John Wiley & Sons, 2013.

[30] E. S. Marmar and A. C.-M. Group, "The alcator c-mod program,"*Fusion Sci. Technol.*, 51, 3, 261, (2007).

[31] A. E. Costley, "On the fusion triple product and fusion power gain of tokamak pilot plants and reactors,"*Nucl. Fusion*, 56, 6, 66003, (2016).

[32] C. Forsberg *et al.*, "Fusion blankets and fluoride-salt-cooled high-temperature reactors with flibe salt coolant: common challenges, tritium control, and opportunities for synergistic development strategies between fission, fusion, and solar salt technologies,"*Nucl. Technol.*, 206, 11, 1778, (2020).

[33] M. C. Gazquez *et al.*, "Al2O3 coating as barrier against corrosion in Pb-17Li,"*Fusion Eng. Des.*, 124, 837, (2017).

[34] E. J. Frankberg *et al.*, "Highly ductile amorphous oxide at room temperature and high strain rate,"*Science (80-.).*, 366, 6467, 864, (2019).

[35] D. Iadicicco *et al.*, "Efficient hydrogen and deuterium permeation reduction in Al2O3 coatings with enhanced radiation tolerance and corrosion resistance,"*Nucl. Fusion*, 58, 12, 126007, (2018).

[36] R. L. Klueh, "Elevated temperature ferritic and martensitic steels and their application to future nuclear reactors,"*Int. Mater. Rev.*, 50, 5, 287, (2005).

[37] J. Zhang *et al.*, "Redox potential control in molten salt systems for corrosion mitigation,"*Corros. Sci.*, 144, 44, (2018).

[38] G. Zheng and K. Sridharan, "Corrosion of structural alloys in high-temperature molten fluoride salts for applications in molten salt reactors,"*Jom*, 70, 8, 1535, (2018).

[39] Y. Liu *et al.*, "Corrosion of Cr in molten salts with different fluoroacidity in the presence of CrF3,"*Corros. Sci.*, 169, 108636, (2020).

[40] C. Schroer *et al.*, "Selective leaching of nickel and chromium from Type 316 austenitic steel in oxygen-containing lead–bismuth eutectic (LBE),"*Corros. Sci.*, 84, 113, (2014).

[41] G. Parker, "Encyclopedia of materials: science and technology," (2001).

[42] R. L. Klueh *et al.*, "Ferritic/martensitic steels–overview of recent results,"*J. Nucl. Mater.*, 307, 455, (2002).

[43] A.-A. Tavassoli, "Present limits and improvements of structural materials for fusion reactors–a review,"*J. Nucl. Mater.*, 302, 2–3, 73, (2002).

[44] R. Konings and R. Stoller, *Comprehensive nuclear materials*. Elsevier,

2020.

[45] M. Rieth *et al.*, “EUROFER 97. Tensile, charpy, creep and structural tests,” Forschungszentrum Karlsruhe GmbH Technik und Umwelt (Germany). Inst. fuer …, (2003).

[46] T. K. Kim *et al.*, “Current status and future prospective of advanced radiation resistant oxide dispersion strengthened steel (ARROS) development for nuclear reactor system applications,”*Nucl. Eng. Technol.*, 48, 2, 572, (2016).

[47] P. Fernández *et al.*, “Creep strength of reduced activation ferritic/martensitic steel Eurofer’97,”*Fusion Eng. Des.*, 75, 1003, (2005).

[48] C. Y. Ho and T. K. Chu, “Electrical resistivity and thermal conductivity of nine selected AISI stainless steels,” Thermophysical and Electronic Properties Information Analysis Center …, (1977).

[49] S. J. Zinkle and N. M. Ghoniem, “Operating temperature windows for fusion reactor structural materials,”*Fusion Eng. Des.*, 51, 55, (2000).

[50] M. J. Assael and K. Gialou, “Measurement of the thermal conductivity of stainless steel AISI 304L up to 550 K,”*Int. J. Thermophys.*, 24, 4, 1145, (2003).

[51] K. Ioki *et al.*, “Design improvements and R&D achievements for vacuum vessel and in-vessel components towards ITER construction,”*Nucl. fusion*, 43, 4, 268, (2003).

[52] K. Horke *et al.*, “Metal injection molding (MIM) of nickel-base superalloys,” in *Handbook of Metal Injection Molding*, Elsevier, 2019, 575.

[53] A. A. Guimaraes and J. J. Jonas, “Recrystallization and aging effects associated with the high temperature deformation of Waspaloy and Inconel 718,”*Metall. Trans. A*, 12, 9, 1655, (1981).

[54] Z. Y. Wang *et al.*, “Hybrid machining of Inconel 718,”*Int. J. Mach. Tools Manuf.*, 43, 13, 1391, (2003).

[55] R. C. Reed *et al.*, “Alloys-by-design: application to nickel-based single crystal superalloys,”*Acta Mater.*, 57, 19, 5898, (2009).

[56] B. D. Conduit *et al.*, “Design of a nickel-base superalloy using a neural network,”*Mater. Des.*, 131, 358, (2017).

[57] S. Zhao *et al.*, “Microstructural stability and mechanical properties of a new nickel-based superalloy,”*Mater. Sci. Eng. A*, 355, 1–2, 96, (2003).

[58] Q. Lei *et al.*, “Inconel 617 corrosion in FLiNaK molten salts: An in situ X-ray diffraction study,”*Corros. Sci.*, 182, 109289, (2021).

[59] L. S. Richardson *et al.*, “CORROSION BY MOLTEN FLUORIDES.

Interim Report," Oak Ridge National Lab., Tenn., (1952).

[60] M. R. Gilbert *et al.*, "Automated inventory and material science scoping calculations under fission and fusion conditions,"*Nucl. Eng. Technol.*, 49, 6, 1346, (2017).

[61] A. Nowotnik, "Nickel-based superalloys," (2016).

[62] J. Blumm *et al.*, "Measurement of the thermophysical properties of an NPL thermal conductivity standard Inconel 600," in *Proc. of 17th European Conference on Thermophysical Properties*, 2003, 621.

[63] E. Kaschnitz *et al.*, "Electrical Resistivity Measured by Millisecond Pulse Heating in Comparison with Thermal Conductivity of the Superalloy Inconel 625 at Elevated Temperature,"*Int. J. Thermophys.*, 40, 3, 27, (2019),doi: 10.1007/s10765-019-2490-8.

[64] G. Pottlacher *et al.*, "Thermophysical properties of solid and liquidInconel 718 Alloy,"*Scand. J. Metall.*, 31, 3, 161, (2002).

[65] H. Kikuchi *et al.*, "Relationship between ferromagnetic properties and grain size of Inconel alloy 600,"*J. Magn. Magn. Mater.*, 381, 56, (2015).

[66] V. Shankar *et al.*, "Microstructure and mechanical properties of Inconel 625 superalloy,"*J. Nucl. Mater.*, 288, 2–3, 222, (2001).

[67] B. A. Loomis and D. L. Smith, "Vanadium alloys for structural applications in fusion systems: a review of vanadium alloy mechanical and physical properties,"*J. Nucl. Mater.*, 191, 84, (1992).

[68] D. L. Smith *et al.*, "Reference vanadium alloy V□ 4Cr□ 4Ti for fusion application,"*J. Nucl. Mater.*, 233, 356, (1996).

[69] D. L. Smith *et al.*, "Development of vanadium-base alloys for fusion first-wall—blanket applications,"*Fusion Eng. Des.*, 29, 399, (1995).

[70] H. M. Chung *et al.*, "Development and testing of vanadium alloys for fusion applications,"*J. Nucl. Mater.*, 239, 139, (1996).

[71] R. J. Kurtz *et al.*, "Critical issues and current status of vanadium alloys for fusion energy applications,"*J. Nucl. Mater.*, 283, 70, (2000).

[72] J. Chen *et al.*, "The influence of hydrogen on tensile properties of V-base alloys developed in China,"*J. Nucl. Mater.*, 307, 566, (2002).

[73] R. J. Kurtz and M. L. Hamilton, "Biaxial thermal creep of V–4Cr–4Ti at 700 C and 800 C,"*J. Nucl. Mater.*, 283, 628, (2000).

[74] P. F. Zheng *et al.*, "Creep properties of V–4Cr–4Ti strengthened by cold working and aging,"*Fusion Eng. Des.*, 86, 9–11, 2561, (2011).

[75] K. Natesan *et al.*, "Uniaxial creep behavior of V–4Cr–4Ti alloy,"*J. Nucl. Mater.*, 307, 585, (2002).

[76] S. Chomette *et al.*, “Creep behaviour of as received, aged and cold worked INCONEL 617 at 850° C and 950° C,”*J. Nucl. Mater.*, 399, 2–3, 266, (2010).

[77] J. P. Shingledecker *et al.*, “Influences of composition and grain size on creep–rupture behavior of Inconel® alloy 740,”*Mater. Sci. Eng. A*, 578, 277, (2013).

[78] T. Muroga *et al.*, “Present status of vanadium alloys for fusion applications,”*J. Nucl. Mater.*, 455, 1–3, 263, (2014).

[79] H. Nishimura *et al.*, “Chemical behavior of Li2BeF4 molten salt as a liquid tritium breeder,”*Fusion Eng. Des.*, 58, 667, (2001).

[80] J. T. Lenkkeri, “The elastic moduli of some body-centred cubic titanium-vanadium, vanadium-chromium and chromium-iron alloys,”*J. Phys. F Met. Phys.*, 10, 4, 611, (1980).

[81] O. N. Senkov *et al.*, “Mechanical properties of Nb25Mo25Ta25W25 and V20Nb20Mo20Ta20W20 refractory high entropy alloys,”*Intermetallics*, 19, 5, 698, (2011).

[82] J. Chen *et al.*, “A review on fundamental of high entropy alloys with promising high–temperature properties,”*J. Alloys Compd.*, 760, 15, (2018).

[83] D. B. Miracle and O. N. Senkov, “A critical review of high entropy alloys and related concepts,”*Acta Mater.*, 122, 448, (2017).

[84] Z. Wu *et al.*, “Phase stability, physical properties and strengthening mechanisms of concentrated solid solution alloys,”*Curr. Opin. Solid State Mater. Sci.*, 21, 5, 267, (2017).

[85] O. A. Waseem *et al.*, “The effect of Ti on the sintering and mechanical properties of refractory high-entropy alloy TixWTaVCr fabricated via spark plasma sintering for fusion plasma-facing materials,”*Mater. Chem. Phys.*, 210, 87, (2018).

[86] O. A. Waseem and H. J. Ryu, “Powder metallurgy processing of a WxTaTiVCr high-entropy alloy and its derivative alloys for fusion material applications,”*Sci. Rep.*, 7, 1, 1, (2017).

[87] O. A. Waseem *et al.*, “Reduced Activation W Alloys for Plasma Facing Materials,” in *Transactions of the Korean Nuclear Society Autumn Meeting*, 2016, 12.

[88] D. L. Smith *et al.*, “Vanadium-base alloys for fusion reactor applications—a review,”*J. Nucl. Mater.*, 135, 2–3, 125, (1985).

[89] K. Zhang and J. Aktaa, “Ratcheting behavior of Eurofer97 at 550° C,”*Nucl. Mater. Energy*, 15, 97, (2018).

[90] E. J. F. Dickinson *et al.*, “COMSOL Multiphysics®: Finite element

software for electrochemical analysis. A mini-review,"*Electrochem. commun.*, 40, 71, (2014).

[91] C. C. Bast and L. Boyce, "Probabilistic material strength degradation model for Inconel 718 components subjected to high temperature, high-cycle and low-cycle mechanical fatigue, creep and thermal fatigue effects," NASA. Lewis Research Center, (1995).

[92] R. J. Farraro and R. B. McLellan, "High temperature elastic properties of polycrystalline niobium, tantalum, and vanadium,"*Metall. Trans. A*, 10, 11, 1699, (1979).

[93] J. W. Davis and P. D. Smith, "ITER material properties handbook,"*J. Nucl. Mater.*, 233, 1593, (1996).

[94] T. Weber and J. Aktaa, "Numerical assessment of functionally graded tungsten/steel joints for divertor applications,"*Fusion Eng. Des.*, 86, 2–3, 220, (2011).

[95] K. Mergia and N. Boukos, "Structural, thermal, electrical and magnetic properties of Eurofer 97 steel,"*J. Nucl. Mater.*, 373, 1–3, 1, (2008).

[96] E. Lucon and W. Vandermeulen, "Overview and Critical Assessment of the Tensile Properties of unirradiated and irradiated EUROFER97," Belgian Nuclear Research Center SCK-CEN (Belgium), (2007).

[97] C. Heintze *et al.*, "Microstructure of oxide dispersion strengthened Eurofer and iron–chromium alloys investigated by means of small-angle neutron scattering and transmission electron microscopy,"*J. Nucl. Mater.*, 416, 1–2, 35, (2011).

[98] B. A. Kalin *et al.*, "Development of brazing foils to join monocrystalline tungsten alloys with ODS-EUROFER steel,"*J. Nucl. Mater.*, 367, 1218, (2007).

[99] G. Pintsuk *et al.*, "High heat flux testing of 12–14Cr ODS ferritic steels,"*J. Nucl. Mater.*, 396, 1, 20, (2010).

[100] R. Schaeublin *et al.*, "Microstructure and mechanical properties of two ODS ferritic/martensitic steels,"*J. Nucl. Mater.*, 307, 778, (2002).

[101] P. J. Karditsas and M.-J. Baptiste, "Thermal and structural properties of fusion related materials," UKAEA Government Division, (1995).

[102] B. A. Loomis *et al.*, "Tensile Properties of Vanadium and Vanadium-Base Alloys,"*Fusion Mater. Semi-Annual Prog. Reports*, 10, 145, (1991).

[103] R. Lindau *et al.*, "Present development status of EUROFER and ODS-EUROFER for application in blanket concepts,"*Fusion Eng. Des.*, 75, 989, (2005).

[104] S. J. Zinkle and J. T. Busby, "Structural materials for fission & fusion

energy,”*Mater. today*, 12, 11, 12, (2009).

[105] T. Jayakumar *et al.*, “High temperature materials for nuclear fast fission and fusion reactors and advanced fossil power plants,”*Procedia Eng.*, 55, 259, (2013).

[106] L. C. Curtil *et al.*, “Innovative materials for fusion reactors,”*ESSAYS Nucl. Technol. Vol. 1 2018*, 140, (2018).

[107] A. Khalili, “Effective Boronizing Process for Age Hardened Inconel 718,” (2017).

[108] H. M. Chung *et al.*, “Creep properties of vanadium-base alloys,”*J. Nucl. Mater.*, 212, 772, (1994).

[109] B. Bocci *et al.*, “ARC reactor materials: Activation analysis and optimization,”*Fusion Eng. Des.*, 154, (2020),doi: 10.1016/j.fusengdes.2020.111539.

[110] D. A. Brown *et al.*, “ENDF/B-VIII.0: The 8th Major Release of the Nuclear Reaction Data Library with CIELO-project Cross Sections, New Standards and Thermal Scattering Data,”*Nucl. Data Sheets*, 148, 1, (2018),doi: https://doi.org/10.1016/j.nds.2018.02.001.

[111] M. R. Gilbert *et al.*, “An integrated model for materials in a fusion power plant: transmutation, gas production, and helium embrittlement under neutron irradiation,”*Nucl. Fusion*, 52, 8, 83019, (2012).

[112] P. K. Romano *et al.*, “OpenMC: A state-of-the-art Monte Carlo code for research and development,”*Ann. Nucl. Energy*, 82, 90, (2015).

[113] A. R. Siegel *et al.*, “Multi-core performance studies of a Monte Carlo neutron transport code,”*Int. J. High Perform. Comput. Appl.*, 28, 1, 87, (2014).

[114] C. J. Werner *et al.*, “MCNP version 6.2 release notes,” Los Alamos National Lab.(LANL), Los Alamos, NM (United States), (2018).

[115] S. Segantin *et al.*, “Optimization of tritium breeding ratio in ARC reactor,”*Fusion Eng. Des.*, 154, (2020),doi: 10.1016/j.fusengdes.2020.111531.

[116] S. Segantin *et al.*, “Neutronic comparison of liquid breeders for ARC-like reactor blankets,”*Fusion Eng. Des.*, 160, 112013, (2020).

[117] M. Abdou *et al.*, “Physics and technology considerations for the deuterium–tritium fuel cycle and conditions for tritium fuel self sufficiency,”*Nucl. fusion*, 61, 1, 13001, (2020).

[118] G. Ferrero *et al.*, “A preliminary CFD and tritium transport analysis for ARC blanket,”*Fusion Sci. Technol.*, (Submitted, (2022).

[119] D. X. Fischer *et al.*, "The effect of fast neutron irradiation on the superconducting properties of REBCO coated conductors with and without artificial pinning centers,"*Supercond. Sci. Technol.*, 31, 4, 44006, (2018).

[120] D. S. Gelles, "Swelling in several commercial alloys irradiated to very high neutron fluence,"*J. Nucl. Mater.*, 122, 1–3, 207, (1984).

[121] W. K. Appleby *et al.*, "Swelling resistance of a high nickel alloy,"*J. Nucl. Mater.*, 43, 3, 213, (1972).

[122] M. Zucchetti *et al.*, "ARC reactor: Radioactivity safety assessment and preliminary environmental impact study,"*Fusion Eng. Des.*, 162, 112132, (2021).

[123] M. Fleming *et al.*, "The FISPACT-II user manual,"*Rep. UKAEA*, (2018).

[124] S. Villani, "Uranium enrichment," (1979).

[125] L. Chkhartishvili *et al.*, "10B-based materials for neutronshielding," in *Proceedings of the 1st international conference on "Modern technologies & methods of inorganic materials science". Meridian, Tbilisi*, 2012, 188.

[126] S. A. Levin *et al.*, "The separation of Tungsten-184," Oak Ridge Gaseous Diffusion Plant, Tenn., (1961).

[127] S. Segantin *et al.*, "ARC reactor–Neutron irradiation analysis,"*Fusion Eng. Des.*, 159, 111792, (2020).

[128] S. Fukuzumi *et al.*, "Defect structural evolution in high purity tungsten irradiated with electrons using high voltage electron microscope,"*J. Nucl. Mater.*, 343, 1–3, 308, (2005).

[129] V. K. Panday *et al.*, "Determination of trace impurities in tantalum by inductively coupled plasma mass spectrometry after removal of the matrix by liquid-liquid extraction,"*Anal. Chim. Acta*, 329, 1–2, 153, (1996).

[130] L. Di Pace *et al.*, *Radioactive waste management of fusion power plants*. INTECH Open Access Publisher, 2012.

[131] C. of the E. Communities *et al.*, *Report on the improvement of the management of radiation protection aspects in the recycling of metal scrap*. New York: United Nations, 2002.

[132] Y. Zhang *et al.*, "Influence of chemical disorder on energy dissipation and defect evolution in concentrated solid solution alloys,"*Nat. Commun.*, 6, 1, 1, (2015).

[133] M. Jin *et al.*, "Thermodynamic mixing energy and heterogeneous diffusion uncover the mechanisms of radiation damage reduction in single-phase Ni-Fe alloys,"*Acta Mater.*, 147, 16, (2018),doi: 10.1016/J.ACTAMAT.2017.12.064.

[134] D. R. Olander, “Fundamental aspects of nuclear reactor fuel elements,”*TID-26711-Pl (Atomic Energy Comm. 1976) p*, 301, (1985).

[135] V. Barabash *et al.*, “Neutron irradiation effects on plasma facing materials,”*J. Nucl. Mater.*, 283, 138, (2000).

[136] M. A. Stopher, “The effects of neutron radiation on nickel-based alloys,”*Mater. Sci. Technol.*, 33, 5, 518, (2017).

[137] M. Griffiths and R. Boothby, “Radiation Effects in Nickel-Based Alloys,” (2020).

[138] M. Klimenkov *et al.*, “Post-irradiation microstructural examination of EUROFER-ODS steel irradiated at 300° C and 400° C,”*J. Nucl. Mater.*, 557, 153259, (2021).

[139] E. Malitckii and M. Ganchenkova, “Hydrogen Uptake and its Effect on Mechanical Properties of EUROFER 97-2 and ODS-EUROFER Steels,” (2013).

[140] J. M. Chen *et al.*, “Overview of the vanadium alloy researches for fusion reactors,”*J. Nucl. Mater.*, 417, 1–3, 289, (2011).

[141] O. El-Atwani *et al.*, “Outstanding radiation resistance of tungsten-based high-entropy alloys,”*Sci. Adv.*, 5, 3, eaav2002, (2019).

[142] E. J. Pickering *et al.*, “High-entropy alloys for advanced nuclear applications,”*Entropy*, 23, 1, 98, (2021).

[143] S. Xia *et al.*, “Irradiation behavior in high entropy alloys,”*J. Iron Steel Res. Int.*, 22, 10, 879, (2015).

[144] K. Nordlund *et al.*, “Primary Radiation Damage in Materials. Review of Current Understanding and Proposed New Standard Displacement Damage Model to Incorporate in Cascade Defect Production Efficiency and Mixing Effects,” (2015).

[145] K. Nordlund *et al.*, “Primary radiation damage: A review of current understanding and models,”*J. Nucl. Mater.*, 512, 450, (2018),doi: 10.1016/J.JNUCMAT.2018.10.027.

[146] J. Knaster *et al.*, “Materials research for fusion,”*Nat. Phys.*, 12, 5, 424, (2016).

[147] G. H. Kinchin and R. S. Pease, “The displacement of atoms in solids by radiation,”*Reports Prog. Phys.*, 18, 1, 1, (1955).

[148] M. J. Norgett *et al.*, “A proposed method of calculating displacement dose rates,”*Nucl. Eng. Des.*, 33, 1, 50, (1975),doi: 10.1016/0029-5493(75)90035-7.

[149] S. Chen *et al.*, “Improved model for atomic displacement calculation,” in

EPJ Web of Conferences, 2020, 239, 8003.

[150] S. C. Edington *et al.*, "Infrared spectroscopy probes ion binding geometries," in *Methods in Enzymology*, 651, Elsevier, 2021, 157.

[151] W. Cai *et al.*, "1.09-Molecular Dynamics,"*Compr. Nucl. Mater.*, 249, (2012).

[152] A. Cocchi, *Elementi di termofisica generale ed applicata*. Società Editrice Esculapio, 2020.

[153] J. R. Ray and A. Rahman, "Statistical ensembles and molecular dynamics studies of anisotropic solids,"*J. Chem. Phys.*, 80, 9, 4423, (1984).

[154] S. Nosé, "A molecular dynamics method for simulations in the canonical ensemble,"*Mol. Phys.*, 52, 2, 255, (1984).

[155] W. G. Hoover, "Canonical dynamics: Equilibrium phase-space distributions,"*Phys. Rev. A*, 31, 3, 1695, (1985).

[156] M. M. P. Simulator, "LAMMPS Users Manual," (2003).

[157] O. Hardouin Duparc, "On the origins of the Finnis–Sinclair potentials,"*Philos. Mag.*, 89, 34–36, 3117, (2009).

[158] J. F. Ziegler and J. P. Biersack, "The stopping and range of ions in matter," in *Treatise on heavy-ion science*, Springer, 1985, 93.

[159] A. P. Thompson *et al.*, "LAMMPS - a flexible simulation tool for particle-based materials modeling at the atomic, meso, and continuum scales,"*Comput. Phys. Commun.*, 271, 108171, (2022),doi: 10.1016/J.CPC.2021.108171.

[160] G. Bonny *et al.*, "Interatomic potential for studying ageing under irradiation in stainless steels: the FeNiCr model alloy,"*Model. Simul. Mater. Sci. Eng.*, 21, 8, 85004, (2013).

[161] Y. Chen *et al.*, "Development of the interatomic potentials for W-Ta system,"*Comput. Mater. Sci.*, 163, 91, (2019),doi: 10.1016/J.COMMATSCI.2019.03.021.

[162] J. Fu *et al.*, "Improved Finnis-Sinclair potential for vanadium-rich V–Ti–Cr ternary alloys,"*J. Alloys Compd.*, 705, 369, (2017),doi: 10.1016/J.JALLCOM.2017.02.103.

[163] M. R. Fellinger *et al.*, "Force-matched embedded-atom method potential for niobium,"*Phys. Rev. B*, 81, 14, 144119, (2010).

[164] A. Stukowski, "Visualization and analysis of atomistic simulation data with OVITO–the Open Visualization Tool,"*Model. Simul. Mater. Sci. Eng.*, 18, 1, 15012, (2009).

[165] M. Parrinello and A. Rahman, "Polymorphic transitions in single crystals:

A new molecular dynamics method,"*J. Appl. Phys.*, 52, 12, 7182, (1981).

[166] B. Sadigh *et al.*, "Scalable parallel Monte Carlo algorithm for atomistic simulations of precipitation in alloys,"*Phys. Rev. B*, 85, 18, 184203, (2012).

[167] H. B. Lee *et al.*, "Atomistic simulations of surface segregation of defects in solid oxide electrolytes,"*Acta Mater.*, 58, 6, 2197, (2010),doi: 10.1016/J.ACTAMAT.2009.12.005.

[168] M. R. Hestenes and E. Stiefel, *Methods of conjugate gradients for solving linear systems*, 49, 1. NBS Washington, DC, 1952.

[169] G. Henkelman *et al.*, "A climbing image nudged elastic band method for finding saddle points and minimum energy paths,"*J. Chem. Phys.*, 113, 22, 9901, (2000).

[170] L. K. Béland *et al.*, "Features of primary damage by high energy displacement cascades in concentrated Ni-based alloys,"*J. Appl. Phys.*, 119, 8, 85901, (2016).

[171] A. F. R. F. Rochim, "Chauvenet's Criterion, Peirce's Criterion, and Thompson's Criterion (Literatures Review)."

[172] E. Wigner and F. Seitz, "On the constitution of metallic sodium,"*Phys. Rev.*, 43, 10, 804, (1933).

[173] E. P. Wigner and F. Seitz, "On the constitution of metallic sodium. II," in *Part I: Physical Chemistry. Part II: Solid State Physics*, Springer, 1997, 372.

[174] E. Alonso *et al.*, "Simulation of damage production and accumulation in vanadium,"*J. Nucl. Mater.*, 276, 1–3, 221, (2000).

[175] S. Wen *et al.*, "Transmutation elements Re/Ta effect on vacancy formation and dissociation behavior in W,"*arXiv Prepr. arXiv1906.06609*, (2019).

[176] C. A. Howells and Y. Mishin, "Angular-dependent interatomic potential for the binary Ni–Cr system,"*Model. Simul. Mater. Sci. Eng.*, 26, 8, 85008, (2018).

[177] "Matweb Material Property Data." https://www.matweb.com/ (accessed May 16, 2022).

[178] G. C. Slagis, "ASME section III design-by-analysis criteria concepts and stress limits," (2006).

[179] N. S. Patel *et al.*, "High-temperature corrosion behavior of superalloys in molten salts–a review,"*Crit. Rev. Solid State Mater. Sci.*, 42, 1, 83, (2017).

[180] K. J. Chan and P. M. Singh, "Corrosion Behavior of Pre-Carburized Hastelloy N, Haynes 244, Haynes 230, and Incoloy 800H in Molten FLiNaK,"*Nucl. Technol.*, 206, 11, 1751, (2020).

[181] M. K. Hariharan *et al.*, “Hot corrosion behaviour of Hastelloy X and Inconel 625 in an aggressive environment for superalloys for high-temperature energy applications,”*Appl. Nanosci.*, 1, (2022).

[182] H. Zhu *et al.*, “High-temperature corrosion of helium ion-irradiated Ni-based alloy in fluoride molten salt,”*Corros. Sci.*, 91, 1, (2015).

[183] Z. Chen *et al.*, “A comparative study on the in situ helium irradiation behavior of tungsten: Coarse grain vs. nanocrystalline grain,”*Acta Mater.*, 147, 100, (2018).

[184] W. G. Johnston *et al.*, “An experimental survey of swelling in commercial Fe-Cr-Ni alloys bombarded with 5 MeV Ni Ions,”*J. Nucl. Mater.*, 54, 1, 24, (1974).

[185] S. Segantin *et al.*, “The lifetime determination of ARC reactor as a load-following plant in the energy framework,”*Energy Policy*, 126, (2019),doi: 10.1016/j.enpol.2018.11.010.